Università degli Studi di Pavia

Dipartimento di Fisica

Corso di Laurea Magistrale in Fisica

Experimental and computational neutron beam characterization at the CN facility of the INFN National Laboratory of Legnaro

Tesi di la Laurea Magistrale di:
Matilde Avesani

Relatore:
Prof.ssa Silva Bortolussi
Correlatori:
Dott. Ian Postuma
Dott.ssa Anna Selva

A.A. 2021-2022

Abstract

Il lavoro descritto in questa tesi è stato sviluppato nell'ambito delle facilities per BNCT basate su acceleratori di particelle (AB-BNCT) e nel contesto del progetto ENTER-BNCT, finanziato dalla Commissione 5 per la ricerca tecnologica e inter-disciplinare dell'INFN. La BNCT è un tipo di adroterapia binaria che combina l'azione di un fascio di neutroni a bassa energia, termico o epitermico a seconda della profondità del tumore da trattare, ed un agente borato che è in grado di accumularsi selettivamente nel tumore. La reazione di cattura neutronica con il boro produce due particelle ad alto LET (Linear Energy Transfer), una particella alfa ed uno ione di litio, che depositano dose terapeutica al tumore minimizzando la dose assorbita dal tessuto sano circostante. La BNCT è una terapia promettente per tumori metastatici, infiltrati e per tutti quei tumori che non possono essere trattati con terapie convenzionali.

Nel passato le uniche strutture in grado di produrre un fascio neutronico adatto a questo tipo di trattamento, erano i reattori nucleari di ricerca. Negli ultimi anni, sono diventate disponibili nuove tecnologie per la produzione di fasci neutronici con le caratteristiche adeguate, utilizzando acceleratori di protoni.

In Italia, è attiva da molti anni una attività di ricerca che ha progettato e realizzato un acceleratore di protoni e un target di berillio per produrre un fascio neutronico per applicazioni cliniche della BNCT. Una parte importante di tale ricerca è la modulazione delle caratteristiche spettrali del fascio per ottimizzare la dosimetria nel paziente. A questo scopo, è stato sviluppato a Pavia un nuovo materiale per moderare il fascio ed ottenere lo spettro desiderato. Questo materiale costituisce il cuore del cosiddetto Beam Shaping Assembly (BSA), un dispositivo frapposto tra il target e il paziente per ottimizzare e collimare il fascio.

In questa tesi sono riportati studi sperimentali e computazionali sviluppati in questo campo. Si descrivono due campagne di misura condotta presso i Laboratori Nazionali di Legnaro (LNL) dell'INFN. Sono stati testati due prototipi di Beam Shaping Assembly costruiti presso l'officina meccanica della Sezione di Pavia dell'INFN. Questo set-up è stato concepito per poter accogliere uno spessore variabile del nuovo moderatore, costituito da blocchetti da fluoruro di alluminio litiato. Questo materiale è stato chiamato *Alliflu* ed è prodotto attraverso un processo di sintetizzazione innovativo, per il quale è stata costruita appositamente una macchina (*TT_Sinter*) presso l'officina meccanica della Sezione INFN di Pavia in collaborazione con il Dipartimento di Chimica dell'Università di Pavia. Il prototipo di BSA è stato testato con un fascio neutronico che ha le stesse caratteristiche spettrali del fascio clinico.

I dati sperimentali relativi all'analisi spettrale sono stati ottenuti utilizzando il rivelatore DIAMON, sviluppato e costruito presso il Politecnico di Milano in collaborazione con la start-up italiana Raylab. Le simulazioni sono state invece fatte con il codice di trasporto Monte Carlo MCNP6.2.

Un aspetto innovativo della campagna di misure presentata in questa tesi è l'acquisizione di uno spettro microdosimetrico ottenuto utilizzando un microdosimetro Tissue-Equivalent Proportional Counter (TEPC) sviluppato presso i Laboratori Nazionali di Legnaro.

Per la prima volta, uno spettro neutronico ed uno spettro microdosimetrico sono disponibili per un fascio neutronico prodotto da una reazione (p,n) su un target di berillio e moderato con fluoruro di alluminio sinterizzato.

Abstract

The work described in this thesis has been carried out in the field of Accelerator-Based Boron Neutron Capture Therapy (AB-BNCT) and developed in the framework of ENTER-BNCT, a project funded by the Commission 5 for technological and inter-disciplinary research of INFN. BNCT is a binary hadrotherapy which combines a low energy neutron beam, thermal or epithermal depending on the depth of the tumor, and a borated agent able to selectively accumulate in the tumor. The neutron capture reaction in boron produces two high-LET (Linear Energy Transfer) particles, an alpha particle and a lithium ion, which deliver a therapeutic dose in the tumor minimizing the dose released in healthy tissue due to the boron targeting of tumor. BNCT is a promising therapy for metastatic and infiltrated tumors and for the ones that cannot be treated with other conventional treatments.

In the past, the only facilities able to produce a proper neutron beam were research nuclear reactors. In recent years, new technologies have been developed and the production of a neutron beam has become possible using proton accelerators.

In Italy, a complete set of technologies to produce a clinical neutron beam has been designed and partially constructed. Research is ongoing to produce the most advantageous neutron beam regarding the spectral characteristics. For this, new materials have been developed to moderate and shape the neutron spectra produced with the accelerator designing the so-called Beam Shaping Assembly.

In this thesis, experimental and computational studies are presented in this field. Two measurement campaigns carried out at the Laboratori Nazionali di Legnaro (LNL) of INFN are described. These studies were carried out with two prototypes of a Beam Shaping Assembly built at the mechanical workshop of INFN, Unit of Pavia. This set-up has been conceived to host increasing thickness of a new moderator created at the INFN and University of Pavia, consisting in solid lithiated aluminum fluoride. This material is called *Alliflu* and it is produced through an innovative sintering process, for which a dedicated machine (*TT_Sinter*) was designed and built in Pavia. The prototypes have been tested in a neutron beam with the same spectral characteristics as the clinical beam.

The experimental data concerning the spectrum analysis were obtained using the detector DIAMON developed and built by Politecnico di Milano in collaboration with the Italian start-up Raylab. The simulations were carried out with the Monte Carlo transport code MCNP6.2.

An innovative aspect presented in this thesis is the acquisition of microdosimetric spectra obtained with a Tissue-Equivalent Proportional Counter (TEPC) developed at LNL.

For the first time, neutron spectra and microdosimetric spectra are available for neutrons emerging from the reaction (p,n) in a beryllium target and moderated with sintered aluminum fluoride.

Contents

Chapter 1

Boron Neutron Capture Therapy

1.1 A brief introduction to BNCT

Boron neutron capture therapy (BNCT) is a binary form of an experimental hadron-therapy. It is based on the synergistic action of low energy (≈ 0.025 eV) neutrons and a boron-enriched drug able to concentrate into the tumor cells [1]. BNCT is based on the nuclear reaction called neutron capture which occurs when an atomic nucleus absorbs a neutron forming a heavier nucleus:

$$n + {}^{A}_{Z}X \rightarrow {}^{A+1}_{Z}X^{*} \tag{1.1}$$

BNCT takes advantage from the high cross section (σ=3837 barn) of the stable isotope of boron-10 to capture thermal neutrons, this leads to the production of the unstable nucleus of ^{11}B which, afterwards, decays following two different branches:

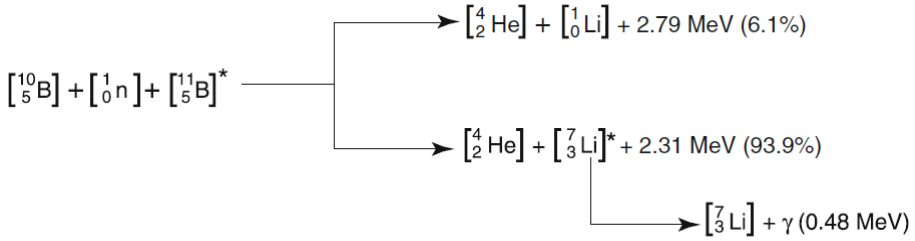

Figure 1.1: Description of the reaction ^{10}B(n,α)^{7}Li.

In both cases, two charged particles with high Lineal Energy Transfer (LET) are generated: an alpha particle (LET_{α}=150 keVμm^{-1}) and a lithium ion (LET_{Li}=175 keVμm^{-1}). Such high LET leads to short ranges in biological tissue, approximately 10 μm for ^{7}Li ion and 4.5 μm for the α particle. These distances are similar to the diameter of a cell, thus they cause irreversible damages to the DNA of the cells where they are created. Given the higher concentration of boron-10 in the tumor cells with respect to healthy ones, the particles deliver a high dose to the tumor while the damages to the healthy tissues are minimized due to a lower number of nuclear reactions in boron. BNCT is thus based on a

biological targeting rather than on a beam targeting and, for this reason, it is a potential therapy for the treatment of infiltrated, radio-resistant or disseminated tumors.

When neutrons penetrate the body, they interact with the components of the biological tissue other than ^{10}B; these elements and their cross sections are reported in Table 1.1.

Nuclide	Weight % in tissue	σN_C (barn)
H	10.0	0.332
C	18.0	0.0034
N	3.0	1.82
O	65.0	$1.8x10^{-4}$
Na	0.11	0.43
Mg	0.04	0.053
P	1.16	0.18
S	0.20	0.53
Cl	0.16	32.68
K	0.20	2.1
Ca	2.01	0.4
Fe	0.01	2.57

Table 1.1: Neutron capture cross-section value of elements and their weight in biological tissue.

Potentially, when neutrons interact with all these elements, they can produce radiation that deliver dose to the surroundings cells. However, the nuclear cross section values are at least two orders of magnitude lower than that of ^{10}B, hence, in most cases, the dose due to these interactions is negligible. The only elements that cannot be ignored because of their abundance in tissue are hydrogen and nitrogen. These produce gamma rays and protons which can interact with DNA:

$$n +^1 H \rightarrow [^2H] \rightarrow^2 H + \gamma(2.23MeV) \tag{1.2}$$

$$n +^{14} N \rightarrow [^{15}N] \rightarrow^{14} C + p(0.63MeV) \tag{1.3}$$

Deep-seated tumors are treated using more energetic neutron beams than the one used for shallow tumors. The epithermal neutrons are thermalized crossing the tissue layers before the tumor; the neutron energy decreases because they interact with hydrogen through elastic scattering and protons are set in motion, their energy is approximately half the energy of the interacting neutron and they deliver dose to the patient. The higher the energy of the beam, the higher is the dose delivered because of the elastic scattering. For this reason, when designing the beam, the tail of the spectrum at higher energies should be minimized. Moreover, since these protons and gamma rays deposit their energy both in normal and malignant cells, it is essential that the boron concentration in tumor is sufficient to absorb an adequate dose and that a significant tumor-to-normal tissue boron concentration ratio exists to guarantee a therapeutic dose ratio. The ideal

agent would be the one which collect ^{10}B only inside the tumor cell, nowadays such an agent does not exist. In clinical BNCT treatments the molecules used in clinical trials are boronophenylalanine (BPA) and sodium borocaptate (BSH), which ensure a boron concentration in the tumor in the range of 3-5 times its concentration in healthy cells. BSH accumulates outside the cell so that its effectiveness in damaging tumor cell at the same neutron fluence is lower because it is more difficult for the alpha particles and the lithium ions to reach the cell nucleus.

The BNCT treatments are thus carried out in two steps: first the borated agent is injected through intravenous infusion in the patient and then, after an adequate time which allow a proper accumulation of boron in the malignant cells, the patients is irradiated with a neutron beam of suitable energy spectrum.

The idea to use neutron capture reaction in cancer treatment was first theorized in 1936 by Locher, shortly after the discovery of neutron and the description of the reaction ^{10}B(n,α)^{7}Li [2]. The first attempts to use BNCT for the treatments of tumor date back to the '50s in USA, for Glioblastoma Multiforme (GBM), a fast-growing and aggressive brain tumor. During this first phase, the treatments did not lead to better outcomes than the conventional radiotherapy and all the patients died for progressive disease [3]. The causes were attributed to a non selective accumulation of the borated compounds, a poor depth-dose profile and incorrect evaluation of the in-patient dose due to fast neutrons and gamma rays. The research in BNCT field stopped for over thirty years in USA.

In the '70s and '80s Japaneses made great progresses in BNCT: Hatanaka and Mishima were two pioneers in this field. Hatanaka's group was the first one to use a new ^{10}B carrier called Disodium Mercaptoundechaydro-Closo-Dodecaborate (BSH) and they developed innovative approaches including the injection of heavy water in the patient in order to obtain better dose distribution [4]. Mishima developed a second borated carrier, the Boro-Phenylalanine (BPA) which, nowadays, is the mostly used in BNCT clinical trials. The innovations introduced led to significant increase of the survival time [5] [6].

In the early 90s' and in the 2010s' BNCT facilities have been developed worldwide, also in Italy, and many other tumors, such as head and neck tumors, skin melanoma, liver and lung cancer and pleural mesothelioma have been treated. After several phases, the potential of BNCT in addressing complicate and orphan tumors has been proven and it is now considered promising especially in view of the last technological improvements [7] [8] [9] [10] [11] [12] [13] [14] [15] [16]. In all the cited studies, patients were treated with reactor-based facilities (RB-BNCT) because the reactors were the only installations able to produce a beam with the appropriate features. And for many years they have remained the only facilities used [17]. In recent years the interest has gone from reactor-based facilities (RB-BNCT) to accelerator-based facility (AB-BNCT), as explained below in more details. The web page of the International Society of Neutron Capture Therapy (https://isnct.net/) reports a list of the existing AB-BNCT installations, the technology on which they are based and their purpose (clinical application or research).

1.2 Neutron sources

One of the pillars of an effective BNCT treatment is the availability of a suitable neutron beam. Thus, a pivotal aspect that must be addressed is the optimization of the beam characteristics desired for BNCT treatments. The aim is to increase the probability of neutron capture by boron nuclei in the tumor: the neutron capture cross section is inversely proportional to the neutron energy and for this reason a uniform distribution of thermal neutrons in the tumor volume is preferable. This means that the optimal energy distribution of neutrons before entering the body depends on the depth of the tumor. Figure 1.2 shows that an epithermal beam entering in tissue creates a thermal neutron flux which is maximum at a depth of 2-3 cm, the so called spare-skin effect, and it drops exponentially therefore. The penetration of the beam can be improved by increasing the average energy of the neutrons. On the other hand, a thermal beam falls off exponentially from the surface of the body. For this reason, an epithermal spectrum is better for tumors deep-seated in the body, instead a thermal beam is used for shallow tumors such as melanoma, or in case of open craniotomy as performed in some cases for glioma treatments [4].

In 2001, IAEA published a guideline, called TECDOC-1223, which established the characteristics that a BNCT neutron beam should have for treatments. The guideline was written for the treatment of brain cancer in a deep position and considered an epithermal beam produced by a reactor [18]. The characteristics are summarized in Table 1.2.

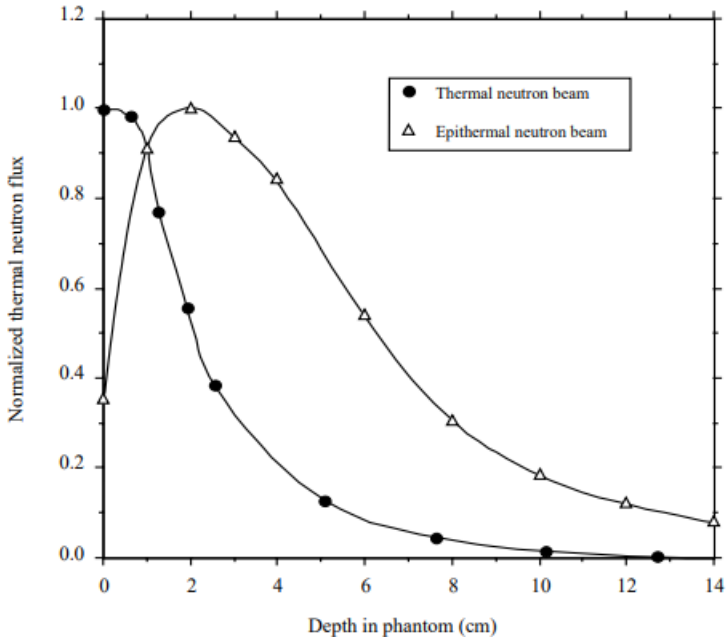

Figure 1.2: Comparison of flux-depth distributions for epithermal and thermal neutrons, taken from [18]

The two principal characteristics of interest are the quality and intensity of the beam;

quality refers to energy, types and relative intensities of the radiation components present in the spectrum, intensity is related to the flux of epithermal neutrons as emerge from the beam shaping assembly.
The intensity determines the irradiation time: as it is recommended to perform a treatment within 1 hour, a neutron flux higher than 1x10^9 cm^{-2}s^{-1} is necessary. This recommendation depends on boron concentration achievable in tumor: if the ratio of boron concentration between tumor and normal tissue would be higher, then the requirements on neutron flux could be less stringent.

The beam quality under free beam conditions is determined by four parameters:

- *the fast neutron component:*
  fast neutrons (energy >10 keV) accompany the incident beam and they can interact with biological tissues, produce high LET protons which can induce biological effects. For this reason a filter is usually introduced in the beam shaping assembly. The dose delivered by this contamination should be less than 2x10^{-13} Gy cm^2;

- *the gamma ray component:*
  gamma rays contaminate the beam, they have a long range and this results in dose delivered to a healthy tissue distant from the tumor (non-selective dose). Gamma radiation is also produced in the reactions (n,γ) when neutrons interact with hydrogen, other than in the reaction with ^{10}B. This components cannot be removed. The dose delivered by this contamination should be less than 2x10^{-13} Gy cm^2;

- *the ratio between the thermal flux and the epithermal flux:*
  when using an epithermal beam for deep-seated tumors, thermal neutrons in the beam deliver undesired dosed to healthy tissue their contribution should be minimized and the ratio between thermal and epithermal neutron flux should be lower than 0.05 ;

- *the ratio between the total neutron current and the total neutron flux:*
  this ratio provides a measure of the fraction of neutrons that are moving in the forward beam direction. The ideal value is 1, which indicates that all neutrons are moving forward, Of course it is impossible to achieve this ideal condition and it is acceptable a ratio higher than 0.7. A high value is important because (1) it limits the off-beam organs irradiation, and (2) it permits flexibility in positioning the patient along the beam central axis.

The beam quality is also determined by its size and shape: circular apertures with 12 to 14 cm diameter are the most used.

In the present times, these guidelines are being reconsidered in light of the extensive experience gained in research and in clinics. A new IAEA TecDoc is being prepared, and it is currently in the phase of final revision [19]. The new knowledge produced in the treatment planning and in the patient treatment shows that it is not convenient to evaluate the beam suitability on the sole basis of its physical characteristics as described above. Yet, it is possible that a beam which does not comply with the cited IAEA requirements is still useful and effective for the clinical treatment. This has been demonstrated for the beam relevant for this work in the publication [20]. The recent approach is thus to use

Characteristics	Desired facility performance
energy	$\sim$0.4 eV < E < $\sim$10-20 keV
intensity	> 1x10^9 n $cm^{-2}s^{-1}$
treatment time	< 1 hour
n_{th} and γ beam contamination	< 2x10^{-13} Gy cm^2
th/epth	< 0.05
collimation	J/ϕ > 0.7

Table 1.2: Summary of the characteristics desired for a neutron beam used in BNCT.

the IAEA guidelines to design a neutron beam, but to evaluate its potentials through a simulated treatment planning. The obtained in-patient dosimetry can be used to calculate figures of merit such as Tumor Control Probability or Normal Tissue Complication Probability which allow establishing clinical criteria to state if the neutron beam is effective for BNCT.

There are four different sources that have been considered in the TecDoc to produce a neutron beam for BNCT: fission reactors, accelerators, compact neutron generators and a source of californium-252. Clinical BNCT applications have been conducted so far nuclear reactors and in facilities based on accelerators (more details are given below). A ^{252}Cf source would provide a compact facility but it would need frequent replacement of ^{252}Cf because of its 2.6 year half-life and it is expensive. Furthermore, a source of the order of 1 g would be necessary, which is difficult to produce. Regarding compact neutron generators, they can provide high yield of neutron using D-D o D-T fusion reactions. In recent years attempts have been made to use this kind of sources in order to house the complete BNCT system inside a medical facility [21] [22].

1.2.1 Reactor-based BNCT facility

The production of a neutron beam in a reactor is based on nuclear fission:

$$n + {}^{235}_{92}U \rightarrow {}^{140}_{56}Ba + {}^{93}_{36}Kr + 3n + Q \tag{1.4}$$

The cross section of the interaction in reported in Figure 1.3, specifically when the neutron is thermal (E$\approx$0.025 eV) the cross section is $\sim$500 b as it can be seen in the first graph of Figure 1.3.

Neutrons emitted by the reactor (prompt neutrons) have a continuous energy distribution characterized by a mean energy of 2 MeV and a most likely energy of 0,7 MeV. The distribution is reported in Figure 1.4. In order to use neutrons produced in a reactor for a clinical BNCT treatment, it is necessary to add a Beam Shaping Assembly (BSA) between the patient and the neutrons source. The BSA must be added in the facility because most of the time the reactor used is not BNCT-dedicated and the characteristics of the beam which is produced are not suitable for a treatment. The BSA (Figure 1.5) consists of several elements, each of which has a specific function ad it is made up of different materials: moderator, filters, reflectors and a collimator. Moderators change the energy range of fast neutrons produced during the reactions (spectral shifting). They are

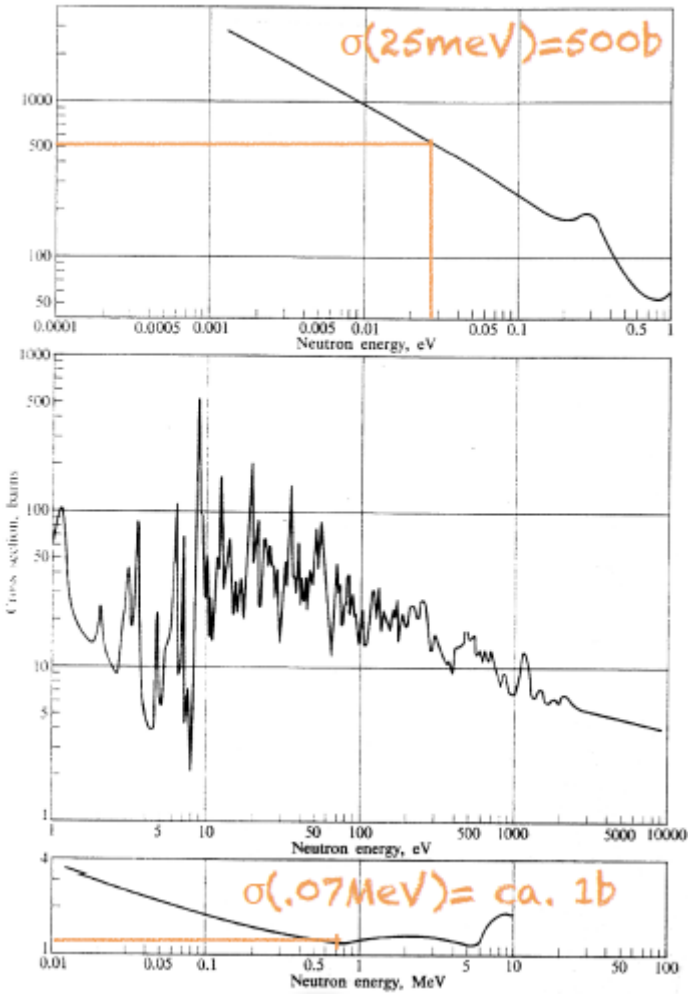

Figure 1.3: Cross section of the fission of U-235.

made of materials with low atomic numbers, it should be highly resistant and stable and the nuclei produced by the interaction of neutrons should decay quickly. The materials use most frequently are aluminum, carbon, sulphur, sapphire (Al_2O_3), AlF_3, D_2O and TEFLON (CF_2) or their combination such es FLUENTAL [23].

Filters are used to capture high energy neutrons and they are made of materials whose cross section has a maximum of transmission for the neutrons with the desired energy and a maximum of interaction for the neutrons which have to be removed from the beam. The most used materials are Ni_{60} combined with B_{10} or S_{32} or Fe_{56}. Filters are also useful to reduce the gamma contamination, for this purpose the materials they are made of are concrete doped with B_{10} or Li_6, the latter is better because it does not emit gamma radiation when it interacts with thermal neutrons. If the desired beam is epithermal, the filter that should be used is doped with cadmium because it is transparent to epithermal neutrons but it absorbs thermal neutrons. Reflectors, made of lead or graphite, are necessary to redirect to the beam neutrons that are escaping outside along

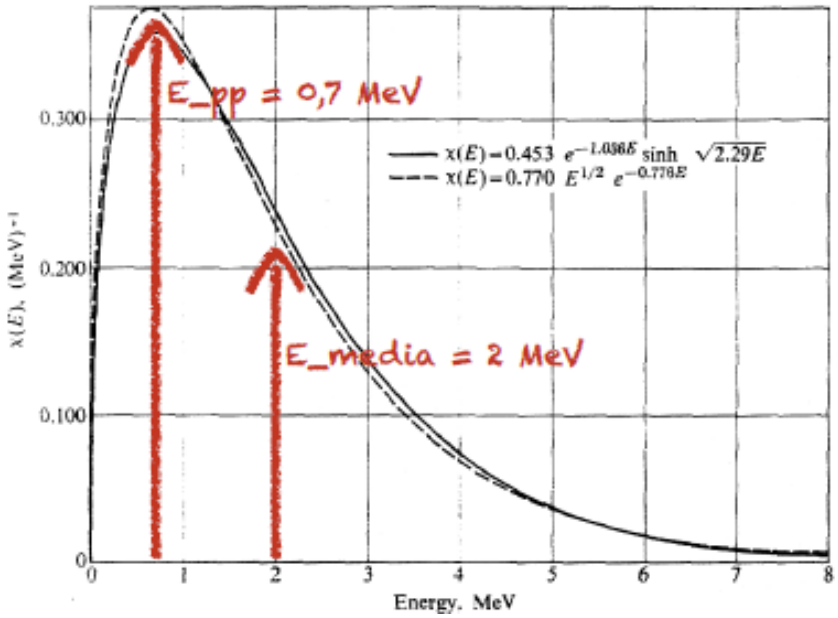

Figure 1.4: Energy distribution of the prompt neutrons: the arrow on the left points to the most likely energy (0.7 MeV) and the arrow on the right points to the mean energy (2 MeV).

a wrong direction. Lastly, collimators are arranged in the last section of the BSA before the patient so that neutrons which are not moving along the beam direction are absorbed. Collimators also give the beam the desired shape. The materials used for collimators are compounds of B_{10} or Li_6 such as polyethylene doped with B_4C and $^6Li_2CO_3$.

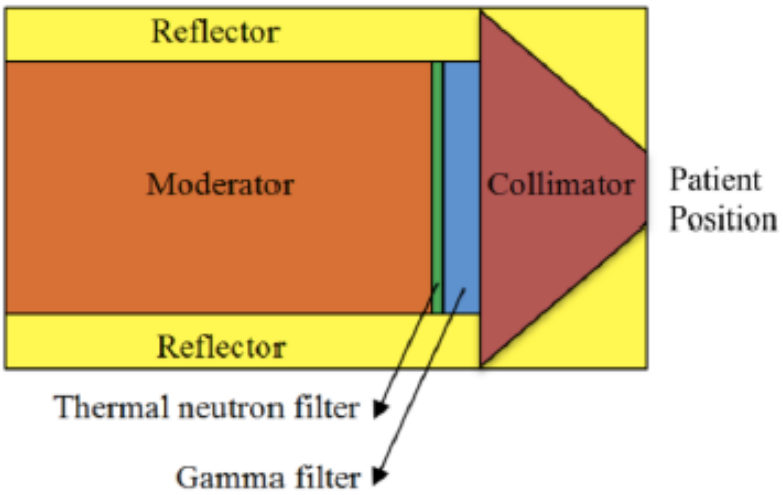

Figure 1.5: Outline of a BSA with its typical elements.

In recent years, the research is focusing on developing accelerator-based BNCT facilities because reactors have several problems. Reactors are not easy to install in healthcare settings because of aspects such as authorization issues, safety and maintenance requiring high qualified employees. The facilities are large, hence they cannot be constructed inside hospitals. For these reasons, BNCT has been carried out in Institutions already equipped with reactors, creating irradiation facilities for limited clinical trials. However, in most cases, reactors are not dedicated to the therapy, therefore they can be used for a short amount of time during the week. Finally, in some Countries, as Italy, reactors arise acceptability issues which make it difficult to promote new installations based on this technology.

1.2.2 Accelerator-based BNCT facility

Accelerator-based facilities overcome most of the problems which characterize the reactors. First of all, these machines are similar to those typically installed in conventional radiotherapy wards. Their dimensions allow the construction of relatively small dedicated centres or new wings of existing hospitals. Accelerators are socially accepted and their cost is lower than that of reactors. Furthermore, they are easier to operate and maintain and the level of qualification of the operators is less demanding than for reactors. From the point of view of the neutron spectra obtained, the advantage is a lower contamination of fast neutrons comparing to the beams produced by a reactor [24].

The new technology of low-energy, high-current accelerators allows producing stable, high-intensity neutron beam through a nuclear reaction induced by charged particles: a projectile (proton or deuterium) are sufficiently accelerated to overcome the repulsive Coulomb barrier, they impinge on a target ad produce neutrons. Endothermic reaction, which requires a minimum threshold energy, are preferred because the neutrons produced are slower so that they need a smaller BSA in order to be moderated. There are many possible reactions which can be used to produce a neutron beam, reported in Table 1.3, but the most used are ^{7}Li(p,n)^{7}Be and ^{9}Be(p,n)^{9}B.

The most popular reaction for AB-BNCT is ^{7}Li(p,n)^{7}Be. The threshold energy for the proton is 1.880 MeV and the Q value of the reaction is -1.644 MeV. It can bee seen in Figure 1.6 that the cross section has a maximum around the neutron energy of 2.3 MeV, so that it is important to accelerate protons to a proper energy in order to make the reaction convenient. The necessary neutron flux of the order of 10^{9} n cm^{-2} s^{-1} in requires proton currents of the orders of tens of mA which is technologically challenging because lithium has a low melting point (180.5 °C) and a low thermal conductivity (85 W m^{-2} K^{-1}). These are not the only problems of lithium targets, Li is highly reactive with oxygen and it is activated when it reacts with neutrons. Different technological strategies have been developed to face these problems, for example in Israel a liquid lithium target has been studied [25].

The other most studied reaction is ^{9}Be(p,n)^{9}B. The threshold energy is 2.06 MeV. The yield of the reaction at 2.3 MeV is lower than the one of protons on Li at the same energy, as shown in Figure 1.7, and in order to obtain a comparable beam the protons

Reaction	E_{th} (MeV)	E_{in} (MeV)	Tot production (n/mA s)	Fraction E_n<1 MeV (%)	$E_{n,max}$ (keV)	$E_{n,min}$ (keV)
^{7}Li(p,n)^{7}Be	1.880	1.880	0	100	30	30
		1.890	$6.3x10^{9}$	100	67	0.2
		2.500	$9.3x10^{11}$	100	787	60
		2.800	$1.4x10^{12}$	92	1100	395
^{9}Be(p,n)^{9}B	2.057	2.057	0	100	20	20
		2.500	$3.9x10^{10}$	100	574	193
^{9}Be(d,n) ^{10}B	0	0	0	50	3962	3962
		1.500	$3.3x10^{11}$	50	4279	3874
^{13}C(d,n)^{14}N	0	0	0	75	4974	4964
		1.500	1.9x1011	70	6772	5616
^{12}C(d,n)^{13}N	0.327	0.327	0	100	4	3
		1.500	$6.0x10^{10}$	80	1188	707
d(d,n)^{3}He	0	0	0	0	2451	2451
		0.120	$3.3x10^{8}$	0	2898	2123
		0.200	$1.1x10^{9}$	0	3054	2047
t(d,n)^{4}He	0	0	0	0	14050	14050
		0.150	$4.5x10^{10}$	0	14961	13305

Table 1.3: All the reactions that can be performed in an accelerator-based BNCT facility.

should have a energy of about 4 MeV. The consequence is that the neutrons produced have a higher energy than the one produced in the p+Li reaction, thus the technological requirement is an accelerator able to deliver a higher proton current at a higher energy and a bigger beam shape assembly.

Targets made of beryllium have the issue called blistering which is the result of the low gas permeability of beryllium which causes breaks. Furthermore, beryllium is toxic when it becomes powder but it is easier to handle compared to Li because it is not chemically active and its melting point is 1287 °C.

In Italy, at the Laboratori Nazionali di Legnaro (LNL), an accelerator which can produce an intense neutron flux suitable for BNCT has been designed and constructed by INFN, the National Institute of Nuclear Physics. The machine is a Radio Frequency Quadrupole (RFQ) proton accelerator developed within the MUNES (MUltidisciplinary NEutron Source) project [27]. It is able to accelerate 5 MeV protons with a 30 mA current in Continuous Wave (CW) mode and, coupled with a bryllium target, the proton beam can produce a neutron intensity of 10^{14} s^{-1} [28]. The RFQ, as shown in Figure 1.8, is made of six modules of 1.2 m each, which are assembled by means of ultra high vacuum flanges.

The article *A novel approach to design and evaluate BNCT neutron beam combining physical, radiobiological, and dosimetric figure of merit* by Postuma et al. [20], describes the design of different BSAs for the RFQ+Be target system to produce a suitable beam for deep-seated tumors. This work proposes a method to evaluate the dosimetric performance of the beam through the simulation of a treatment plan in a typical case of head and

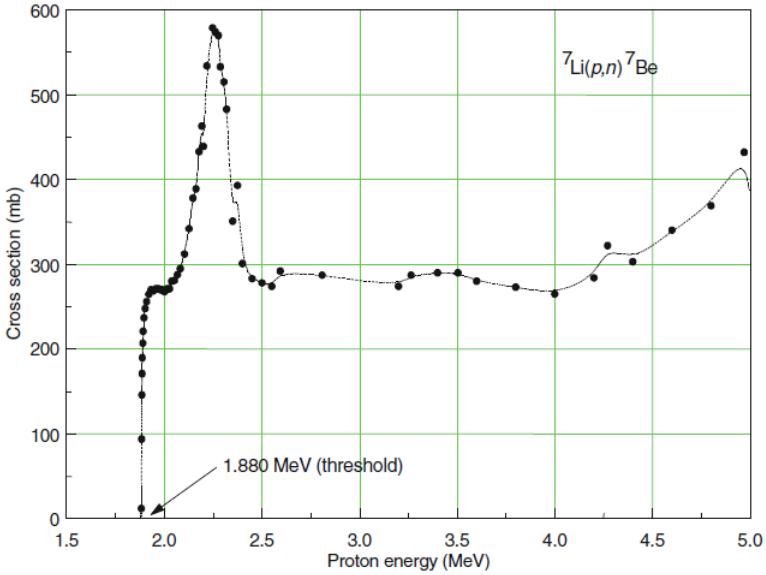

Figure 1.6: Cross section of the reaction ^{7}Li(p,n)^{7}Be [26]

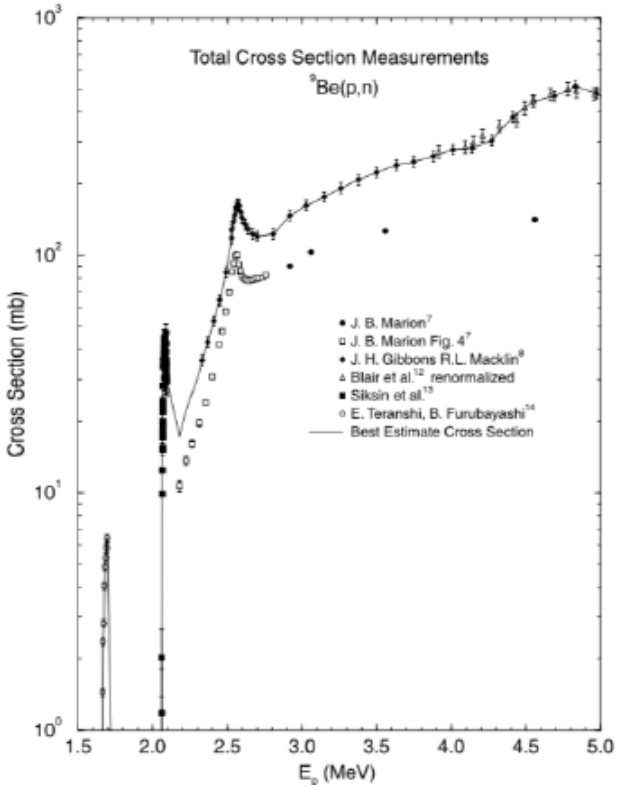

Figure 1.7: Cross section of the reaction of ^{9}Be(p,n)^{9}B [26]

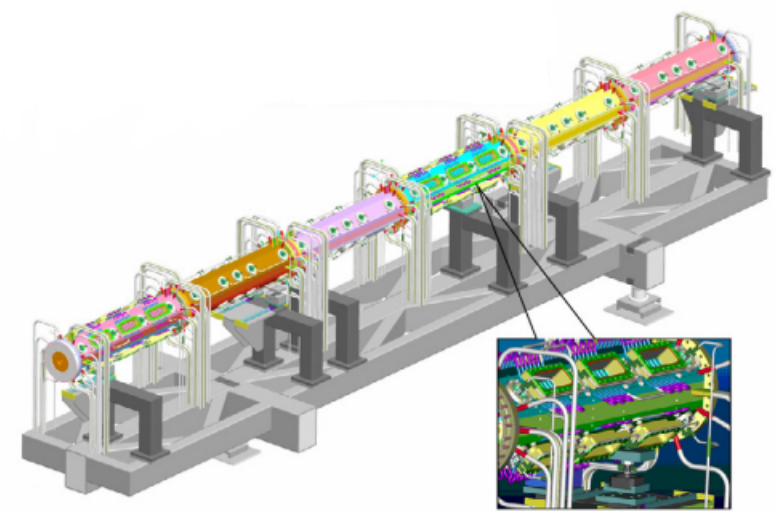

Figure 1.8: Outline of the RFQ designed and constructed at LNL, Italy.

neck tumor. The conclusions show that one of the evaluated design performs in the same way as a beam used to treat several hundreds of patients in a reactor facility in Finland. This enables the choice of that BSA design, based on a new material called *Alliflu*, as an adequate solution for a clinical facility based on the RFQ and the Be target.

Figure 1.9 summarizes the three most important parts of the technology needed to produce the clinical neutron beam and the solutions implemented by INFN: the RFQ accelerator, the Be target and the designed BSA based on *Alliflu*.

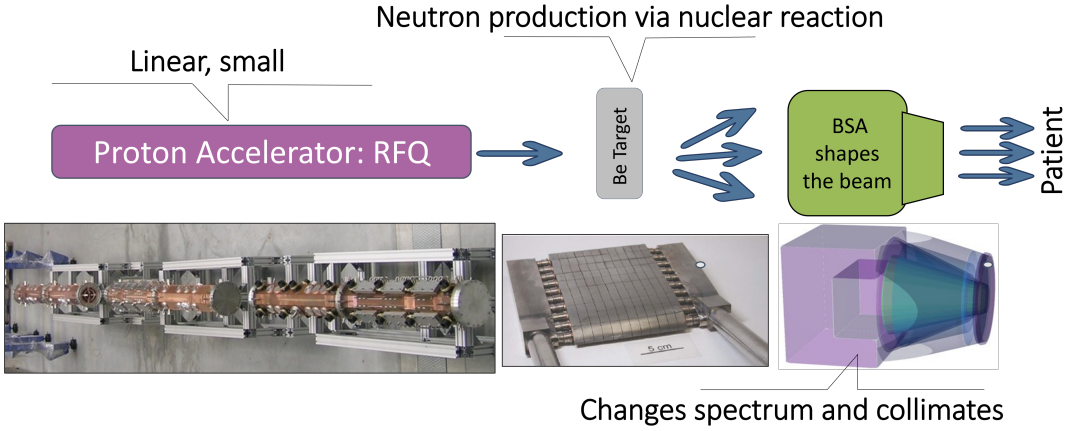

Figure 1.9: Scheme of a AB-BNCT facility with the solutions implemented by INFN: the RFQ accelerator, the Be target and the designed BSA for the treatment of deep-seated tumors.

Alliflu material, obtained as described below, was never tested experimentally concerning its moderation properties. The necessity to validate the Monte Carlo simulations

ultimately used to calculate the dosimetry in patient, motivated a project for extensive measurements. The experiments have been designed at a facility able to produce a beam characterized by the identical neutron spectrum produced with the RFQ, although with lower intensity, that is a 5 MeV proton beam coupled to a beryllium target. This goal has been pursued in the framework of the ENTER-BNCT project funded by Commission 5 of INFN. ENTER-BNCT involves 4 different INFN Units: Pavia, Turin, Laboratori Nazionali di Legnaro (LNL) and Laboratori Nazionali di Frascati (LNF). The Working Packages of the project relevant for this thesis are the realisation of a BSA prototype and the production and test of a beryllium target. The aim of the design of the BSA prototype was to build a set-up with the same materials of the clinical BSA and able to house a moderator with modular thickness. The clinical BSA would be difficult to produce also in terms of costs and its dimensions would make the measurements very difficult because the intensity of the neutron flux available at the experimental facility is significant lower than the one of the RFQ accelerator. The target fabricated in the frame of ENTER-BNCT is made up of a thin beryllium layer deposited on a vanadium support and a copper backing in order to solve the blistering and cooling problems.

In this thesis I describe some aspects of the work related to these goals, as I had the opportunity to work at the experimental facility for a measurement campaign dedicated to the new target test and to the neutron spectrometry and microdosimetry using the BSA prototype.

In Chapter 2 the CN facility at the Laboratori Nazionali di Legnaro of INFN (where the experiments took place) and the experimental set-up are described with a focus on the target used to produce the neutron beam, the Beam Shaping Assembly and the new moderator developed and produced at University of Pavia.

In Chapter 3 the experimental set-up and the detector used to study the neutron spectra of the beam after the BSA equipped with different layers of *Alliflu* are presented. In the same Chapter the experimental and simulation results will be reported and discussed.

In Chapter 4 the basics of theoretical and experimental microdosimetry are explained. In this Chapter, the most used microdosimeters, tissue-equivalent proportional counters and solid-state detectors, are described; especially, the borated TEPC with interchangeable cathodes developed and built at LNL is discussed because it is the one used during this thesis work. The experimental spectra are shown and discussed.

Finally, Chapter 5 shows some preliminary results for the simulations of microdosimetry spectra and the last Chapter draws some conclusions on the presented work.

Chapter 2

The CN facility at LNL and the experimental set-up

This Chapter is dedicated to the description of the experimental set-up prepared for the measurements shift carried out from the 11 July 2022 to 21 July 2022, developed within the ENTER-BNCT project. Specifically, the CN accelerator present at the Laboratori Nazionali di Legnaro (LNL) will be briefly described and then the beam shaping assembly, the Alliflu moderator and the target used will be illustrated.

2.1 A brief description of the CN-accelerator, LNL-INFN

The CN-accelerator (https://www.lnl.infn.it/cn/) was the first device to be installed in 1961 at the Laboratori Nazionali di Legnaro. The AC-accelerator is a Van de Graaff electrostatic machine and it is a vertical accelerator about 7 m tall. The high voltage terminal (in the past it was about 7 million Volts, from 2006 the highest voltage is 6 million Volts) is on the top of the structure and the voltage, from 6 MV to 0 V (at the ground), is uniformly distributed by means of a resistor chain. The whole accelerator is contained inside a metal tank, filled with a mixture of gasses (N_2+SF_6) at a pressure of 12-14 bar (Figure 2.1). The gas has an insulating function. On the top of the accelerator the source generates the particles that need to be accelerated. They are protected by a Faraday cage so that they are not affected by the voltage. The CN device can accelerate many types of particles such as positive ions of H or He.

The particles are downward driven thanks to a proper deflection and electrostatic focusing system and, as soon as they exit from the terminal region, they are affected by the electric field along the pipe and they are accelerated to a final energy E=qV, where q is the ion charge and V is the difference between the terminal and the ground voltage. The last step is to guide the particles to the target: there are seven different lines at different angles.
This accelerator is employed for research in the field of fundamental and applied physics.

During the ENTER-BNCT measurements shift, a 5 MeV proton beam has been generated at the CN to produce neutrons. The current that can be generated for such experiments is limited by the radioprotection restrictions. A monitor detects the ambient dose

Figure 2.1: CN-accelerator at LNL.

due to neutrons generated at the target and works as an interlock which blocks the beams in case the limit is reached. In the described set of measurements, with an appropriate shielding system (flex-boron sheets, borated water and polyethylene and lead blocks in addition to the beam shaping assembly reported in Figure 2.2), we were able to work at 4 μA proton current. The line at 0° has been used for all the measurements.

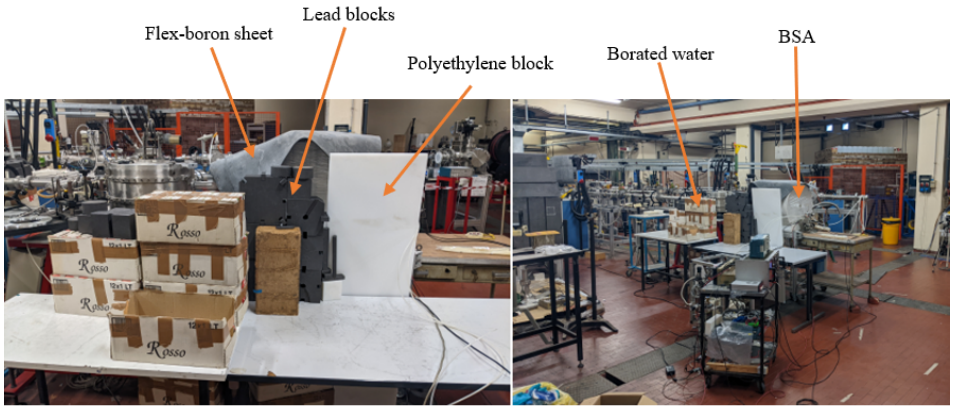

Figure 2.2: The shielding constructed during the ENTER-BNCT measurements shift.

2.2 Target

The target used during the measurements was a beryllium-vanadium-copper (BeVCu) target with a diameter of 2 cm and the beryllium layer is 50 μm thick (Figure 2.3). This target has been developed in the frame of ENTER-BNCT project to overcome the problem of blistering arising in the thick beryllium target. Previous measurement campaigns had been carried out using a Be thick target, with no structure for the cooling and the monitoring.

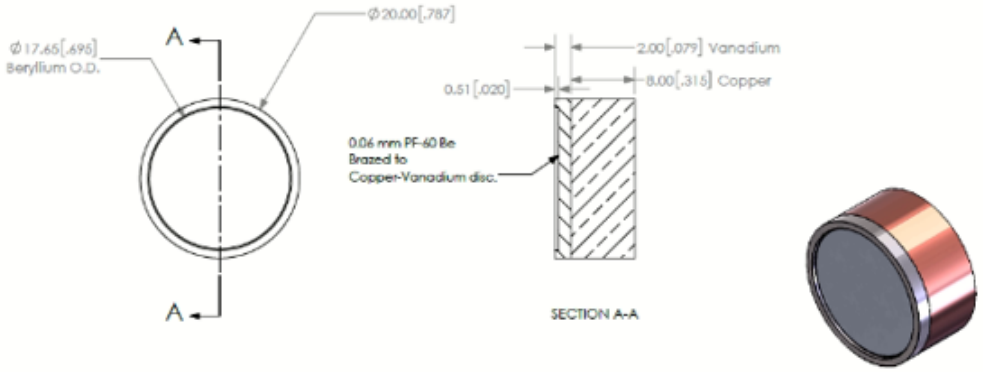

Figure 2.3: BeVCu target and its dimensions.

The choice to use a beryllium target has been made because of the reasons reported in Chapter 1 concerning the p+Be and especially for the fact that Be is more easily handled than Li. A consequence of this choice is the energy of the proton beam imprinting on the target which is 5 MeV, easily reachable with a RFQ. The position of the Bragg peak of 5 MeV protons that hits beryllium allows the use of a thicker beryllium layer, in the range of 50-100 μm thick instead of a target $\sim$1 μm thick. Such a target is easier to produce and manage.The positioning of the target, which is skewed with respect to the beam line, gives an effective thickness equal to 160 μm

As shown in Figure 2.3, the target is made up of three different layers: beryllium, vanadium ad copper, each with a very specific function. A structure like this is the result of several studies carried out in recent years. The first prototype built and tested at LNL consisted of only two layers, one of beryllium and one of copper, the latter necessary to improve the thermal conductivity. It has been shown that this configuration arises serious blistering problems so that the target breaks or swells (image (a) in Figure 2.4). In the second configuration that was taken into account, the copper layer was replaced with vanadium, which solves the blistering problem, having a better gas permeability, however vanadium has a low thermal conductivity (30.7 W m^{-1} K^{-1}). Therefore the target, despite not showing blistering, overheats (image (b) and (c) in Figure 2.4) with consequent damages.

For all these reasons, the final target has been built in three layers: the copper layer (8

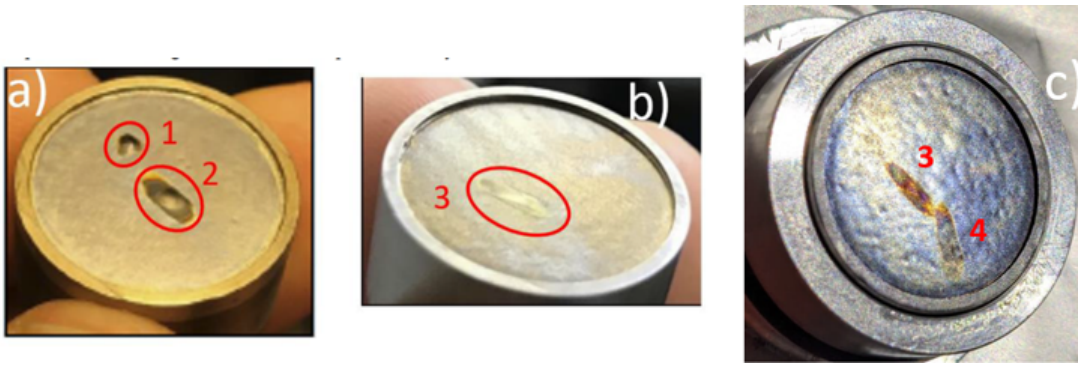

Figure 2.4: (a) Beryllium-Copper target: 1) and 2) are the signs of the blistering; (b) and (c) Beryllium-Vanadium target: 3) and 4) are the signs of the overheating.

mm thick) to overcome the overheating problem and the vanadium layer (2 mm thick) to solve the blistering problem. This configuration also made the target less activated after the irradiation compared to the BeCu solution. For the cooling, pipes have been added to inject water inside the target channel (the blue tube in the upper picture of Figure 2.6) and air around the containing system (the green tube in the upper picture of Figure 2.6).

The BeVCu target has been installed and assembled before the start of the ENTER-BNCT shift. It was inserted inside the structure shown in Figure 2.6, which connects the accelerator pipe to the target. This is made up of steel and polyethylene and it includes the beam collimator. The target fits in the system at an angle of 71.68° with respect to the beam direction. The whole structure is is made up of several components as it can be seen in Figure 2.5.

Figure 2.5: Picture of the components of the target.

The assembly procedure carried out in LNL during the cited shift, consists of several steps. The first one is cleaning all the components, included the o-rings which are used to guarantee the vacuum but they are not pictured in Figure 2.5, with isopropyl alcohol. Then the target has been inserted in the cooling structure using the conductive compound RS 217-3835 to improve the dispersion of the heat. It was assembled in the pipe which connects it to the beam line; the collimator and the repeller are included and spaced out with nylon disc to guarantee electric isolation of the components. The repeller is included in the structure to measure the current at the target with great precision.

Figure 2.6: Assembled target. Top: a close-up sight of the installed target with the cooling system (blue pipes for water and green pipe for air), bottom: a view of the target connected to the beam pipe.

2.3 *Alliflu*: a new neutron moderator

As anticipated in the Introduction, the best material for the core of the BSA has been determined to be lithiated aluminum fluoride (AlF_3+LiF). Monte Carlo simulations have shown that AlF_3+LiF can provide an epithermal flux at the beam-port greater than 10^9 cm^{-2} s^{-1} with acceptable thermal and fast neutron contamination and gamma dose when introduced in the BSA structure around the Be target [20].

Aluminum fluoride exists only in powder, which obviously is not the best option because it is inadequate to produce a compact, stable and uniform BSA with the required density and mechanical properties. Sintering was used in Pavia to combine powdered AlF_3 and LiF to create a solid material.
Sintering is a process in which high temperatures and pressures transform a material with low aggregation into a solid. Sintering can be considered as a technique that densifies powders while reducing interstitial porosity, without melting the material during the process.
The procedure of densification for the compound of our interest is complicated by a significant high-temperature volatility. A custom machine called *TT_Sinter* (Figure 2.7) was designed in collaboration between University of Pavia (Department of Chemistry) and INFN, Unit of Pavia and built at the local INFN mechanical Workshop. The machine exploits the Field Assisted Sintering Technique (FAST), a process based on a modified hotpressing. The AlF_3+LiF material produced has a density in the range from 70 to 99% of the theoretical one and it has been proven to be easily manageable. It is called *Alliflu* [29].
The production of *Alliflu* can be summed up in the following steps:

- preparation of a suitable combination of AlF_3 and LiF powders;
- the powders previously mixed is poured into a graphite die;
- the die is placed between two graphite punches inside the vacuum chamber of the TT_Sinter device;
- the die is heated up to the desired temperature;
- compression with the desired pressure;
- cooling and extraction of the sintered sample.

Ideally, the final material should be perfectly homogeneous and uniform. The mechanical resistance of the *Alliflu* core is another critical consideration. Any material loss is particularly undesirable since it could change the neutron moderation thus altering the spectral properties and possibly degrading the therapeutic quality of the beam. Therefore, it is crucial to guarantee that the main BSA material has good mechanical resistance for the safety of both workers and patients. Furthermore, a considerable radiation dose is expected for the BSA over the course of the clinical BNCT facility, in particular since

the neutron flux at the beryllium target is greater than 10^9 n cm^{-2} s^{-1}. Some of the neutrons that interact with *Alliflu* are trapped by Li-6, which emits charged particles. These particles may cause changes in the microstructure, such as cracking. These properties has been tested in a previous study and is still underway [29].

(a) (b)

Figure 2.7: The sintering machine called TT_Sinter. a): the machine with the door of the electronic controls open. b): the machine closed with the carters. The PLC for the interaction is visible on the door. The pressure,the heating and the heating ramp can be set via the PLC.

2.4 BSA prototype

The various stages of the BSA prototype design are described in this section.

The goal was to design and build a prototype that embodied the key elements of the BSA created for the RFQ in order to experimentally verify how well the BSA materials work together to moderate neutrons. As mentioned above, this structure is not intended to be a replica of the clinical BSA. Instead, it was intended to build a model of the BSA enabling the collection of data regarding the impact of various materials on the neutron spectrum and Monte Carlo validation.

The preliminary experiments are reported in the Master thesis by Gabriele Parisi [30].

These were carried out at CN with bricks of *Alliflu* but without the whole BSA structure. Based on simulations previously run, beam characteristics and available beam-time, the spectra of the open-beam, without moderator, and with 2, 4 and 7 cm bricks of *Alliflu* positioned in front of the target were collected. Two detectors were used, one to study the neutron spectrum with high precision (ACSpect) and one to study the attenuation of the beam after crossing increasing moderator thickness (DIAMON). The results are published in [31].

The following step consisted in testing the moderator endowed with reflecting materials and a collimator, to improve the directionality of the beam. In these new measurements the ACSPect detector could not be used, because its low efficiency does not allow short-time data taking given the neutron flux produced at CN.

The process to design the BSA prototype was carried out through simulations [29]. The neutron flux was calculated at the beam-port and at progressively farther intervals along the direction of the beam: at the beam-port, in two concentric disks with a radius of 2.5 and 12 cm, and then at distances of 20, 40, 60, 80, and 100 cm. To verify the collimation, the neutron current was also simulated in concentric discs centred on the beam axis as a function of the distance from the beam-port and varying the radius. To distinguish the contributions of thermal, epithermal, and fast neutrons, three energy bins were studied.

Two configurations have been finally selected for the construction, on the basis of their effectiveness in collimation and of the spectral modulation obtained by changing the moderator thickness. The first configuration (Figure 2.8) consist in a 5 cm thick lead cylinder (reflector) with a cylindrical housing for the insertion of 5 cm diameter *Alliflu* elements. The length of the reflector is 25 cm. The reflector is surrounded by a 1 cm thick absorber of borated polyethylene. A collimator of borated polyethylene, 25 cm thick leaving a 5 cm diameter beam port ends the structure. The collimator is 25 cm long.

The *Alliflu* elements can be housed in the core of the BSA prototype, inside the cylindrical reflector, allowing measurements with variable moderator thickness from 0 to 25 cm. Figure 2.9 shows the prototype constructed at the mechanical workshop of INFN, Unit of Pavia.

This version of the BSA prototype was tested in a measurement campaign at the CN in September 2021. Figure 2.10 shows the BSA positioned in front of the 0° proton line at CN. The cone shields the DIAMON detector (see below for further details) to acquire the radiation background.

The second configuration is shown in Figure 2.11. It consists in adding a shell made of polyethylene to configuration 1, with the aim of improving the moderation as well as the absorption of ambient radiation.

The simulation of the measurements performed in both campaigns have been run in this thesis work, taking into account the precise geometry and the characteristics of 7 packages of *Alliflu* bricks, inserted in the BSA for the spectra acquisition with the two BSA configurations.

The polyethylene additional shell in the second configuration was extended towards the target to better shield the neutrons emerging in all directions. This strategy plus the

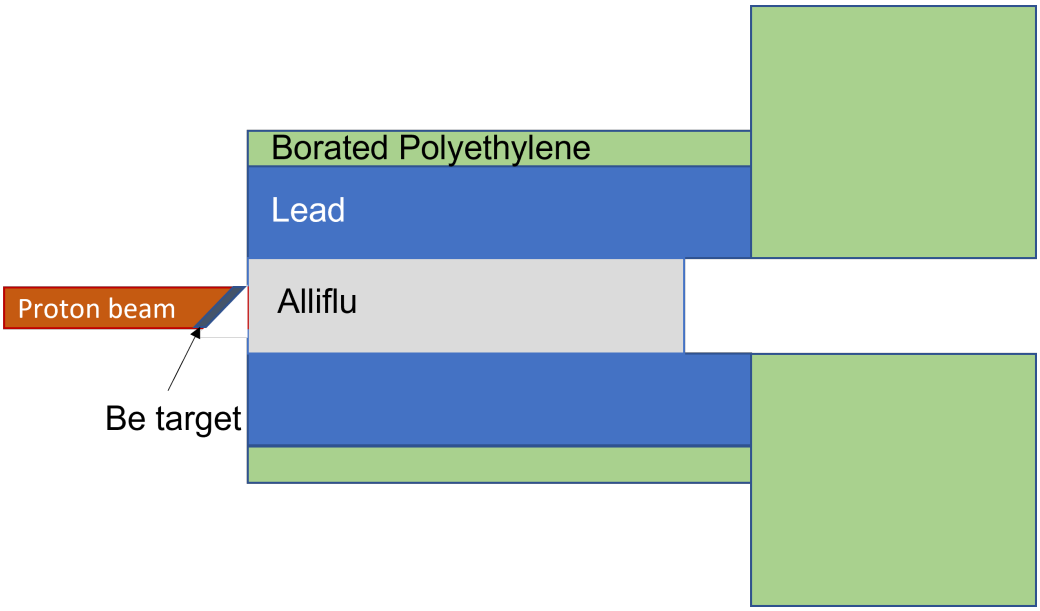

Figure 2.8: First configuration of the BSA prototype. Not in scale.

Figure 2.9: First configuration of the BSA prototype built at the mechanical workshop of INFN, Unit of Pavia.

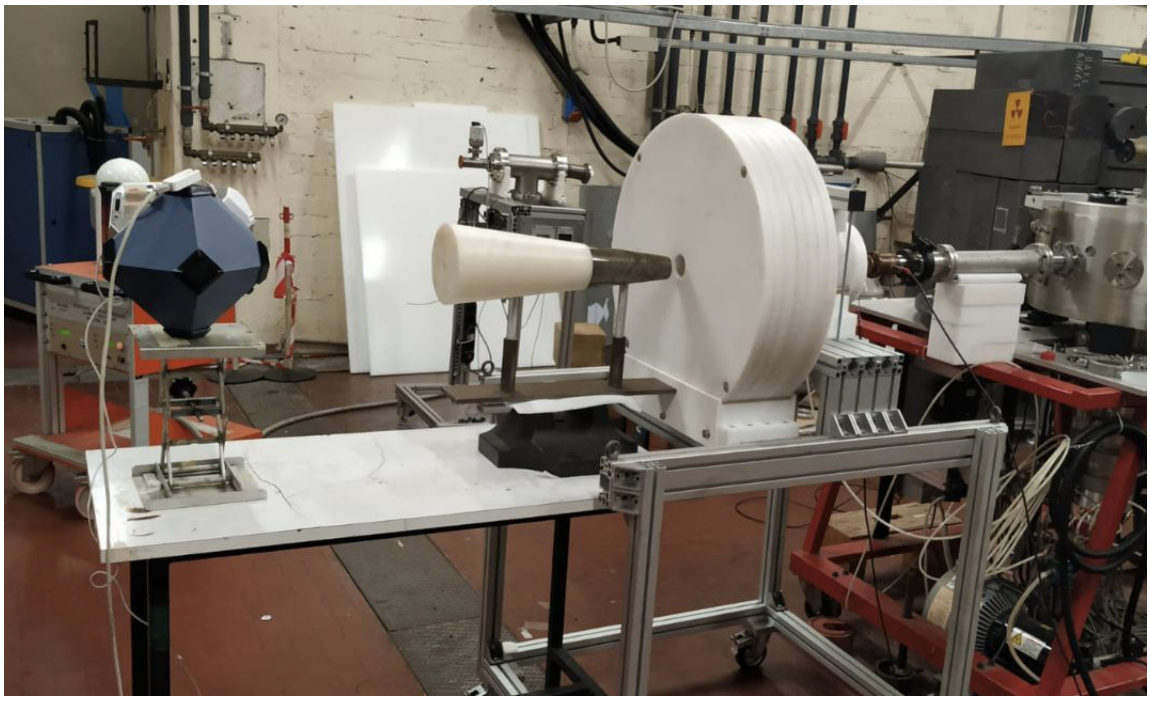

Figure 2.10: First configuration of the BSA prototype positioned in front of the 0° line at the CN facility

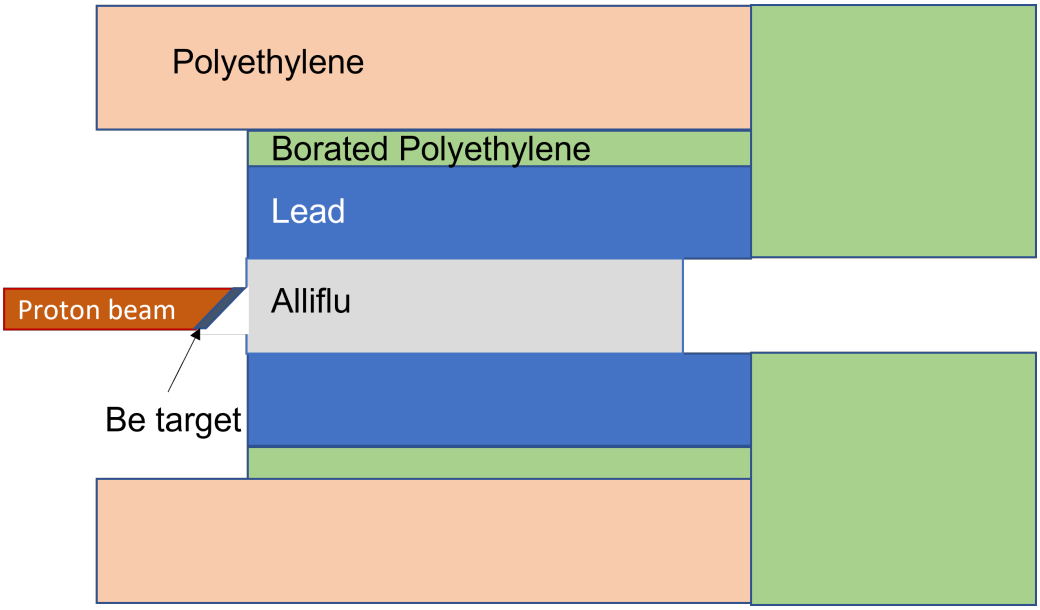

Figure 2.11: Second configuration of the BSA prototype. Not in scale.

extra thickness of absorber made it possible to reach a proton current of 6 μA in some of the measurements. The energy deposition, the neutron an gamma flux in the whole room

were also simulated and the results are reported in the Chapter 3.

The next Chapter describes the spectra measurements performed at LNL with the two versions of the prototype and the simulations reproducing the different set-ups. The second configuration had been constructed in 2022, some weeks before the measurement campaign: Figure 2.12 shows the technical drawings with the explosion of the polyethylene outer shell, while Figure 2.13 shows the second prototype positioned in the irradiation room.

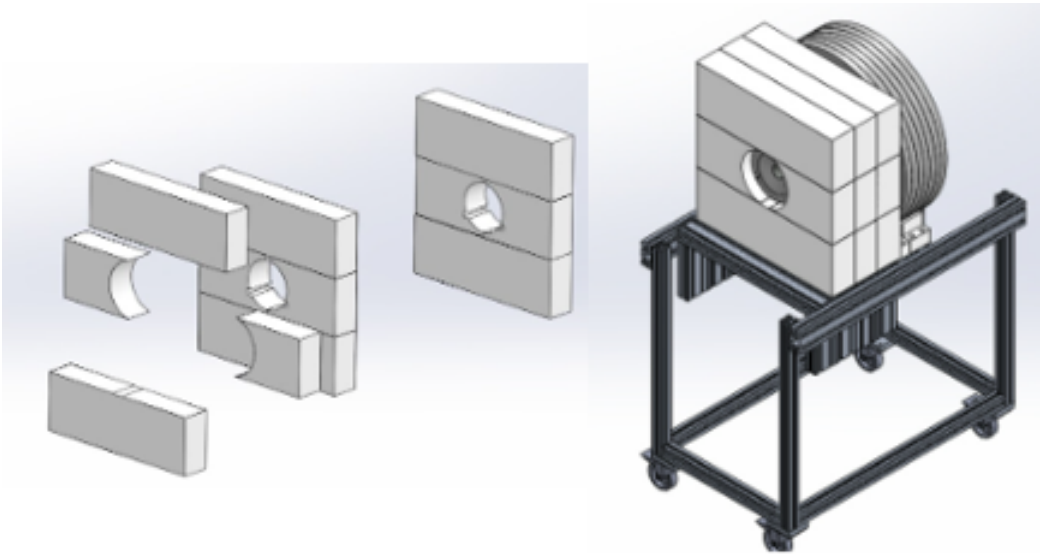

Figure 2.12: Technical drawings of the second version of the BSA.

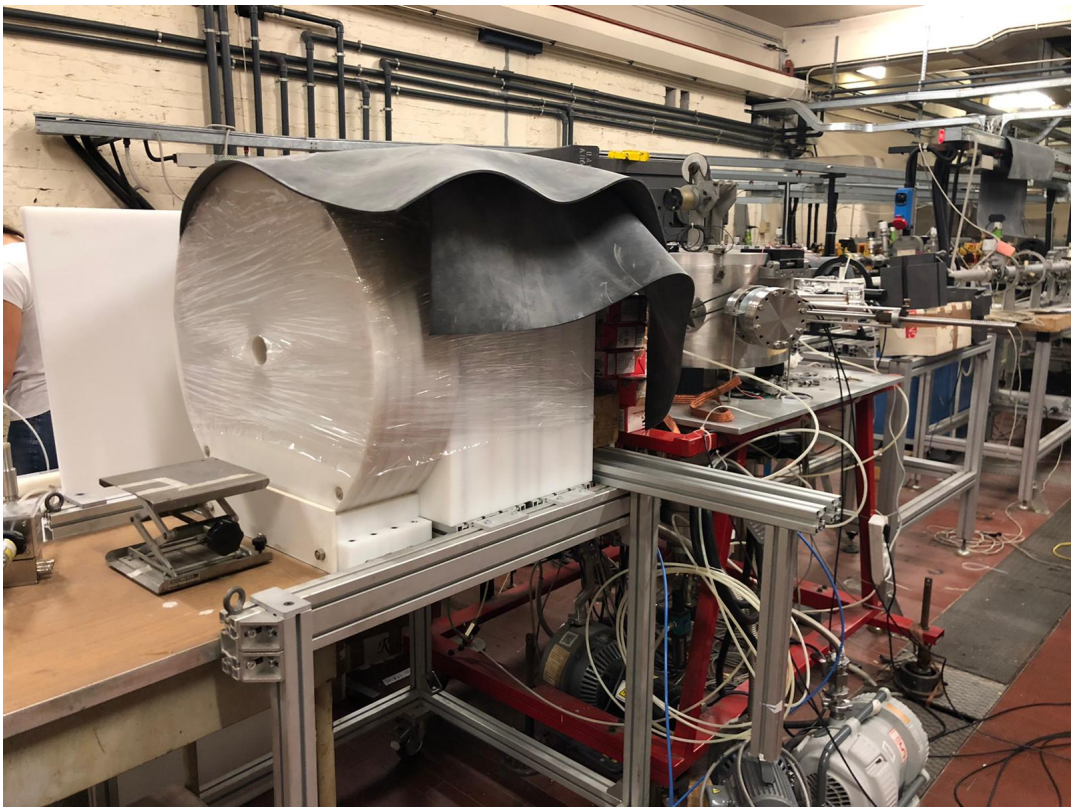

Figure 2.13: Picture of the configuration of the BSA used during ENTER-BNCT measurement shifts (covered by a flexboron sheet)

.

Chapter 3

Neutron spectrometry

3.1 Materials and methods

In the measurement shifts in September 2021 and July 2022, neutron spectroscopy has been carried on using the spectrometer called DIAMON, which was previously employed in this field [31] [30].

DIAMON (Figure 3.1), Direction-aware Isotropic and Active MONitor, is a neutron spectrometer designed and developed by the neutron measurements group of Politecnico di Milano in collaboration with Raylab, an Italian innovative sturt-up which is a spin-off of Politecnico di Milano (https://www.raylab.solutions/).

DIAMON is an all-in-one portable and smart device able to perform neutron spectrometry, to reconstruct neutron direction distributions and to properly derive field and operational quantities in real-time [32]. It is made of a high-density polyethylene (HDPE) polyhedral moderator body that houses a matrix of thermal neutron sensors built on semiconductors. Along the three main axes at different radial positions the sensors are placed, they are a combination of a semiconductor device with a radiator based on ^{6}LiF. The position of the sensors and the geometry of the spectrometer are a result of studies conducted through Monte Carlo simulations.

The signals are recorded and analyzed by a small ultra-low power electronics that allows the device to work stand-alone for an entire day.

A software processes the collected information and creates two datasets called "energy outputs" and "direction outputs", this one is obtained by a weighted sum of counts detected by the sensors along the same axis and the former is the result of a weighted sum of counts recorded by sensors placed at the same radial position. These datasets are provided in real-time and they are used to reproduce the distribution of the field direction and to attain energy outputs, both extracted by an unfolding code called UNCLE. The code calculates quantities related to the field and dosimetric quantities such as H*(10), using the coefficient defined in ICRP 74 [33]. Figure 3.2 shows a screen of the user interface of the software.

During the ENTER-BNCT measurements, different moderator configurations have been tested with the two versions of the BSA. Data were collected on neutron spectrometry due to 14 different arrangements: 7 with a shadow cone between the beam-port and

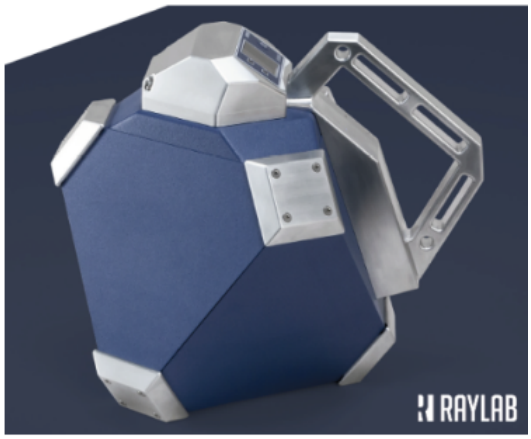

Figure 3.1: DIAMON.

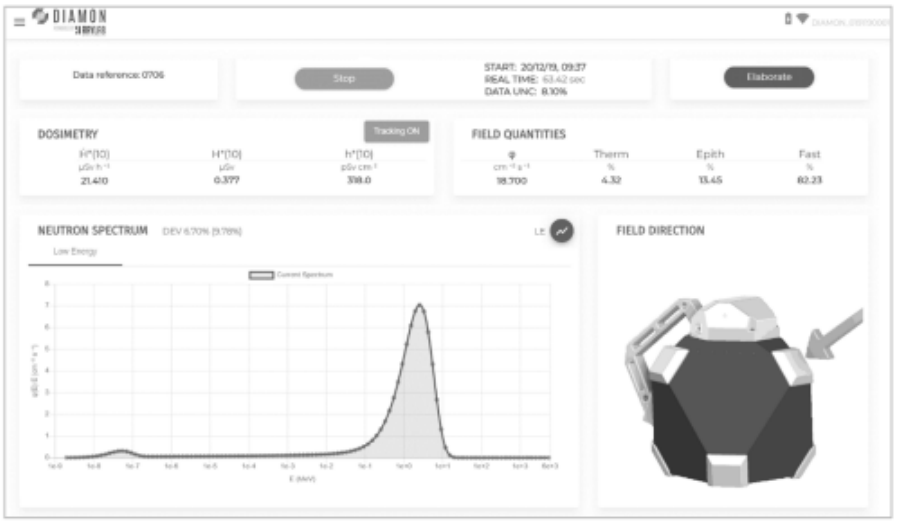

Figure 3.2: Screenshot of the wed interface of the DIAMON.

the spectrometer, and other 7 configurations identical to the previous ones but without the cone. The 7 configurations consist on adding increasing packages of bricks of *Alliflu* for a final total thickness of 26.9 cm. Figure 3.3 shows two bricks.

A total of 27 bricks were available for the measurements, that were assembled into 7 packages as described in Table 3.1.

The shadow cone is 50 cm long, made of iron and polyethylene and constructed according ISO specification. The measurements with the cone are performed to estimate the contribution of the scattered field that is subtracted from the total field, obtained without cone. It is thus possible to determine the response of the device to the direct field, through the subtraction of the scattered component. DIAMON, in all the configurations, in placed 1 m away from the beam port.
Figure 3.4 shows the placement of the elements.

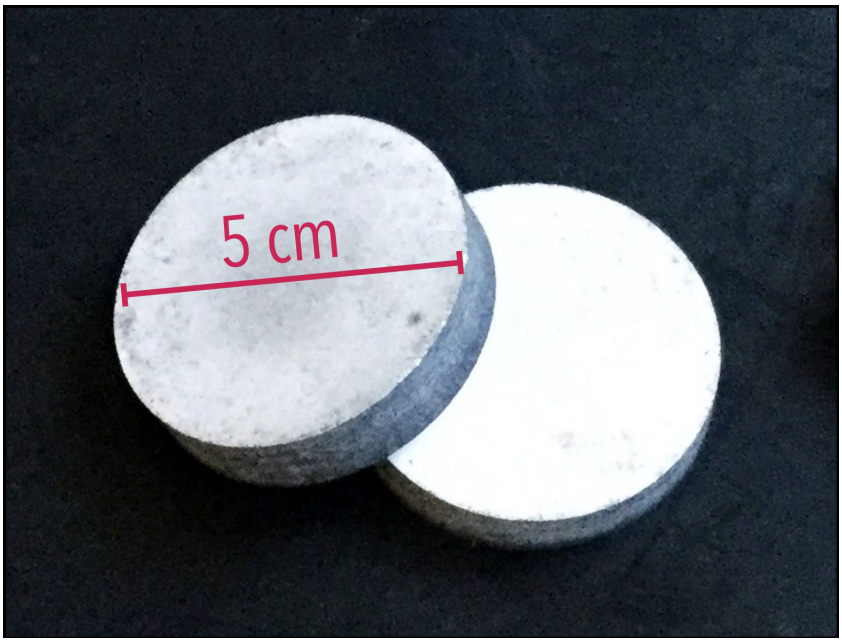

Figure 3.3: Picture of two *Alliflu* bricks.

Name	**density [g/cm^3]**	**thickness [cm]**	**description**
N1N2N3	2.27	3.3	without Li
N4N5A	2.33	3.2	without Li
BCDE	2.35	4.3	with Li
FGHI	2.30	4.3	with Li
LMNO	2.34	4.2	with Li
PQRL3L4	2.48	3.7	with Li
L8L9L10L11	2.55	3.9	with Li

Table 3.1: Characteristics of the *Alliflu* bricks list in the exact order (from top to bottom) used in the measurements (from the position closest to the target towards the beam port).

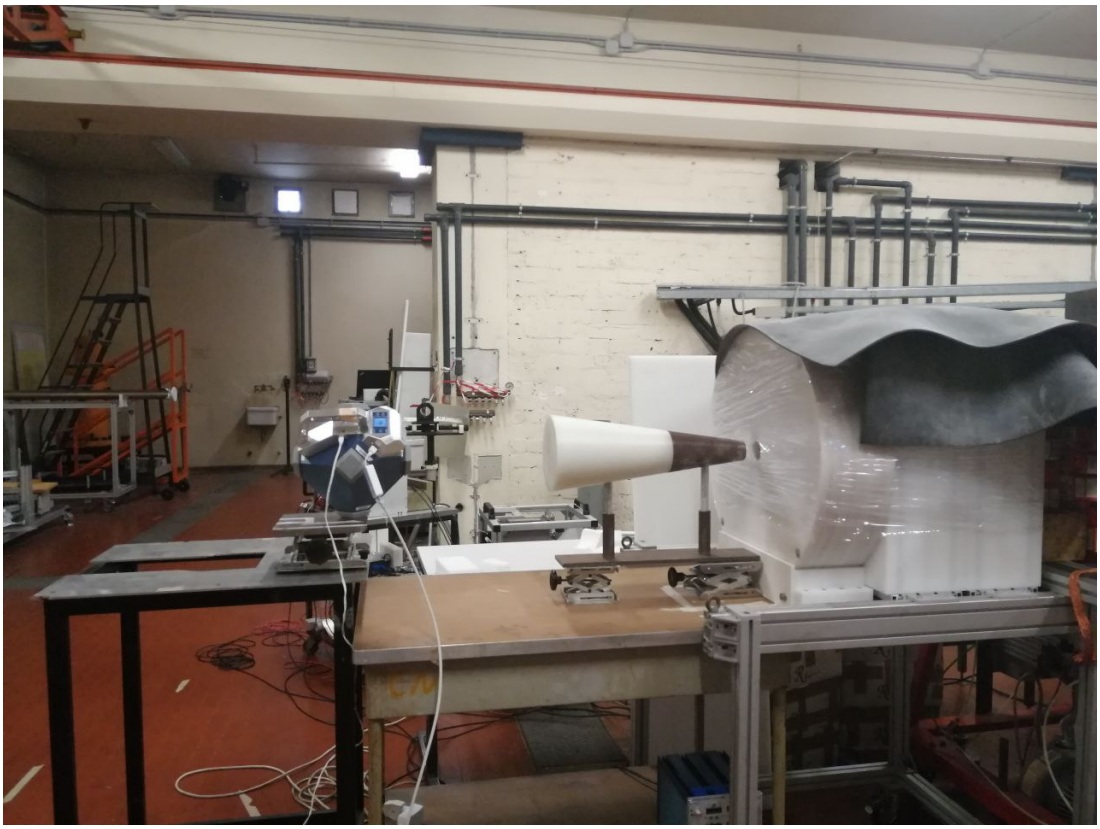

Figure 3.4: Picture of the configuration with the shadow cone and the DIAMON put in place. From left to right: DIAMON detector, shadow cone, BSA collimator, BSA body (covered with a flexi-boron sheet).

3.2 Monte Carlo Simulations

MCNP is a Monte Carlo radiation-transport code designed to track many particle types over broad ranges of energies. [34].

MCNP has been released for the first time in the mid-1970s by Los Alamos National Laboratory and has been enhanced over the years. MCNP can be used in many transport modalities, for example neutron or photons only or combined neutron/electron/photon, neutron/photon or photon/electrons; but the code can simulate the transport of others charged particles. The code can be used for several applications such as nuclear reactor design, radiation protection, medical physics, radiation protection, nuclear criticality safety and many other fields.
The user writes an input file which gives to the code the information for calculation. The input file must have a specific structure and includes the following items in the order reported:

1. the geometry;
2. the materials (which select the nuclear data to be used for the transport);

3. the radiation source;

4. the tally (i.e. the quantity to be calculated).

The *geometry* is the 3D space within which the particles have to be transported. It is defined through surfaces and cells, the latter characterized by the material and its density and they are outlined using the Boolean geometry starting from the surfaces.
The *tally* are the quantities to be calculated in a specific volume or surface inside the geometry defined by the user.

The transport code allows the employ of different types of variance reduction techniques that improve the effectiveness of the calculation, i.e., reaching a reliable result affected by a low relative error in short calculation times. One of MCNP characteristics is a deep analysis of the significance of the tally result, performed through the calculation of 10 statistical tests to ensure that variance reduction did not affect the robustness of the calculation.

The simulation reported in this thesis are all performed with the MCNP6 code, in its version 6.2.

3.2.1 Geometry of the experimental set-up

The geometry simulated (Figure 3.5) consists in a room 335x324.5x300 cm^3 with a concrete floor thick 50 cm and a corridor 55 cm large placed behind an iron door 5 cm thick. Beyond the corridor there is a 50 cm thick concrete wall. The BSA is placed on the surface opposite the door. The body of the accelerator is not represented, as the radiation source is defined in the target as explained below. The composition of the two BSA prototypes are reported in Section 2.4. The 7 packages of *Alliflu* bricks are simulated with the same dimension, composition, density and order reported in Table 3.1.
A Bakelite table is placed in front of the BSA simulating the supports for the instrumentation present in the irradiation room.
Figure 3.6 shows the simulation of the first version of the BSA with (left) and without (right) shadow cone. The purple structure is the borated polyethylene collimator, the *Alliflu* elements are depicted in green (without lithium) and yellow (lithiated). The lead reflector is the red cylinder housing the moderator bricks. Figure 3.7, shows the second version of the BSA, again with (left) and without (right) shadow cone, with the same color code as before. The orange structure is the polyethylene shell added for the second measurement campaign.

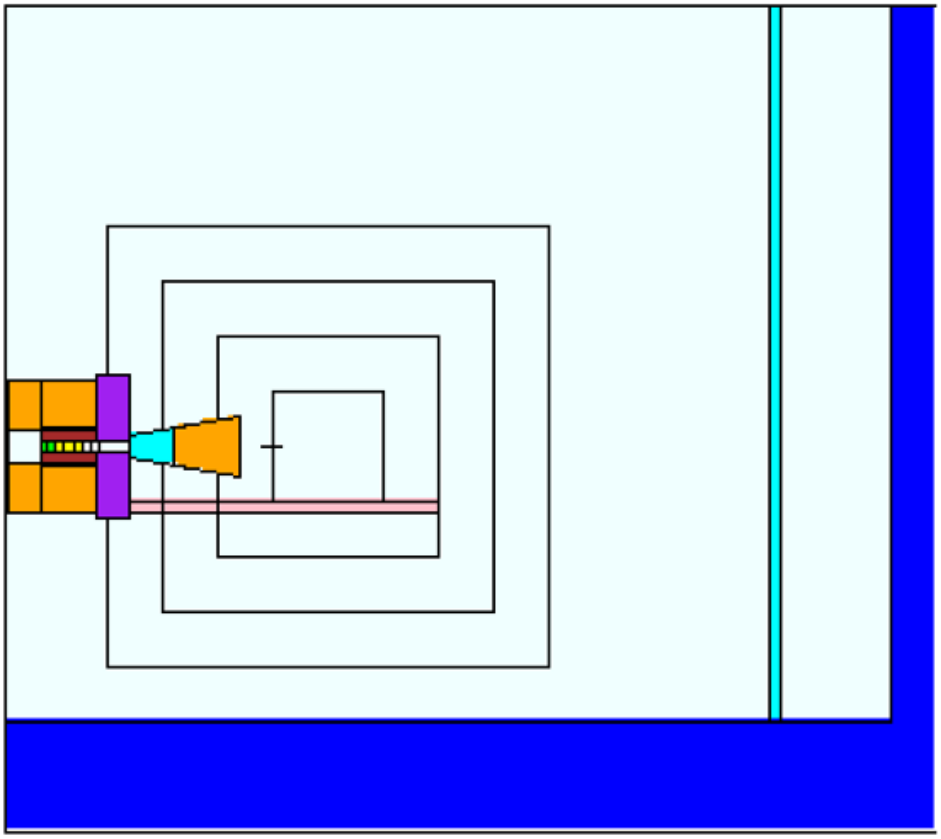

Figure 3.5: Complete geometry simulated of the room (second configuration); the neutron spectrometer DIAMOND is placed in correspondence of the sign "+".

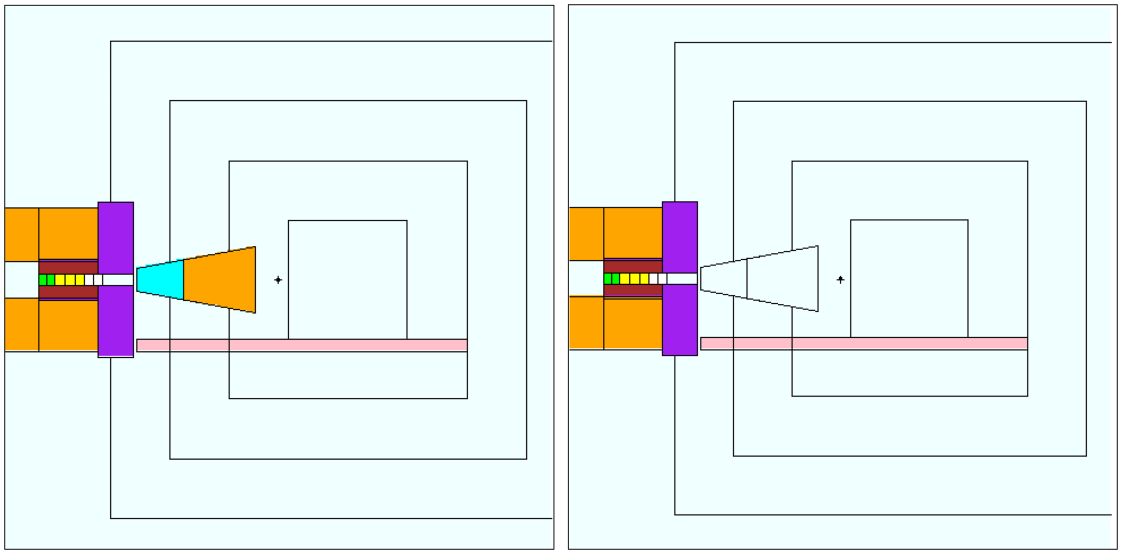

Figure 3.7: Simulated geometry of the room with the second prototype of the BSA, left: configuration with the shadow cone right: simulation without the cone.

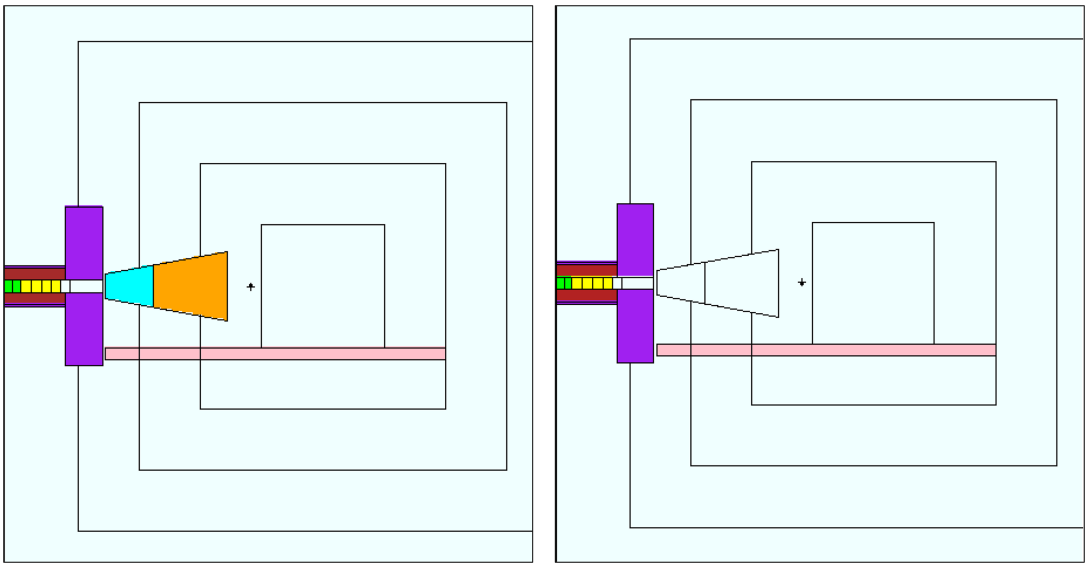

Figure 3.6: Simulated geometry of the room with the first prototype of the BSA, left:configuration with the shadow cone right: simulation without the cone.

3.2.2 Source of neutrons

To model the neutron source, the specification of the double-differential spectra emerging from (p,n) reaction in Be at 5 MeV has been used. This source had been implemented in a previous PhD thesis [35] and validated thoroughly. The same source was used to design the BSA prototype in [29]. The cross section of neutron production in Be are not adequate in MCNP. Moreover, starting from a proton source, the efficiency of the calculation would be very low. Thus, experimental results of neutron spectra as a function of energy and for different angles with respect to the proton beam were used to define the source. These spectra had been measured in the same CN facility, as described in [36]. The source has been approximated as point-wise. Figure 3.8 shows the neutron flux energy distribution for different laboratory angles.

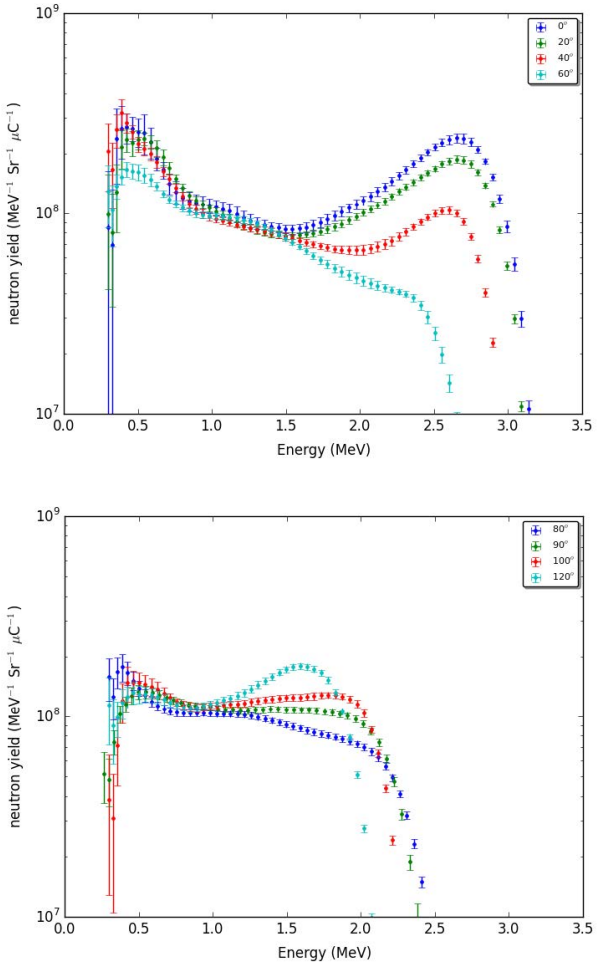

Figure 3.8: Double differential spectra of neutrons emerging from the Be(p,n) reaction at 5 MeV, as measured by Agosteo et al., and used to simulate the emission of neutrons from the target.

3.2.3 Tally and Variance Reduction

The detector has been simulated as a 1 cm^3 air volume located in the same position as DIAMON. The neutron flux (tally type F4) has been defined in the volume with an energy binning from 0 to 4 MeV. The tally results obtained in the configuration with the shadow cone were subtracted to those obtained with the shadow cone for the first configuration (see below). The results of the simulations are per unit of source neutron.
The tally in the first configuration of the BSA has been placed where the sign "+" is drown; in the second configuration, a tally is placed near the beam port where the microdosimeter has been placed during the measurements (see Section 4.4.3).
Given the amount of materials, the distance between the source and the detector, and the small tally volume, the simulations suffer from a very low efficiency. This means that

it is necessary a very long computation time to reach a reliable statistics in the tally, i.e. a relative error lower than 10% in all the energy bins. For this reason, variance reduction was an important part of the simulation. MCNP allows the implementation of the so-called weight-windows [34]. First, the simulation is run setting a value of importance for each cell. The importance causes the particles to split when they cross a surface towards a cell of higher importance. The statistics thus improves because the number of particles reaching the detector increases. To avoid a bias, a weight is associated to each particle in the run: when it splits, the weight decreases accordingly and the tally is calculated by weighted average of the contributions. On the other hand, when crossing a surface towards lower importance, particles are killed with a certain probability and those which survive gain a higher weight. In the limit of a high number of simulated particles, the overall weight is conserved and the tally is not biased. This helps to reach proper results in shorter times, however, over-splitting may occur. Weight Windows (WW) are a more refined technique, consisting in weight limits set for each cell. The weight of the crossing particles are checked against these minimum and maximum thresholds and particles are forced to split if too heavy, or they are killed if too light. This avoids proliferation of very low-weighted particles and large tally fluctuations due to the contribution of heavy particles. To define the WW, the instruction WWG (Weight Windows Generator) is turned on and MCNP optimizes the values for each cells according to the tally to be calculated. The map of WW can then be used to re-iterate the calculation with the generator on to obtain a further optimization. This calculation of WW is performed in the worst case, i.e. the BSA completely filled with the moderator and the shadow cone present. This is in fact the situation where a lower number of particles reaches the detector. Then, the next calculations are made by replacing the shadow cone and the packages of bricks with air but maintaining the same WW values. This strategy allowed reducing significantly the calculation time and obtaining statistical reliable tally results. The concentric cubes visible in the air of the room in Figures 3.5, 3.6 and 3.7 are a fictitious cell separation created to increase the importance (and to optimize WW) in the region of the detector.

3.2.4 Results and discussion

First configuration

Figures 3.9 shows the simulated spectra obtained using the first configuration of the BSA filled with increasing thickness of neutron moderator.

As expected, the integral flux decreases as the the thickness of the *Alliflu* increases. Moreover, increasing the thickness of the moderator, the fast component of the spectrum decreases, with a relative gain in the region around 100 keV, at least for thickness values up to 15 cm. The moderator performs as expected in reducing the fast component without loosing too much epithermal flux (central region of the spectra). As mentioned before, generating a peak around 10 keV is not a possibility with this prototype which is aimed at modifying the spectra for simulation-measurement validations.

Experimental spectra were obtained with UNCLE unfolding method, using no *a-priori*

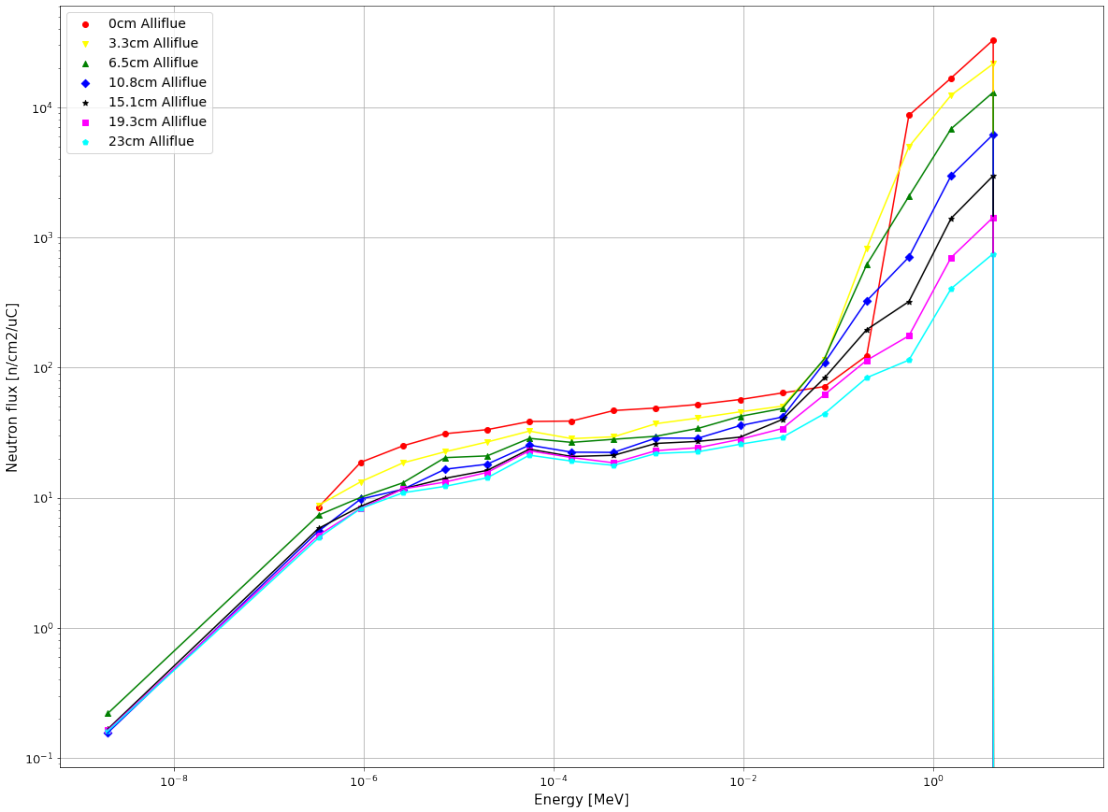

Figure 3.9: Comparison of the neutron spectra of the first configuration of BSA with increasing *Alliflu* thickness obtained with the simulations.

knowledge. For this reason, although the experimental spectra point out a prevalence of flux in the fast energy region and a general behaviour coherent to what expected, the spectra are not yet optimized for a proper validation. In fact, due to the unfolding algorithms the spectra extend to 10 MeV, which is not physical. As an example, Figure 3.10 reports the comparison with no moderator inserted.

For reference, Figure 3.11 reports the experimental spectra obtained wih the UNCLE method.

Despite the unfolding method used for experimental data is not optimized yet, DIAMON has the ability to measure the integral fluence with great precision. This value can be used for a validation of the simulations concerning the integral flux, as reported in Figure 3.12, where the attenuation, both simulated (red) and experimental (blue), as a function of the thickness of *Alliflu* is represented. The Figure 3.12 shows a very good agreement between the experimental and simulated data.

Second configuration

Figure 3.13 and Figure 3.14 show the spectra simulated with the BSA modified with the polyethylene shell, they represent the spectra of the tally in the position of the DIAMON

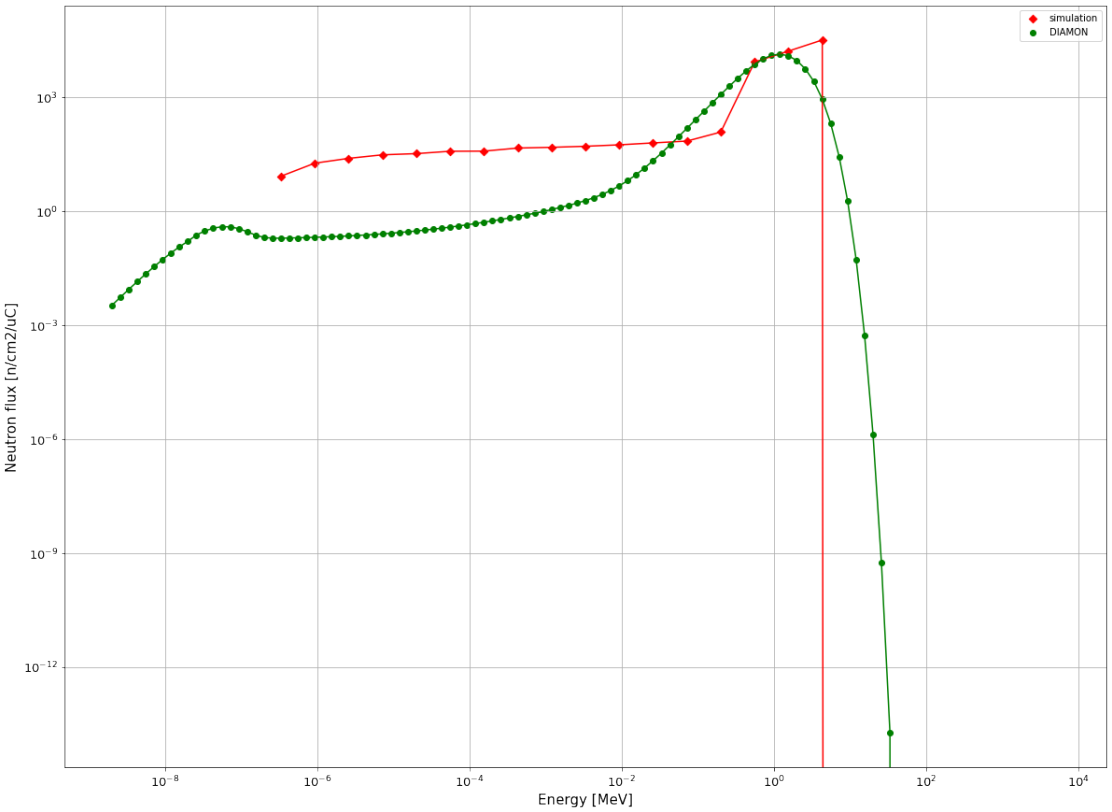

Figure 3.10: Comparison of the simulated and experimental spectra for the first prototype of the BSA with no moderator inserted.

and the microdosimeter respectively.

The spectra show that the neutron flux decreases increasing the bricks of *Alliflu* for both the tallies as expected. At the time of the writing of this thesis the experimental results of this run of measurements are still under analysis and cannot be reported here. However, a new analysis based on an educated unfolding, introducing some constraints (i.e. the maximum neutron energy at 3.2 MeV) and the *a-priori* knowledge of the spectra given by the simulations presented is underway.

The simulated results on spectrometry allow a comparison of the two BSA configurations. The first points out a significant modification of the spectrum in the fast region, showing the ability of *Alliflu* to suppress this component which delivers unwanted dose to the patient without affecting much the epithermal part of the spectrum. This confirms the potential of this material as the central core of a clinical BSA to design a beam useful for patient treatments with good efficiency, i.e. without loosing flux. It is in fact important to have a neutron flux of at least 10^{10} cm^{-2} s^{-1} with as low as possible contributions in the thermal and fast regions.

The second configuration, which adds a significant moderator around the reflector, evidences a deeper modification of the beam, also in the epithermal part, where we lose a factor 2 for 6 moderator elements included, with a even deeper suppression of the fast

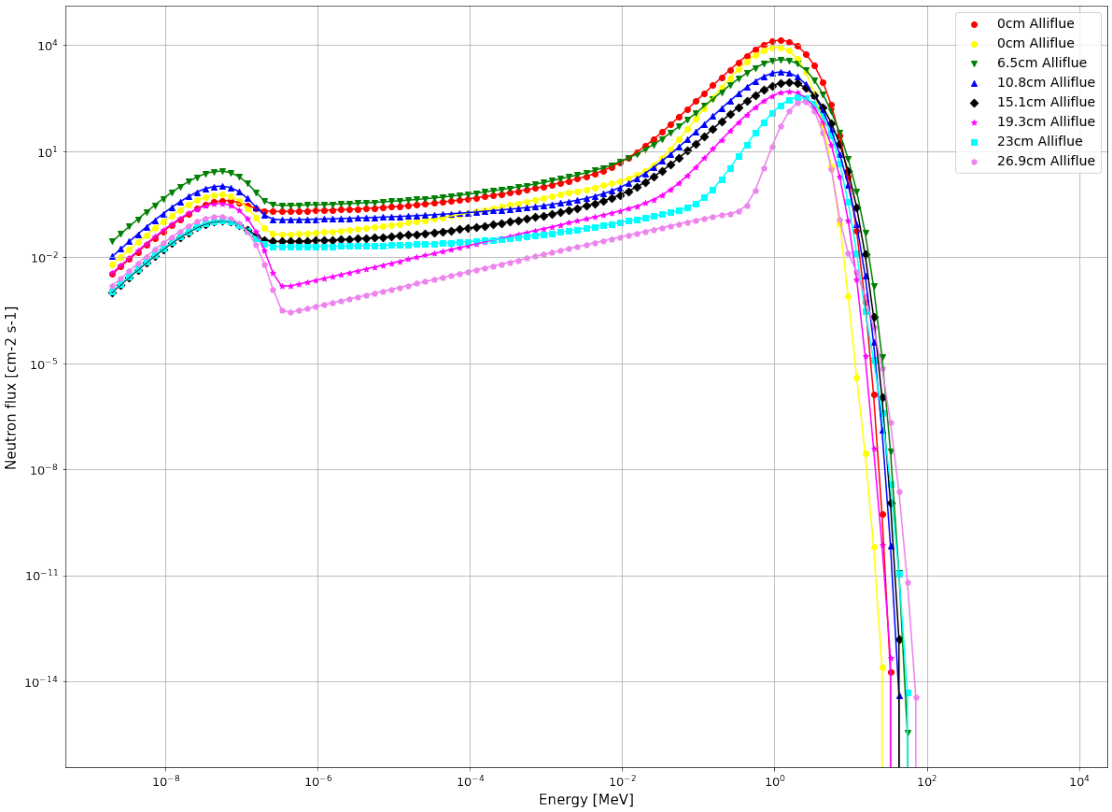

Figure 3.11: Comparison of the neutron spectra of the first configuration of BSA acquired by the detector DIAMON.

component. In Figure 3.15 and 3.16 the spectra of the two configurations of the BSA, with 0 and 6 bricks of *Alliflu*, are compared.

The possibility to work with two configurations of the BSA (where the thickness of moderator can be modulated) is very important because the quantity of spectra to be acquired and simulated is high, enabling a detailed validations. This will ensure the correctness of the in-patient dosimetry calculated with the designed beam of the clinical facility.

As mentioned before, the polyethylene shell lowered the ambient dose and allowed working with higher proton current.

Figures 3.17 e 3.18 show the energy deposition distribution in the room obtained by a *Tmesh tally*, i.e. a tally superimposed on the geometry for the second version of the BSA and for the first, respectively. Simulations were carried out using tally type 3 which scores energy deposition per unit volume from all particles included in the transport, in this case, neutron and photons. Dose cannot be scored with mesh-tally type because the elements of the mesh are superimposed to the geometry and the mass of the encompassed objects cannot be calculated by MCNP. However, this distribution is an indicator of the dose distribution in the space. Even if the color-scale is not the same, these Figures show how the polyethylene shell helped in decreasing the ambient dose. The experiments

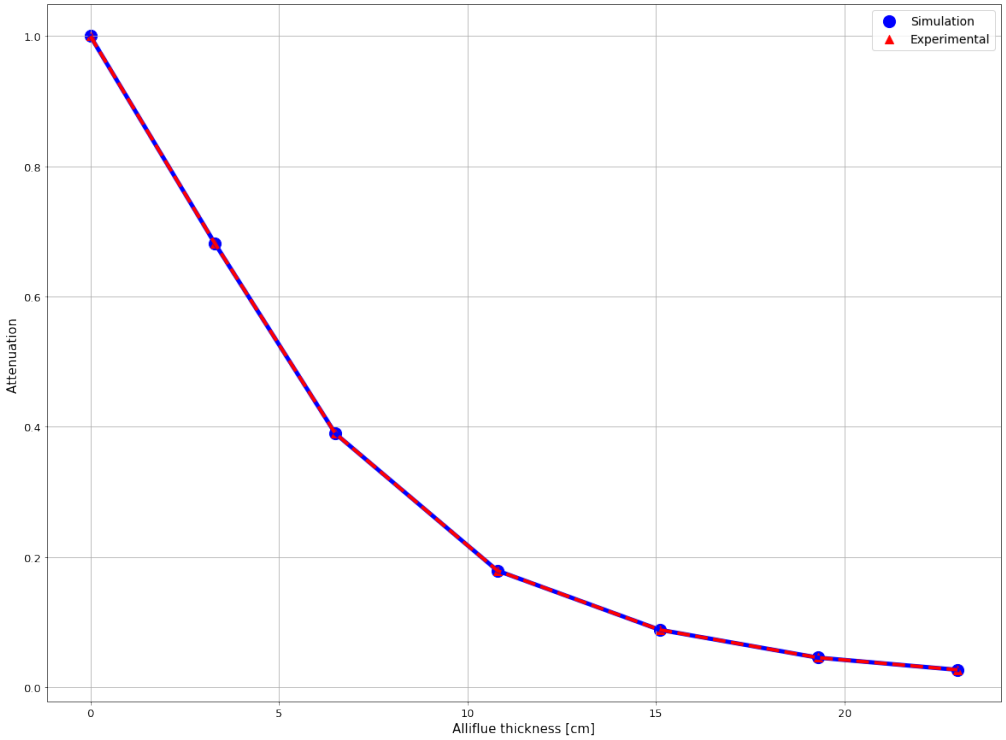

Figure 3.12: Comparison of the attenuation due to increasing thickness between the experimental data (red) and the simulation (blue): the errors of the experimental data are about 5%, the errors of the simulated data are about 1%.

where carried out with additional shields (flex boron shields and borated water elements) as shown before.

To visualize the effect of the shell and its influence on the ambient dosimetry Figures 3.19 and 3.20 show the neutron flux obtained with the Tmesh tally type 1 for the second and the first configuration respectively.

Finally, Figures 3.21 and 3.22 show the photon flux obtained with the Tmesh tally type 1 for the second and the first configuration respectively. Again, color scale is not the same.

For gamma radiation, it can be seen a higher flux in the BSA region, due to the presence of hydrogenated material (polyethylene) and the consequent production of 2.2 MeV photons. However, this increase is more than balanced by the reduced flux of neutrons, shielded by the shell itself.

In this measurement campaign, the innovative aspect respect to the previous campaigns has been the studies of the spectra in the field of microdosimetry, described in the next Chapter.

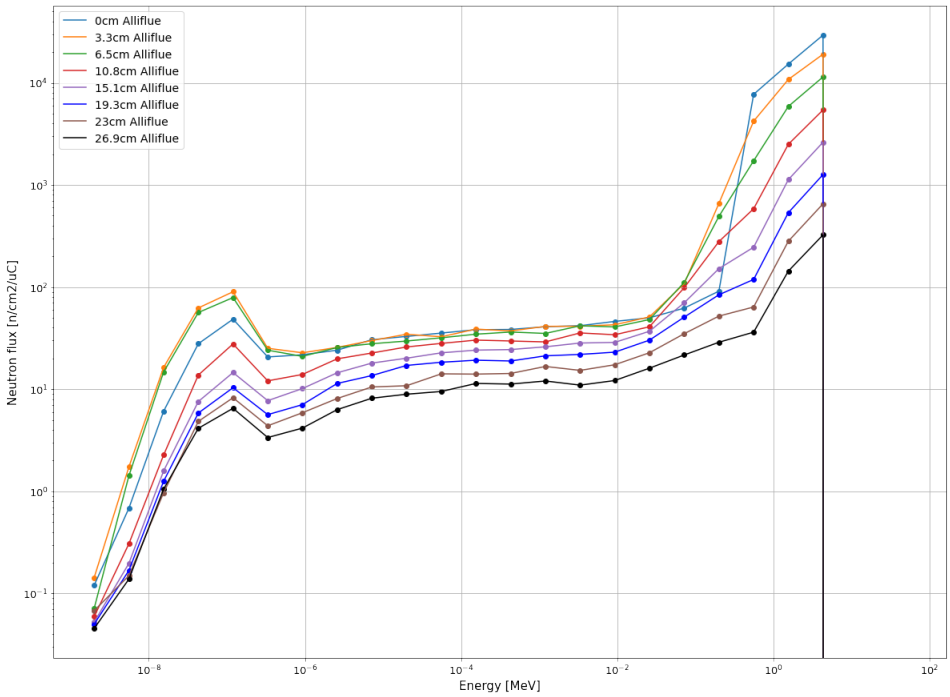

Figure 3.13: Spectra of the second configuration of BSA with increasing thickness of *Alliflu*, tally placed in the position of the DIAMON.

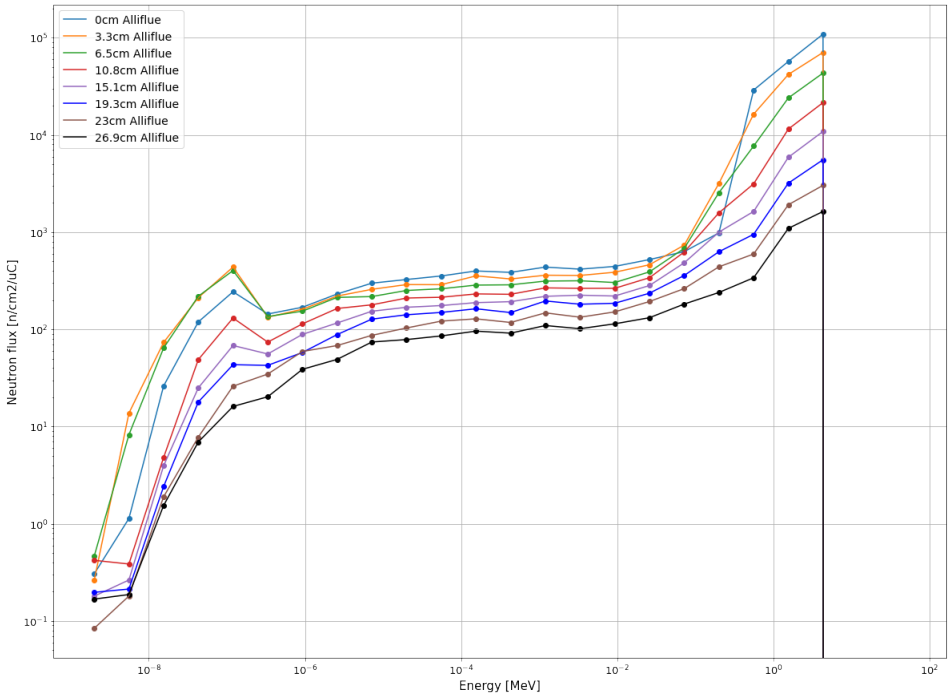

Figure 3.14: Spectra of the second configuration of BSA with increasing thickness of *Alliflu*, tally placed in the position of the microdosimeter.

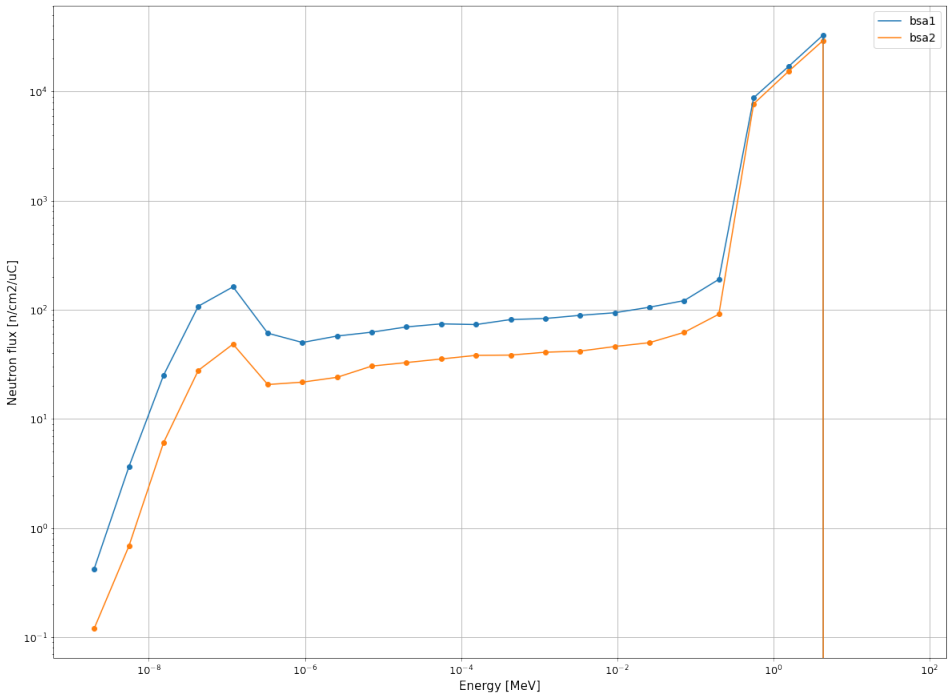

Figure 3.15: Comparison of the spectra obtained without moderator in the two prototypes of BSA.

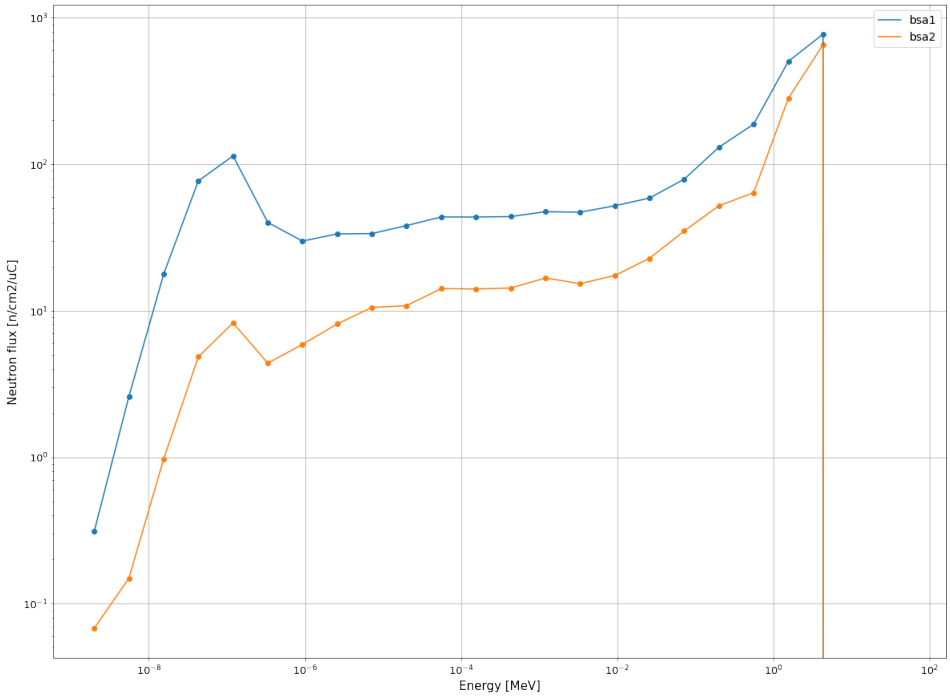

Figure 3.16: Comparison of the spectra obtained with 6 bricks of moderator in the two prototypes of BSA.

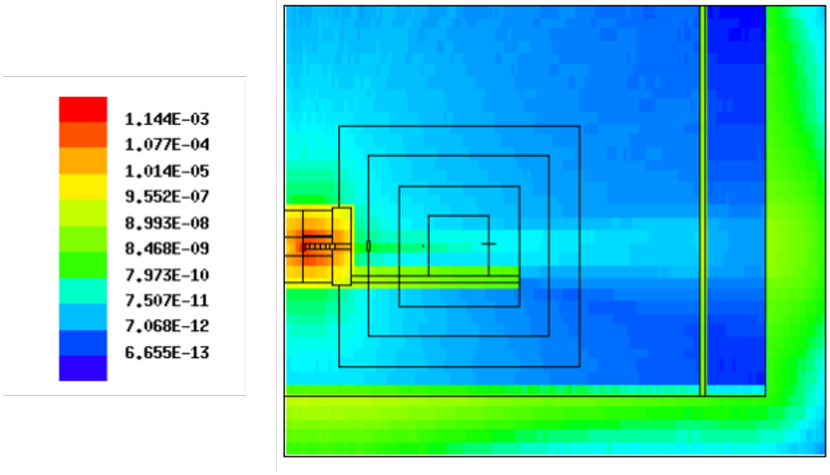

Figure 3.17: Energy deposition per unit volume in the room for the second version of the BSA. Units are per neutron emitted from the source.

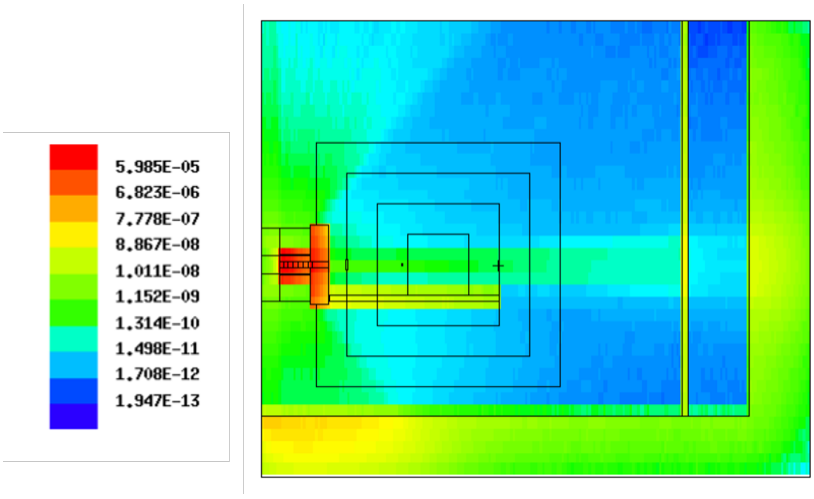

Figure 3.18: Energy deposition per unit volume in the room for the first version of the BSA. Units are per neutron emitted from the source.

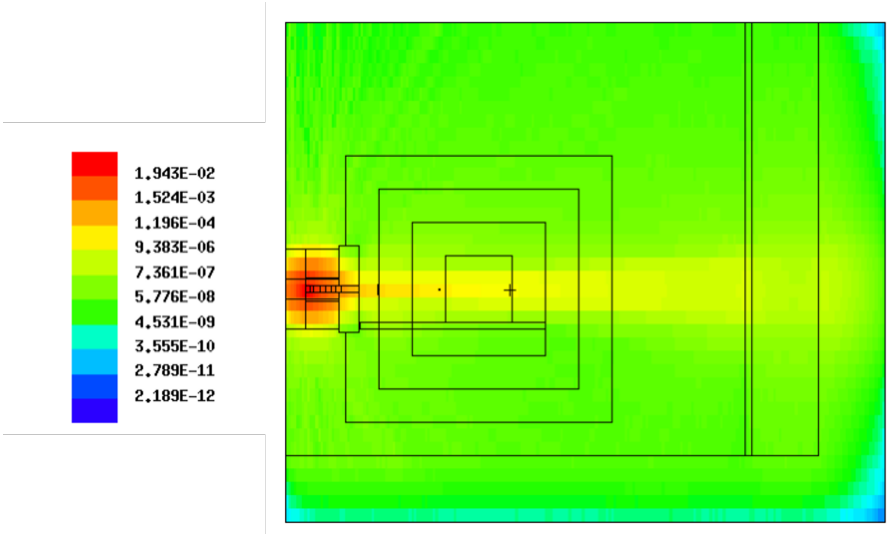

Figure 3.19: Neutron fluence in the room for the second version of the BSA. Units are per neutron emitted from the source.

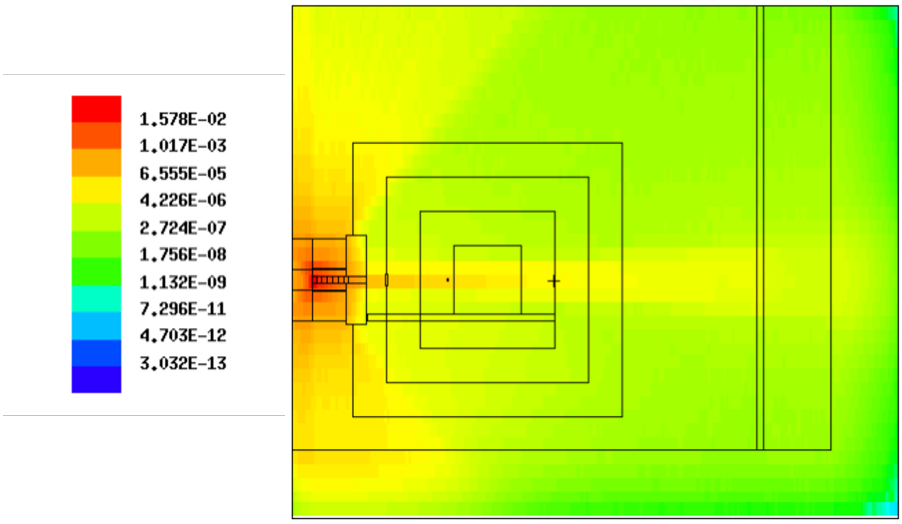

Figure 3.20: Neutron fluence in the room for the first version of the BSA. Units are per neutron emitted from the source.

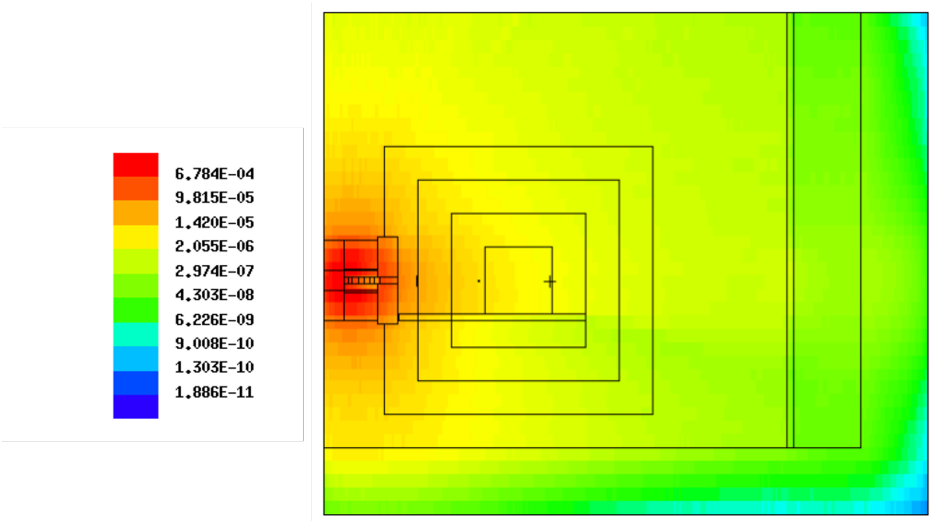

Figure 3.21: Photon fluence in the room for the second version of the BSA. Units are per neutron emitted from the source.

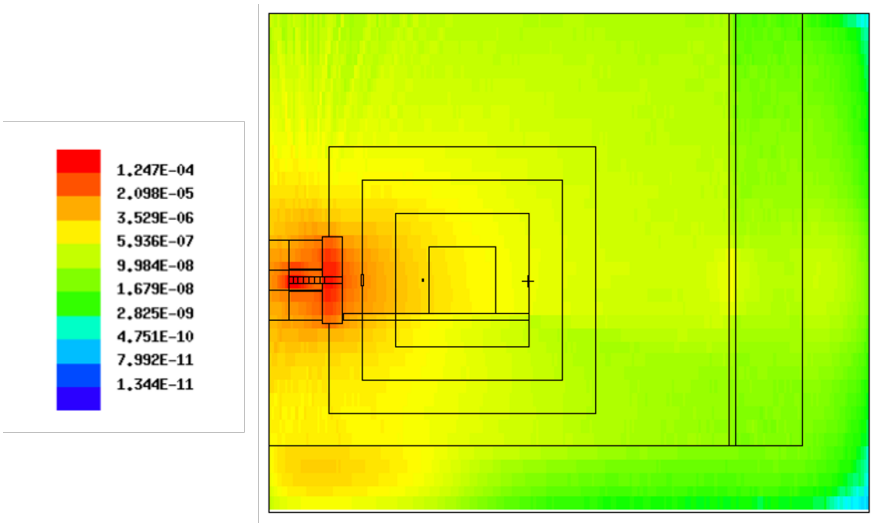

Figure 3.22: Photon fluence in the room for the first version of the BSA. Units are per neutron emitted from the source.

Chapter 4

Microdosimetry

In this chapter theoretical and experimental microdosimetry will be described. In the first section the main quantities used in microdosimetry are defined, then, the following section will give an overview of the most used microdosimetric detectors, in particular the Tissue-Equivalent Proportional Counter (TEPC) used in this work.

Microdosimetry, which was developed as a system of concepts as well as of physical quantities and their measurement, is the systematic study and quantification of the spatial and temporal distribution of absorbed energy in irradiated matter. [37].

Microdosimetry was introduced for the first time in the 1950s by H.H. Rossi in order to overcome the use of average quantities to describe stochastic phenomena such as the interaction of ionizing radiation with matter; the spectrum distribution of energy deposited by a single primary event that crosses a micrometric volume can be recorded by microdosimetry.
When charged particles interact with matter, they loose energy along their track and this quantity is usually calculated through the energy loss per unit of path length, called Stopping Power S(E) and described by the Bethe-Bloch formula. It might happen that the kinetic energy loss during the interaction is not completely absorbed in the target volume due to the production of δ-rays, secondary electrons, which can have high energy so that their ranges are longer than the dimension of the volume and they thus escape. When this occurs in a small volume, the Stopping Power overestimates the dose delivered to the volume if this phenomenon is not taken into account. For this reason, in 1952, Zirkle introduced the Linear Energy Transfer (LET) to highlight the fact that, in dosimetry, the energy absorbed by the medium is more important than the energy lost by the primary particles. The restricted LET (LET_Δ) has been also defined: it is the mean energy loss per unit of path length with the kinetics energy of the secondary electrons smaller than Δ which means that in the restricted LET only the secondary electrons with energy smaller than Δ are considered, in order to exclude the electrons that deposit energy far from the track. This quantity has been introduced to consider the energy deposition in proximity of the track, being the one that mostly influences the biological effect. LET is a non stochastic quantity which cannot describe the pattern of the energy deposition at a micrometer level; in these cases, quantities that describe the stochastic nature of the interaction between radiation and matter are necessary. For these

reasons, Rossi introduced microdosimetry.

4.1 Theoretical Microdosimetry

4.1.1 Microdosimetric quantities

Energy deposit, ϵ_i, is the principal quantity of microdosimetry and it is the energy deposited in a single interaction i:

$$\epsilon_i = \epsilon_{in} - \epsilon_{out} + Q \tag{4.1}$$

where ϵ_{in} is the initial energy of the ionizing particle which interact with the matter without considering the rest energy, ϵ_{out} is the sum of the energies of the products of the interaction without the rest energy and Q is the change in the rest energy of the nucleus and particles involved in the reaction.
The sum of all the energy deposits ϵ_i in a given volume of matter is called *energy imparted*:

$$\epsilon = \sum_i \epsilon_i \tag{4.2}$$

Both *energy deposit* and *energy imparted* are most often expressed in terms of eV.

The *specific energy imparted*, z, is the ratio of ϵ and the mass m of the volume taken into account, thus

$$z = \frac{\epsilon}{m} \tag{4.3}$$

J kg^{-}1 is the unit but in the case of z, the unit is called Gray (Gy).

The *lineal energy*, y, is the quotient of the energy imparted to a given volume in matter by a single primary particle and all the secondaries it generates ϵ_s and the mean chord length of the volume $\bar{l}$:

$$y = \frac{\epsilon_s}{\bar{l}} \tag{4.4}$$

The Unit is J m^{-1} but the numerator may be expressed in eV or its multiples and the denominator in multiplies of m, so that the most used unit is keV μm^{-1}. The *specific energy imparted* z and the *lineal energy* y can be considered the analogous of the dose and the LET respectively but with the difference that they are defined for a finite volume which may not even be crossed by the track of the primary particle.

The stochastic nature of ϵ makes it necessary to use probability distributions. f(y) is the probability density so that f(y)dy is the probability of having an event characterized by *lineal energy* y included between y and y+dy; d(y) is the probability density that, weighted by y, represents the fraction of dose delivered with *lineal energy* y in the interval (y, y+dy). Both, f(y) and d(y), do not include events with y=0.

There are two more quantities which are useful: the frequency-mean lineal energy $\overline{y}_F$ and the dose-mean lineal energy $\overline{y}_D$:

$$\overline{y}_F = \int_0^{+\infty} yf(y)dy \tag{4.5}$$

$$\overline{y}_D = \int_0^{+\infty} yd(y)dy = \frac{1}{\overline{y}_F}\int_0^{+\infty} yf^2(y)dy \tag{4.6}$$

In the same way, f(z), d(z) and average quantities $\overline{z}_F$, $\overline{z}_D$ are defined.

4.1.2 Representation of microdosimetric distribution

A microdosimeter can detect a great variety of particle types (e.g. photons, neutrons, charged ions...) and for this reason a microdosimetric spectrum must be able to represent a wide range of imparted energies and cover multiple orders of magnitude. Therefore, the lineal energy axis is usually divided into equal logarithmic intervals. The dose or frequency distribution are instead plotted on a linear axis, after being multiplied by y so that the area under the curve is not distorted by the logatithmic representation. In the *f(y)* vs *y* and *yf(y)* vs *log(y)* representations of the spectrum, the area under the curve between two values of lineal energy indicates the fraction of events characterized by lineal energy in the range considered; similarly in the *d(y)* vs *y* and *yd(y)* vs *log(y)* dose distribution spectrum equal areas represent equal fractions of dose delivered by events with y in the range take into account. The advantage of the representation with the logarithmic axes lies in the fact the the fraction of events or the dose delivered by events with the y in a specific range, can be extract directly from the spectra.

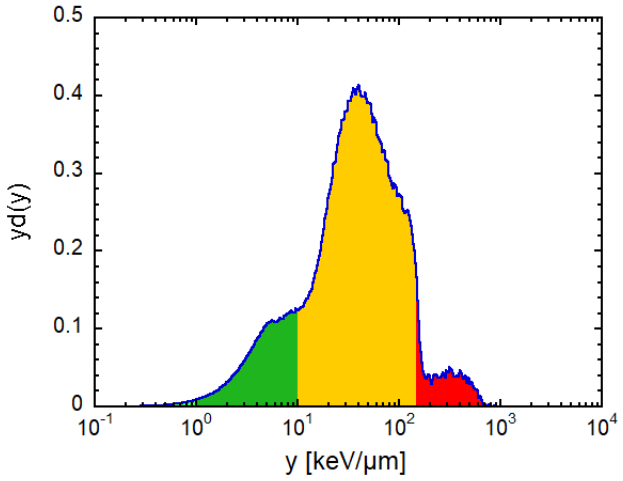

Figure 4.1: Example of a generic single-event spectrum: it is a spectrum of fast neutron produced in the reaction D(5.5 MeV)+Li during an experiment carried on at the CN accelerator of LNL and it is acquired with a TEPC.

4.2 Experimental Microdosimetry

The purpose of microdosimetry is measuring quantity related to the energy imparted ϵ. The most used devices in the field of experimental microdosimetry are the Tissue-Equivalent Proportional Counters (TEPCs) but there are other types of detectors that can be used in such measurements. The idea that a particle passing through the macroscopic sensitive volume of a gas counter deposits the same amount of energy that the same particle would do passing through a tissue volume is the foundation of the simulation of a microscopic site. The density of the gas cavity must be lowered appropriately to reach this equality. And, in addition to this, the elemental composition of the device must be similar to the tissue. The other types of detectors used in this field are the solid state detector, their use has been spread out in the last years even though their potential was recognised back in the 1980s. The solid state largely studied in the last years are especially silicon ([38], [39] and [40]) e diamond based microdosimeters ([41] and [42]).

In this Section the most used microdosimetes, Tissue-Equivalent Proportional Counters, will be described, with the focus on the device developed at Laboratori Nazionali di Legnaro of INFN by the team of Valeria Conte. Furthermore, the main characteristics a microdosimeter should have will be discussed.

4.2.1 Gas detectors: the Tissue Equivalent Proportional Counters

Tissue-Equivalent Proportional Counters (TEPCs) are gas detectors filled with tissue equivalent gases and constructed with tissue equivalent materials. They work in pulse mode, collecting signal pulses from each ionising particle interacting in the sensitive volume and the output given is proportional to the number of ionisations of each event.

The first TEPC, portrayed in Figure 4.2, was designed and built by Rossi when he developed the theory of microdosimetry; since then, TEPCs have been the most used microdosimeters and they have been improved during the years.

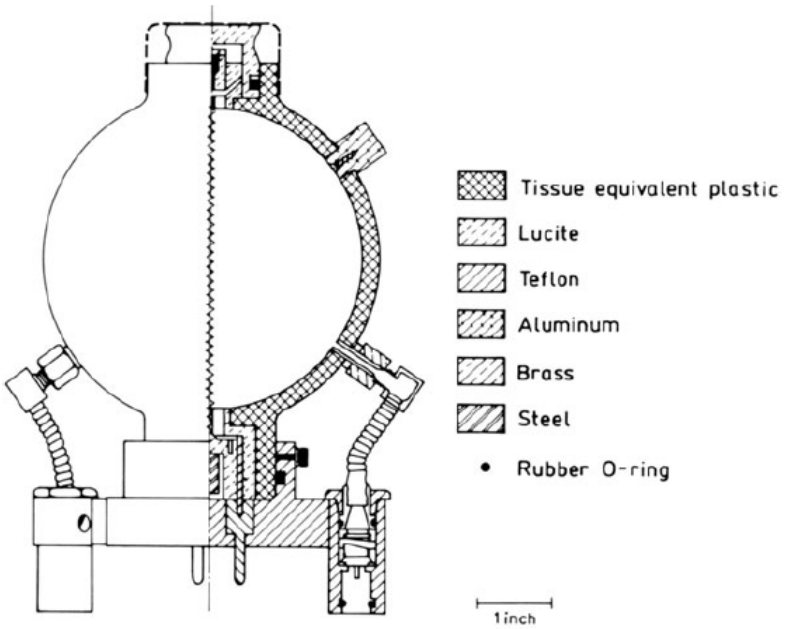

Figure 4.2: Representation of the TEPC invented by Rossi.

4.2.1.1 The site size equivalence

The main purpose of microdosimetric detectors is to simulate the interaction of a radiation field with biological matter and in order to achieve this, detectors should have the appropriate features to simulate the dimension and the chemical composition of a cell. The filling gas must have the same type of atoms as the tissue and the same number of atoms with which the ionizing particles interact as it would in biological tissue, so that the difference of density can be ignored.

Density (ρ) and mass stopping power (dE/ρdx) are two proprieties that characterize the detector gas cavity (subscript det) and the tissue site (subscript t); the mean chord length ($\bar{l}_{det}$ and $\bar{l}_t$) defines the size of their volumes.
When the charged particles cross the volume along its mean chord length, they impart a mean energy given by:

$$\bar{\epsilon}_{t,s} = \left[\frac{dE}{\rho dx}\right]_t \rho_t \bar{l}_t \tag{4.7}$$

$$\bar{\epsilon}_{det,s} = \left[\frac{dE}{\rho dx}\right]_{det} \rho_{det} \bar{l}_{det} \tag{4.8}$$

If the tissue and the detector gas are composed of the same atoms and with the same

proportion, their mass stopping power are the same, and if the detector gas density is adjusted so that

$$\rho_{det}\bar{l}_{det} = \rho_t\bar{l}_t \tag{4.9}$$

then the same mean energy will be deposited by the charged particles while they cross the mean chord lengths in both the gas volume and the tissue site:

$$\bar{\epsilon}_{t,s} = \left(\frac{dE}{\rho dx}\right)_t \rho_t\bar{l}_t = \left[\frac{dE}{\rho dx}\right]_{det} \rho_{det}\bar{l}_{det} = \bar{\epsilon}_{det,s} \tag{4.10}$$

The mean specific energy of a single event $\bar{z}_s$ and the mean lineal energy $\bar{y}$, can be easily obtained dividing $\bar{\epsilon}$ by m, the mass of the volume with the density ρ, and $\bar{l}$.

From Equation 4.9 follows Equation 4.11 if r_{det} and r_t are, respectively, the radius of the spherical microdosimeter and the radius of a tissue sphere:

$$\rho_{det} = \rho_t\frac{r_t}{r_{det}} \tag{4.11}$$

This relation can be written also for the cross-sectional ares A_i, the volumes V_i and the masses m_i:

$$A_{det} = A_t\frac{r_{det}^2}{r_t^2} \tag{4.12}$$

$$V_{det} = V_t\frac{r_{det}^3}{r_t^3} \tag{4.13}$$

$$m_{det} = \rho_{det}V_{dett} = \rho_t\frac{r_t}{r_{det}}V_t\frac{r_{det}^3}{r_t^3} = \rho_tV_t\frac{r_{det}^2}{r_t^2} = m_t\frac{r_{det}^2}{r_t^2} \tag{4.14}$$

If $\rho_{det,0}$ is the gas density at normal pressure P_0 and 20°C, and $\rho_{det,x}$ is the gas density at pressure P_x and 20°C then

$$\frac{P_x}{P_0} = \frac{\rho_{det,x}}{\rho_{det,0}} \tag{4.15}$$

Combining Equations 4.9 and 4.15, it follows

$$\rho_{det,x}\bar{l}_{det} = \frac{P_x}{P_0}\rho_{det,0}\bar{l}_{det} = \rho_t\bar{l}_t \tag{4.16}$$

or

$$\frac{P_x}{P_0} = \frac{\rho_t\bar{l}_t}{\rho_{det,0}\bar{l}_{det}} \tag{4.17}$$

For example, if a tissue site with 1 μm diameter must be simulated using a detector with 10 mm diameter, the pressure of the methane-based TE gas filling the microdosimeter must be 9.524 kPa or, if the filling gas is propane-based, then the pressure of the gas must be 5.562 kPa.

This argument remains effective in a multi-event because a single particle i deposits the energy $\overline{\epsilon}_{t,i}$ along the mean chord for which the simulation assumption is valid, $\epsilon_{det,i}$=$\epsilon_{t,i}$, even if, for a given fluence, the particles passing across the microdosimeter volume are more than the particles crossing the corresponding tissue volume of unit density. For this reason, in a multi-events condition, the mean energy $\overline{\epsilon}_{det}$ must be reduced by a factor proportional to the ratio of the two volumes cross-sectional areas:

$$\overline{\epsilon}_t = \overline{\epsilon}_{det} \frac{A_t}{A_{det}} \tag{4.18}$$

that for a sphere becomes

$$\overline{\epsilon}_t = \overline{\epsilon}_{det} \frac{r_t^2}{r_{det}^2} \tag{4.19}$$

Dividing $\overline{\epsilon}_t$ by m_t and $\overline{\epsilon}_{det}$ by m_{det}, from Equations 4.14 and 4.19 follows that

$$\overline{z}_{det} = \frac{\overline{\epsilon}_{det}}{m_{det}} = \frac{\overline{\epsilon}_t \frac{r_{det}^2}{r_t^2}}{m_t \frac{r_{det}^2}{r_t^2}} = \frac{\overline{\epsilon}_t}{m_t} = \overline{z}_t \tag{4.20}$$

It can be concluded then that the $\overline{z}$ imparted in a multi-events condition in a detector is equal to the $\overline{z}$ in a tissue site of density 1000 kg m^{-3} if the particle fluence is the same.

4.2.1.2 Particle tracks

The events, which occur inside the cavity when a radiation interacts with the gas, can be classified in five groups depending on their tracks [43]:

- *stopper* when the particle stops inside the cavity but it is generated outside;
- *starter* when the particle is generated inside the cavity but it stops outside;
- *crosser* when the particle is generated and it stops outside the volume but it crossed the entire cavity depositing part of its energy in the gas;
- *insider* when the particle is the product of an interaction inside the volume and it loses all its energy inside it;
- *toucher* when the track of the particle is tangent of the volume but does not cross it and it can enter in the cavity because of the straggling together with the secondary electrons it might create.

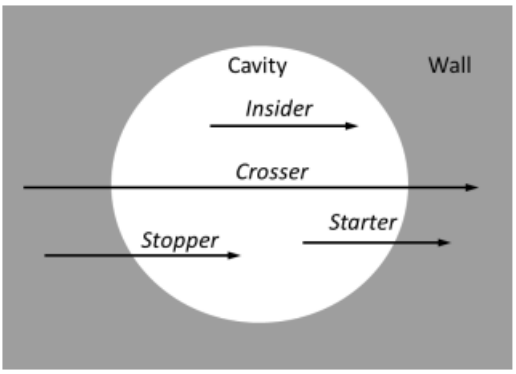

Figure 4.3: Classification of the tracks [44].

4.2.1.3 Tissue-equivalent materials

Another important aspect to take into account, when a detector is built, is the material used both for the filling gas and the walls. The most used material for the walls in the plastic called A-150 developed by Dr Shonka at the Benedictine College in Kansas. Table 4.1 reports the elements which compose the A-150 and it is compared with the composition of tissue of muscle defined by ICRU [45]. The Table neglects the elements with a percentage by weight lower than 1%.

	H	**C**	**N**	**O**	**F**	**Ca**
ICRU (1989) tissue	10.1	11.1	2.6	76.2		
A-150	10.2	76.8	3.6	5.9	1.7	1.8

Table 4.1: Elemental composition in percent by weight of plastic A-150 and muscle tissue [46].

The density of A-150 is 1120 kg m^{-3}. A large percentage of oxygen in the tissue has been replaced by carbon in the plastic A-150 in order to provide a conductivity adequate for ion chambers and proportional counters; this exchange is justified because the neutron kerma factors and the photon mass absorption coefficients are similar for carbon and oxygen at the energies encountered and, therefore, the exchange of oxygen with carbon does not affect the tissue equivalence. Nylon is a significant component of A-150, the concern is that nylon is hygroscopic and the weight of the A-150 could increase by up to 10% due to the water vapour absorption. For this reason, before filling the detector with the gas, the microdosimeter has to be outgassed.

Regarding the filling gas, the most used are three: methane-based TE gas, propane-based TE gas and pure propane. Their composition is reported in Table 4.2.

As it can be seen in Table 4.2, pure propane is not tissue-equivalent because there is no oxygen and nitrogen,for this reason in a study developed in 2015 [47], the equivalence of pure propane and propane-based TE gases for microdosimetric measurement has been studied with a Tissue Equivalent Proportional Counter. Two sites made of different

Gas	Components in percent by partial preassure				ρ (kg m^{-3})	Preassure at 1 μm in a detector with 10 mm diameter (kPa)
	CH_4	C_3H_8	CO_2	N_2		
Methane-based	64.4	0	32.5	3.1	1.05	9.524
Propane-based	0	55	39.6	5.4	1.798	5.562
Propane	0	100	0	0	1.85	5.396

Table 4.2: Composition of the TE gases and their density at 20°C and 100 kPa.

materials are declared similar in terms of radiation dosimetry if their respective mean imparted energies or absorbed doses are the same. Extending this idea to the SV of a TEPC filled with C_3H_8-TE gas mixture or pure C_3H_8, demands that the mean energy imparted by a charged particle, as it enters the detector volume on one of its diameters D, is independent of the gas. The equivalence between the two gases, if the secondary electrons are completely absorbed in the volume, can be described by the following expression:

$$\left(\frac{S}{\rho}\right)^{C_3H_8}(D\rho)^{C_3H_8} = \left(\frac{S}{\rho}\right)^{C_3H_8-TE}(D\rho)^{C_3H_8-TE} \tag{4.21}$$

Where $(\frac{S}{\rho})^{C_3H_8}$ and $(\frac{S}{\rho})^{C_3H_8-TE}$ are the mass collision stopping powers of the primary particle in the propane-based TE and pure propane gases, $(\mathrm{D}\rho)^{C_3H_8}$ and $(\mathrm{D}\rho)^{C_3H_8-TE}$ are the thicknesses in mass per area of the volume in the two gases (ρ is the gas density). Only particles whose ranges are noticeably larger than the target size are valid for Equation 4.21. Because of the different composition of the filling gases $(\mathrm{S}/\rho)^{C_3H_8}/(\mathrm{S}/\rho)^{C_3H_8-TE} \neq 1$, so that $(\mathrm{D}\rho)^{C_3H_8}/(\mathrm{D}\rho)^{C_3H_8-TE}$ varies in the same way. Using the proper calibration factor, a TEPC converts the distribution of ionization produced by incident radiation into a distribution of energy imparted. Therefore, the material equivalence of the filling gases in a TEPC should be based more on the equality of ionisation distributions than on the equality of the imparted energy distributions. Assuming the primary particles pass through the volume on one of the diameters D of the detector, if D is much shorter than the range of the primary particle hence the mean number of primary ionizations is $(\mathrm{D}\rho)/(\lambda\rho)_{ion}$ where $(\lambda\rho)_{ion}$ is the mass per area of the mean free path length with respect to primary ionisation, which depends on the energy and the type of the particle. Using the same radiation field, the response function of the TEPCs filled with C_3H_8-TE gas mixture and C_3H_8 are the same if the measured ionisation spectra are identical; therefore the number of primary ionizations should be the same in the two gases:

$$\frac{(D\rho)^{C_3H_8}}{(\lambda\rho)_{ion}^{C_3H_8}} = \frac{(D\rho)^{C_3H_8-TE}}{(\lambda\rho)_{ion}^{C_3H_8-TE}} \tag{4.22}$$

where $(\lambda\rho)_{ion}$ is the mass per area of the mean free ionisation path length. The discussion of Equation 4.21 is also valid for Equation 4.22.

The study discovered that $(\lambda\rho)^{C_3H_8}{}_{ion}$ for electrons and protons is smaller than $(\lambda\rho)^{C_3H_8-TE}{}_{ion}$ (as it can be seen in Figure 4.4), which means that the number of primary

ionizations produced in the TEPC with pure propane is greater than the one created in the microdosimeter filled with propane-based TE gas.

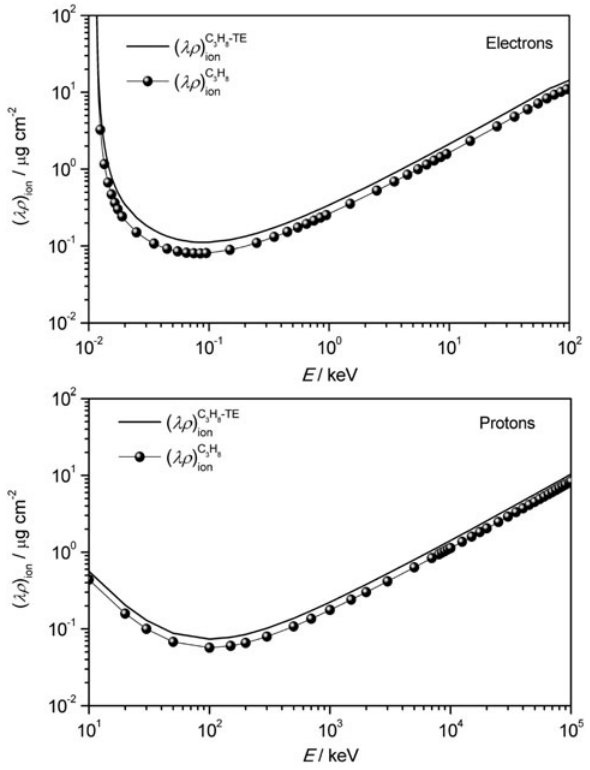

Figure 4.4: Primary ionisation mean free path of electrons (top) and protons (bottom) in C_3H_8 and C_3H_8-TE gases.

The conversion factor $(\lambda\rho)^{C_3H_8}{}_{ion}/(\lambda\rho)^{C_3H_8-TE}{}_{ion}$ is plotted in function of energy E for electrons and protons in Figure 4.5; this factor is used to determine the size of the site $(D\rho)^{C_3H_8}$ of a detector filled with pure propane which has the same response function as the detector filled with propane-based TE gas, as it indicates Equation 4.22. The conversion factor as a function of E is smaller and less dependent on energy than the ratio of (S/ρ) (see Figure 4.5).
So a similar response of the two gases is expected if the propane has a lower density with respect to the propane-based TE gas.

The conclusion of the study is that, in order that the TEPCs with the two different gases considered have the same response, it is sufficient to reduce the mass per area in pure C_3H_8 by a factor of 0.75 when compared with C_3H_8-TE. The microdosimetric spectra were shown to be almost identical and the dose-mean lineal energies does not differ very much, within the reported uncertainty of 1.5%.

4.2.1.4 The detector design and the gas gain

The typical shape of a TEPC is spherical or cylindrical and their principal components are two electrodes: a central wire which represents the anode and the wall which represents

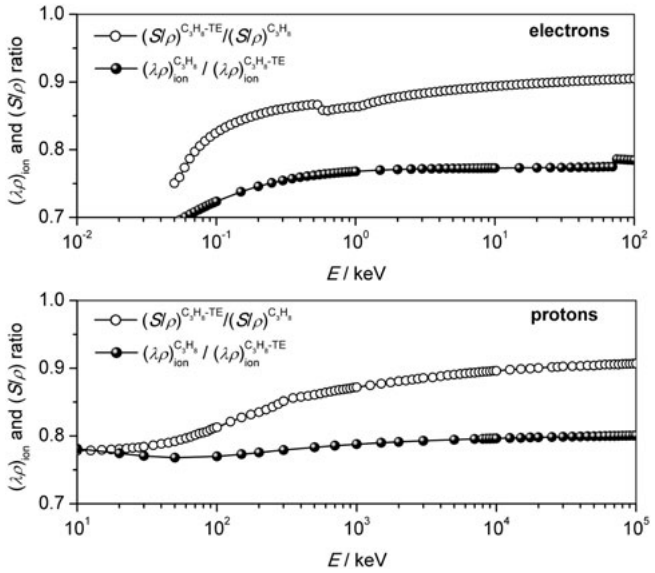

Figure 4.5: Ratio $(\lambda\rho)^{C_3H_8}{}_{ion}/(\lambda\rho)^{C_3H_8-TE}{}_{ion}$ and $(s/\rho)^{C_3H_8-TE}/(s/\rho)^{C_3H_8}$ for electrons (top) and protons (bottom).

the cathode and determines the shape of the cavity.

The choice to build a spherical TEPC is explained by the isotropic response of the device to the radiation field, guaranteeing that the spectrum is independent from the orientation of the microdosimeter; but, if the voltage is applied uniformly to the anode and the cathode, the response of the detector depends on the point where the particle interacts because the electric field is not homogeneous and for this reason a helix is added around the anode in a spherical TEPCs; this third electrode is also added to confine the avalanche. Such a device is complicated to build so that many TEPCs are characterized by a cylindrical geometry and equipped with two or three electrodes (the central wire, the helix and the wall). The electrodes have the function to produce a field characterized by the desired lines of electric field.

Inside the sensitive volume it is possible to identify two different regions (Figure 4.6) depending on the local intensity of the electric field: if the intensity of the field is such that between two interactions with the molecules of the gas the electrons produced do not gain enough energy to create secondary ionization then they are in the *drift region*, otherwise they are in the *multiplication region*.

The gain of the detector is a constant coefficient that determines the proportionality between the initial and the final number of electrons. The separation between the two regions is created by the application of a potential difference to the electrodes and an electric field is produced, which is more intense near the anode.

The gas multiplication process is described in several articles available in the literature; in the following part the classical description, firstly proposed by Townsend and then applied to low-pressure proportional counters by Campion, will be reported.

The gas gain is a parameter that depends on multiple factors such as the type of filling

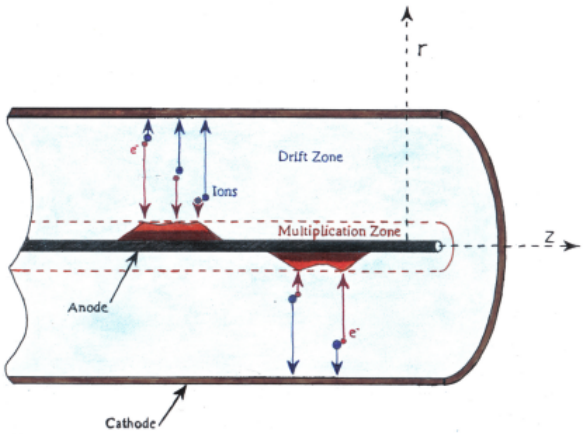

Figure 4.6: Schematic description of the multiplication and drift regions in a cylindrical proportional counter [48].

gas, its pressure, the geometry of the microdosimeter, the potential difference applied to the electrodes and their diameters. The gas gain is defined as the ratio of the total number of secondary electrons to the number of the primary electrons:

$$G = \frac{N_{sec}}{N_{prim}} \tag{4.23}$$

G is linked with the Townsend first-ionisation coefficient α which counts the number of ion pairs produced by one particle when it travels a unit path length:

$$n(d) = n_0 e^{\alpha d} \tag{4.24}$$

where n_0 is the number of initial electrons and d is the distance that an electron travels. Then G can be expressed ad

$$G = \frac{n}{n_0} = e^{\alpha d} \tag{4.25}$$

α depends on the pressure P of the gas and the electric field intensity E according to

$$\frac{\alpha}{P} = Ae^{-BP/E} \tag{4.26}$$

where A is a constant proportional to the reciprocal of the mean free path in a gas at a given pressure and B is connected to the ionisation potential of the molecules which constitute the gas, both are gas specific. Taking the logarithm of both sides of the Equation 4.26, it is expected that the reduced Townsend coefficient α/P becomes constant when E/P gets large and α/P=A.

The electric field in a cyindrical or spherical counter is not constant so that Equation 4.25 becomes:

$$G = e^{\int_a^c \alpha(x)dx} \tag{4.27}$$

where c and a are respectively the point of ionisation and collection which is the anode.
In a counter with a cylindrical geometry the electric field is given by

$$X = \frac{V}{ln\frac{r_c}{r_a}} \tag{4.28}$$

where r_a and r_c are the radii of the anode and cathode respectively and V is the applied potential. When an electron moves between the two locations, the gain is

$$ln(G) = \int_{r_a}^{r_c} \alpha_t dr = \frac{AV}{Bln\frac{r_c}{r_a}} \left[e^{-\alpha P \frac{Bln\frac{r_c}{r_a}}{V}} - e^{-r_c P \frac{Bln\frac{r_c}{r_a}}{V}} \right] \tag{4.29}$$

A r_c»r_a, the previous equation can be approximated by

$$ln(G) \approx \frac{AV}{Bln\frac{r_c}{r_a}} \left[e^{-\alpha P \frac{Bln\frac{r_c}{r_a}}{V}} \right] \tag{4.30}$$

and if an expansion as a series is made

$$ln(G) \approx \frac{AV}{Bln\frac{r_c}{r_a}} \left[\frac{r_c}{r_a} \right]^{\frac{-\alpha BP}{V}} \tag{4.31}$$

4.2.1.5 Wall Effects

The energy deposition in the cavity is influenced by the density differential that a charged particle encounters when it travels through condensed matter that contains a gas cavity. The ICRU (1983) has described four different types of influence, which are called *wall effects*, and they are schematically depicted in Figure 4.7. In the Figure, the homogeneous situation without density difference and the same composition is compared to the situation with the cavity. In the gas volume two concurrent paths allow the particle to deposit energy, while in the case of uniform density two pathways would lead to the deposition of energy in two separate sites. This is why, because of the wall effect, when a gas cavity is inserted into solid matter, the number of events decreases and the mean lineal energy increases compared to the case of uniform density. The wall effect is influenced by the energy and the type of the particles and the size of the simulated volume. The four types of wall effect are the following:

- *delta-ray effect* (a) when a charged particle produces a delta-ray before entering the volume but the delta electron is released near the cavity so that both the particles enter the gas volume. Only the energy deposited by one of the two particle in the observed volume would be considered if the case of no density difference is analyzed. This effect is expected with high-energy electrons or high-energy heavy charged particles;

- *re-entry effect* (b) happens when an electron is scattered back inside the cavity after crossing it, which is less probable with no density difference. Such as in the

delta-ray effect, the re-entry leads to a larger event in the walled volume compared to the wall-less cavity;

- *V-effect* (c) when the two nuclear fragments produced in a non elastic nuclear reaction are created outside the volume but both the particles may enter in the volume and deposit energy inside it, which cannot happen if there is no density differences. Also in this situation, in the walled counter a larger event is recorded compared to the homogeneous density volume;
- *scattering effect* (d) only possible when photons and neutrons are involved; the uncharged particles may create more than one charged particle after interacting through several scattering with the atoms of the matter. If the counter is walled, then the charged particles can be recorded at the same time that is less likely to happen if the counter is wall-less. The result of this effect is the same as the previous.

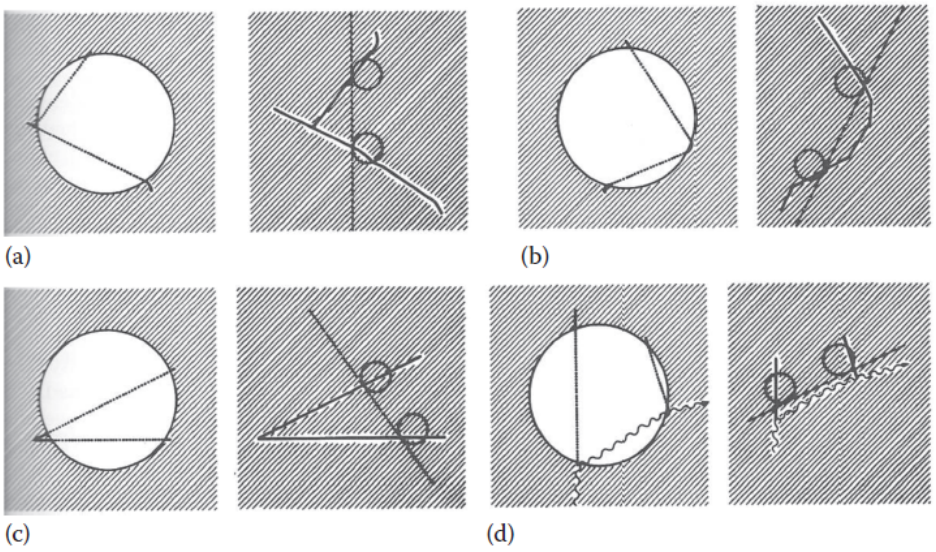

Figure 4.7: Different type of wall effect; the figure shows the energy depositions in a walled counter in comparison with a wall-less counter. (a) Delta-ray effect, (b) re-entry effect, (c) V-effect and (d) scattering effect.

4.2.2 WILLIB: the TEPC developed at LNL

In the framework of ENTER-BNCT project, a cylindrical TEPC with cathode walls, doped with ^{10}B atoms at a concentration of 100 ppm, was used to performed a microdosimetric characterization of the accelerator-based BNC radiation field. The team driven by Valeria Conte at the Laboratori Nazionali di Legnaro of INFN developed and built the TEPC used in this work.

The sensitive volume is a cylindrical volume with a diameter and height of 13 mm. A 100-μm gold-plated tungsten wire is the anode and it is surrounded by a helix of 6

mm in diameter; the cathode is the wall made of plastic A-150 doped with ^{10}B atoms, its thickness is 1 mm and it is composed of two half-cylindrical shell because, originally, the cathode was constructed to be removable and replaced with walls characterized by different concentration of ^{10}B.

The counter in encapsulated in two different caps: a 0.2-mm-think aluminum cap and a 0.4-mm-thick Rexolite cap, for a total counter thickness of 0.21 g cm^{-2} in mass per area (Figure 4.8 and Figure 4.9).

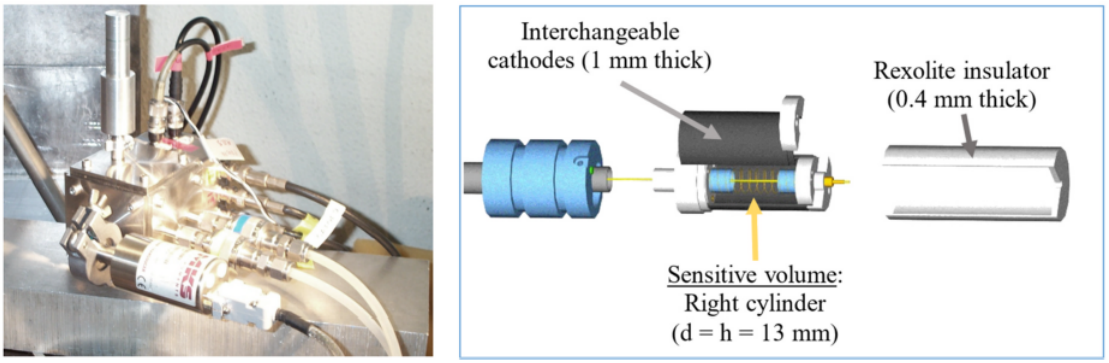

Figure 4.8: Picture of the microdosimeter (left) and a schematic representation of it (right).

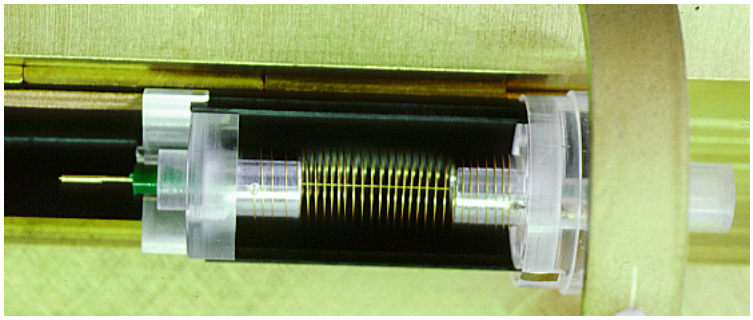

Figure 4.9: Picture of the microdosimeter opened.

The three electrodes (cathode, helix and anode) can be independently biased in order to optimize the gas gain and the energy resolution; the voltages set up for the measurements analyzed in this work in the following chapter are reported in Table 4.3. Two different set-ups of the voltage have been used (see Table 4.3, in particular the high voltage (HV) is necessary to acquire the lower part of the spectra otherwise it would be hidden by the noise. It would be possible to acquire the data using only the high voltage set-up and changing the gain of the amplifiers so that the spectrum would be contained within the input range of the ADC, but the resolution would decrease.

The sensitive volumes of the detector is filled with propane gas at a pressure of 3.14 kPa in order to simulate a site size in tissue with the dimension of 1μm.

	anode	helix	cathode
HV	+350 V	-330 V	-340 V
LV	+350 V	-200 V	-210 V

Table 4.3: Electrodes voltages used during the measurement shift.

4.2.2.1 Gas system

For a correct functioning of the TEPC, a gas system (Figure 4.10) provides a high vacuum level in order to clean the device and this operation has to last for a long time (e.g. two or three days) in order to allow for proper outgassing. Afterwards, the filling gas can be inserted in the detector and continuously flown, using a mass-flow controller and an automatic throttling valve, so that the purity of the gas can be ensured and the reproducibility of the measurements is guaranteed.

Figure 4.10: Picture of the vacuum and gas-flowing system [49].

A schematic drawing of the vacuum and gas-flowing system is reported in Figure 4.11; all the valves, except from the gas valve, remain open during the pumping stage. The gas valve is opened only to insert gas into the detector. A Mass Flow Controller (MFC) controls the gas flow inside the detector and the pressure desired is maintained utilizing an electric valve which a manometer placed downstream of the detector regulates. On a specific electronic module, the steady pressure value and the value of the gas flux can be set.

For the measurements the sensitive volume was filled with the propane gas at a pressure of 3.14 kPa so that the tissue equivalent diameter is 1 μm; the gas inside the SV was continuously flown at a rate of 0,1 cc/min STP.

4.2.2.2 Electronic chain

An outline of the electric chain is reported in Figure 4.12. The microdosimeter is connected to a charge sensitive preamplifier, which creates a pulse proportional to the collected charge Q produced by an event. The shape of the preamplifier output signal is a

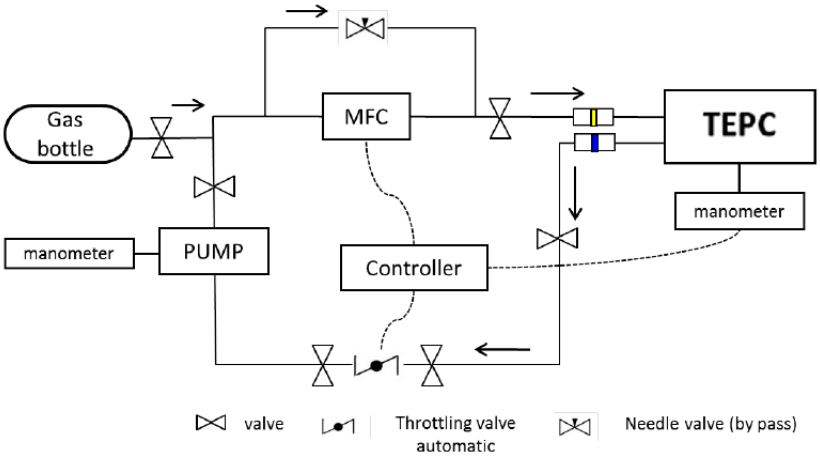

Figure 4.11: Schematic drawing of the vacuum and gas-flowing system.

double exponential with a fast rise time (less than 10 ns) and a decay time of about 50 μs, given by the product of the feedback resistor R_f and capacitance C_f, which determine the time constant of the circuit. The electric avalanche produces a negative signal which is converted into a positive output signal by the preamplifier. The output pulse height is given by V_{out}=-Q/C_f. The signal outgoing from the preamplifier is driven to two spectroscopy amplifiers set at different gains. Their role is to perform gaussian filtering and further amplification on the signals before sending them to the multi-channel analyzer. Two 14-bit analog-to-digital converters (ADCs) receive each event and digitise them in 2^{14}=16384 channels, recording the number of counts for each signal amplitude. The two recorded spectra have a superposition region in order to join them offline to create a single microdosimetric spectrum. The final step consists in sending the ADCs output via a USB-bus to a PC so that the spectra can be saved and analyzed.

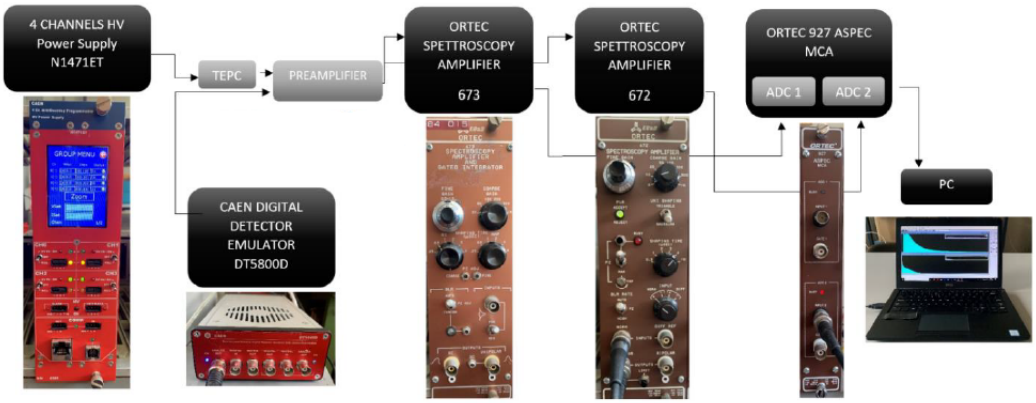

Figure 4.12: The outline of the electric chain employed [50].

4.3 Experimental results and discussion

In the measurements shift carried out from 11 July 2022 to 21 July 2022 we made many measurements in different configurations of the BSA and the microdosimeter. During the campaign, the CN accelerator has been maintained in operation for 24 hours for most of the days in order to attain a good statistics for each configuration that we wanted to test. In all the measurements the microdosimeter has been positioned at a distance of 13 cm from the beam port as it can be seen in Figure 4.14 and it was supported by a lift so that the sensitive volume of the microdosimeter was centered with the collimated neutron beam.
Figure 4.13 reports the simulated spectrum of the beam seen by the microdosimeter; the simulation has been run in the same way as the simulations reported in the previous Chapter, with all the *Alliflu* packages inserted in the BSA.

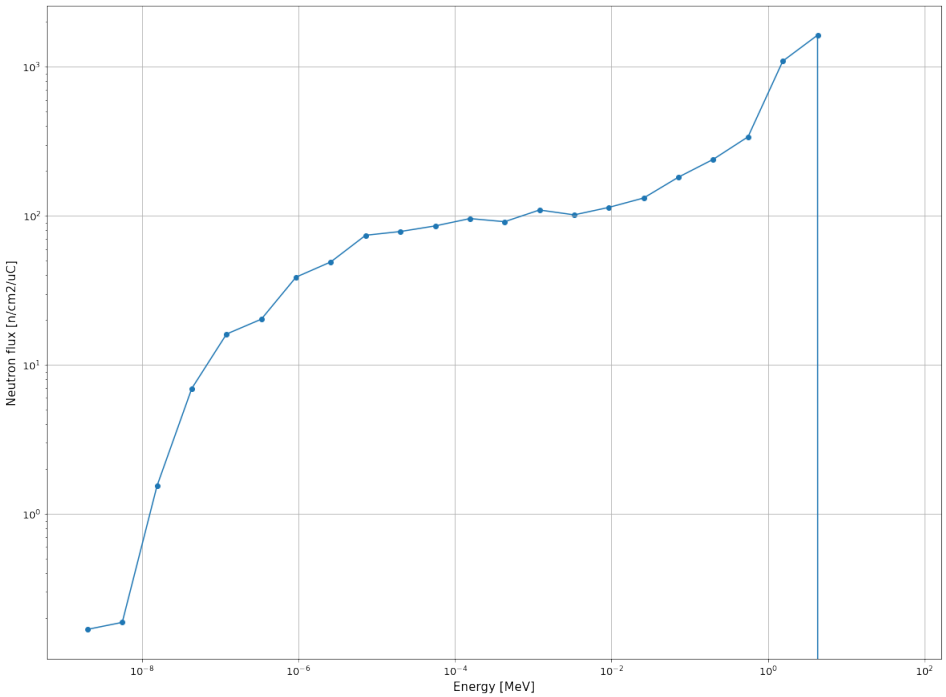

Figure 4.13: Spectrum obtained through simulation of the tally near the beam port of the second configuration of BSA, completely filled by the moderator.

Moreover, the measurements with the different configurations have been made considering the fact that once an *Alliflu* brick was inserted in the BSA, it was not possible to extract, because of radioprotection considerations and practical reasons (we should have moved the entire BSA). Thus, in this Section, the results are not reported in the same order as the measurements have been performed.

The spectra shown below have been obtained with increasing *Alliflu* thickness and with or without cadmium cap.

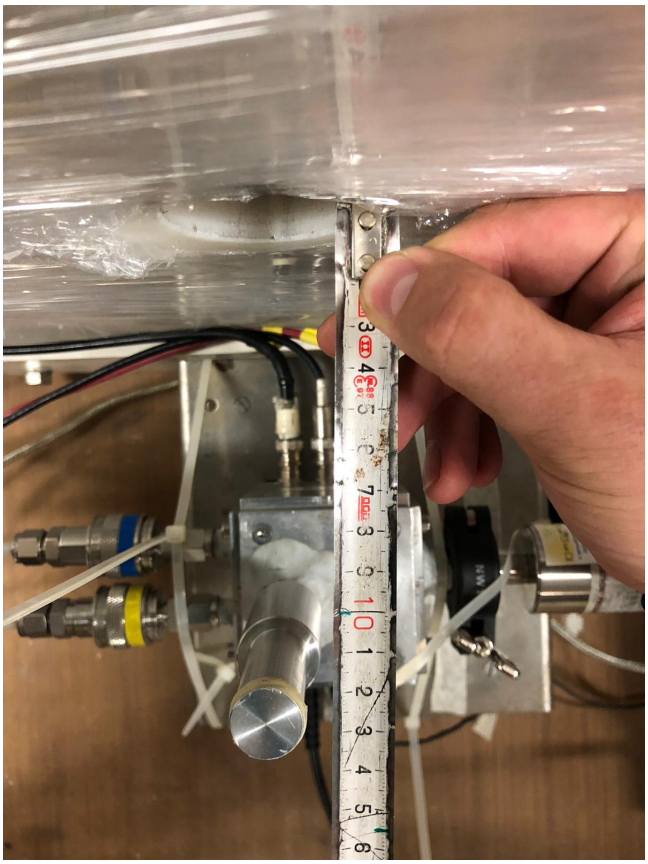

Figure 4.14: Picture from above of the position of the microdosimeter with respect to the beam port.

Figure 4.15: Another prospective of the position of the microdosimeter with respect to the BSA.

4.3.1 Data analysis

The outputs of the two ADCs provide one sub-spectrum for each amplification lines (i.e., one for the low gain and one for the high gain ADC). For each measurement taken, the two spectra are first calibrated in millivolts by means of a research pulser and then binned in logarithmic bins with a bin density of 60 bins/decade. This value has been chosen as the best compromise to maximise the spectral resolution while reducing fluctuations in the data. The procedure for the logarithmic rebinning is described in detail in [50].

The two spectra are then joined offline by superposing the common part, giving a single microdosimetric spectrum. The frequency distribution $f(y)$ is then obtained by normalising on the total number of counts. The dose distribution $d(y)$ is calculated by multiplying $f(y)$ by y and re-normalising.

Since all the measured spectra have an important proton component, the lineal energy calibration has been done by means of the *proton-edge* technique. The proton-edge is a sharp drop in the number of counts in the microdosimetric spectrum, at a specific lineal energy value corresponding to the maximum energy imparted by protons to the gas cavity. The procedure is described in detail in [48], and summarized here: first, the proton-edge region in the $yd(y)$ spectrum is fitted with a Fermi-like function:

$$yd(y) = \frac{A}{1 + e^{B(y-C)}} \tag{4.32}$$

In this Equation, A is the upper limit of the function, C is the position of the inflection point at which $yd(y) = A/2$, and B is a parameter related to the steepness of the function. The inflection point C has been selected as the marker of the proton-edge position. The lineal energy value of $y_{\text{flex}} = 194$ keV/μm has been assigned to the flex position, as discussed in [48].

After the lineal energy calibration, the two spectra obtained by the measurements at high and low voltage (see Table 4.3) are joined to produce the final microdosimetric spectrum for each configuration. Finally, in order to recover at least in part the information on small events hidden by the electronic noise, the final $f(y)$ distribution is extrapolated linearly up to a lineal energy value of 0.01 keV/μm, arbitrarily considered the ionization threshold. This is done by fitting with a linear equation the first 7-10 bins just above the detection threshold [48].

4.3.2 Measurements with increasing thickness of *Alliflu*

Figure 4.16 and Figure 4.17 show the microdosimetric distributions measured with increasing thickness of *Alliflu*. Figure 4.16 shows the frequency distribution of the lineal energy *yf(y)* vs *log(y)*: equal areas under the curve corresponds to equal relative contributions to the total number of events.
In each configuration, it is evident that low LET events (γ and epithermal neutrons) are the most frequent in comparison with the high-LET events (α, Li and recoil ions produced by fast neutrons). Figure 4.16 also shows that increasing the number of *Alliflu* bricks, the component relative to high-LET events decreases while the peak related to low-LET

events increases by a corresponding amount. This is consistent with the moderating properties of the material: the fraction of total flux due to fast neutrons is increasingly reduced in favour of the epithermal component, which is superimposed to the photon events.

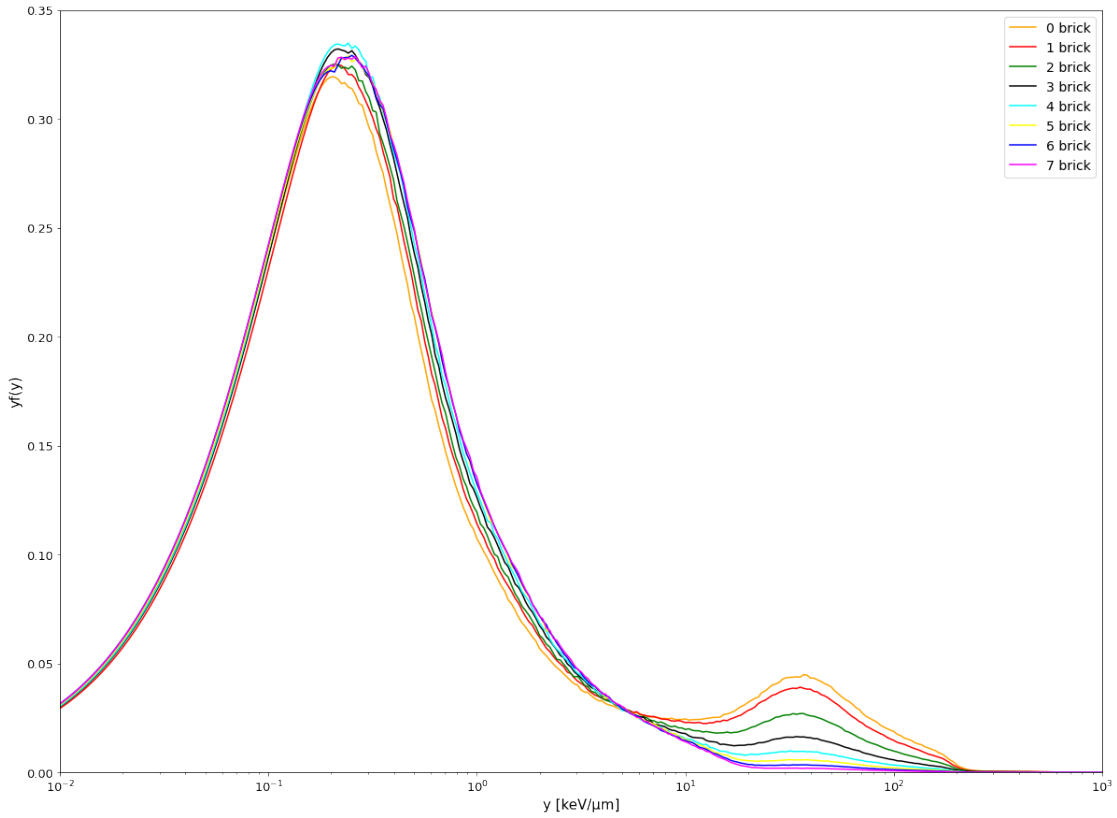

Figure 4.16: Comparison of the microdosimetric spectra (log(y), yf(y)) of the configurations with increasing thickness of *Alliflu*.

The microdosimetric spectra representing the dose distribution (Figure 4.17) is plotted as *yd(y)* vs *log(y)*: the area under the curves between two values of y is proportional to the dose fraction in this interval. In Figure 4.17 a significant contribution to the dose due to high-LET events (above 20 keV/μm) can be seen in the spectra of the measurements with fewer *Alliflu* bricks. This contribution is progressively reduced when the thickness of *Alliflu* increases, and a corresponding increase of the dose contribution due to the low-y part of the spectrum is seen. In other words, without any brick, almost all the dose imparted to the SV is due to protons and ions produced in fast neutron recoils, while when the number of bricks in front of the detector increases, the dose fraction due to photons and epithermal neutrons increases as well, becoming predominant when 7 bricks are present.

Furthermore, in the above spectra the contribution due to thermal neutrons is not observed. It can be understood comparing these spectra with the one obtained within the framework of MUNES (MULtidisciplinary NEutron Source) project which aims at the realisation of an intense accelerator-based source of thermal neutrons. The absence of the

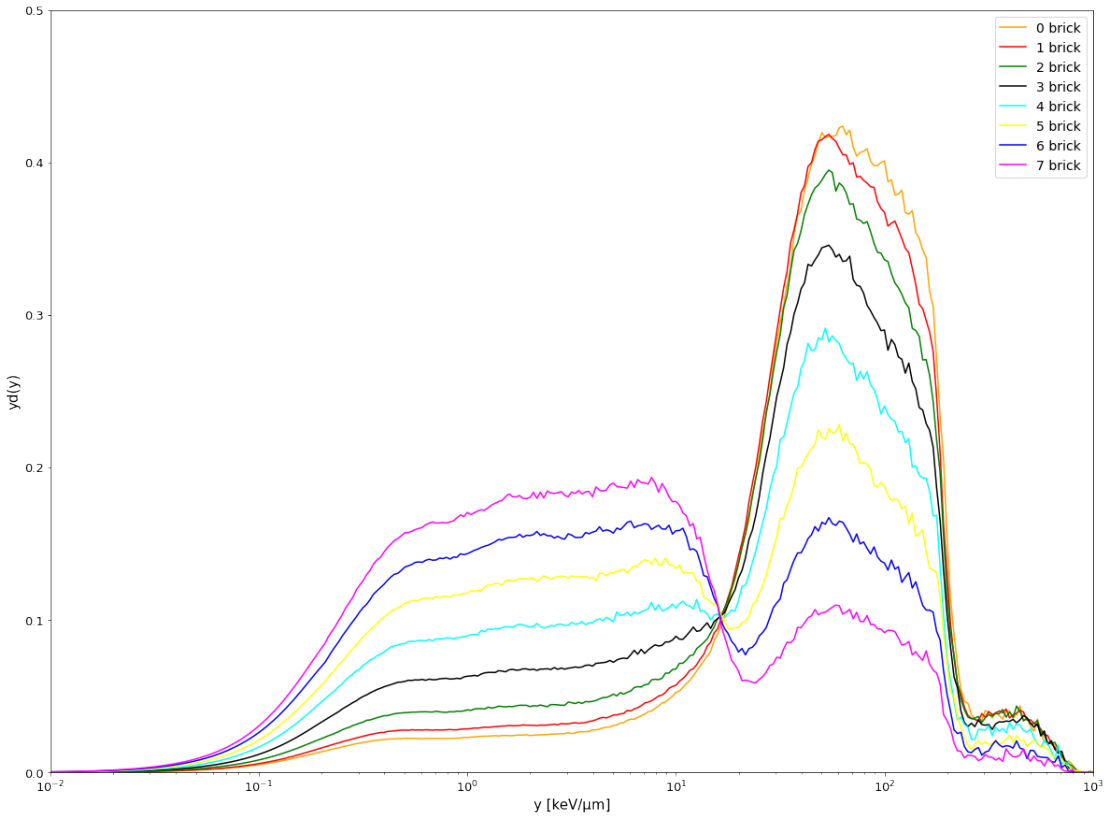

Figure 4.17: Comparison of the microdosimetric spectra (log(y), yd(y)) of the configurations with increasing thickness of *Alliflu*.

thermal neutron contribution is consistent with the very low thermal neutron component which is present in the neutron beam, also with 7 *Alliflu* bricks (see Figure 4.13). An additional phantom would be needed to achieve a thermalization of the neutron beam, which was available at the MUNES facility, characterized by a well thermalized beam. The difference between the spectra can be observed confronting Figure 4.17 and Figure 4.18.

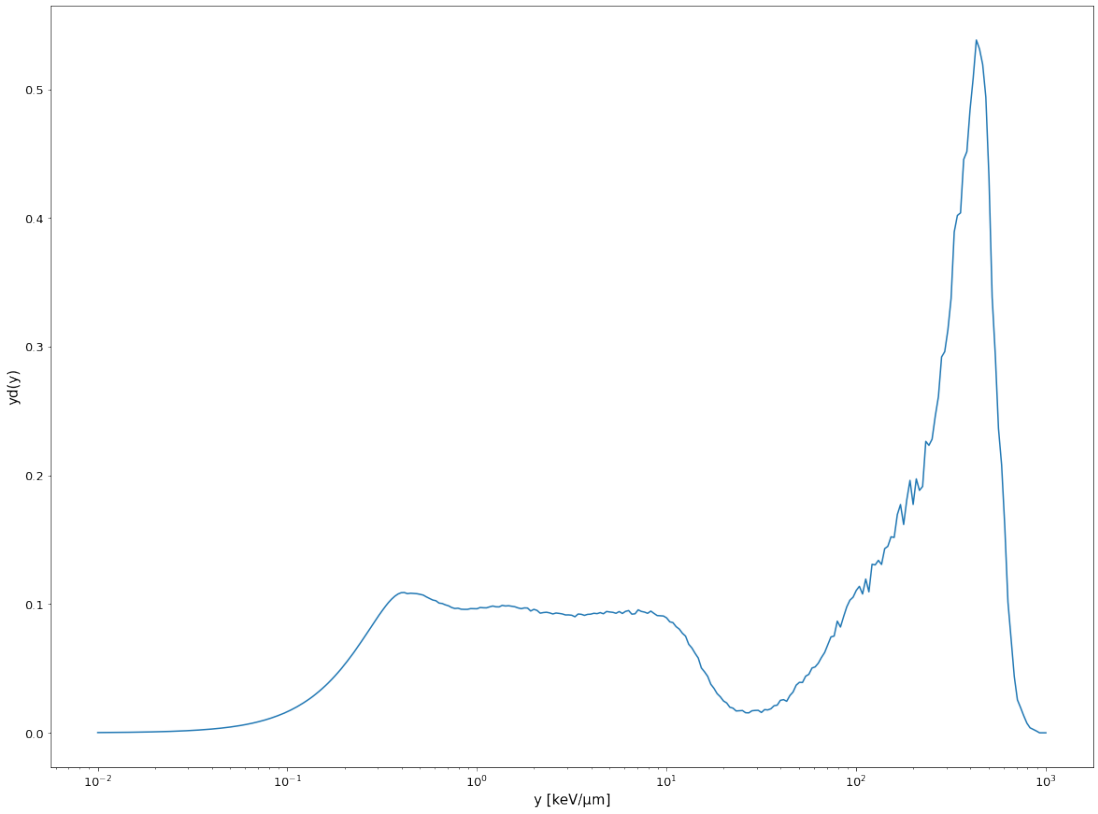

Figure 4.18: Microdosimetric spectrum acquired in the framework of MUNES project [51].

4.3.3 Measurements with and without cadmium

The spectra of the other set of measurements, the one with and without cadmium cap, are reported in Figure 4.19 and Figure 4.20. These measurements have been carried out in two different configurations: 1 and 7 bricks of *Alliflu* in the BSA.
Figure 4.19 shows that the presence of the cadmium cap does not modify the spectrum when only 1 brick is present; on the contrary the measurement with 7 bricks, shown in Figure 4.20, has been more altered by the presence of the cadmium. This is because the cross section of the neutron capture on cadmium presents some resonances in the range of epithermal neutrons.
This can be attributed to the fact that, with 7 *Alliflu* bricks, the fraction of neutron flux in the epithermal range is higher than the case with 1 brick so that the overall spectrum is more affected.

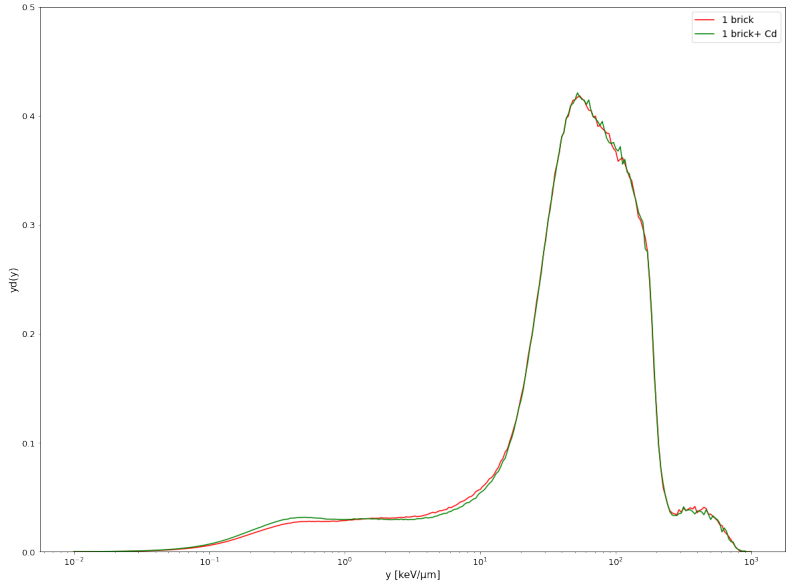

Figure 4.19: Comparison of the microdosimetric spectrum of the two configurations with 1 *Alliflu* bricks: Without (red) and with (green) cadmium cap.

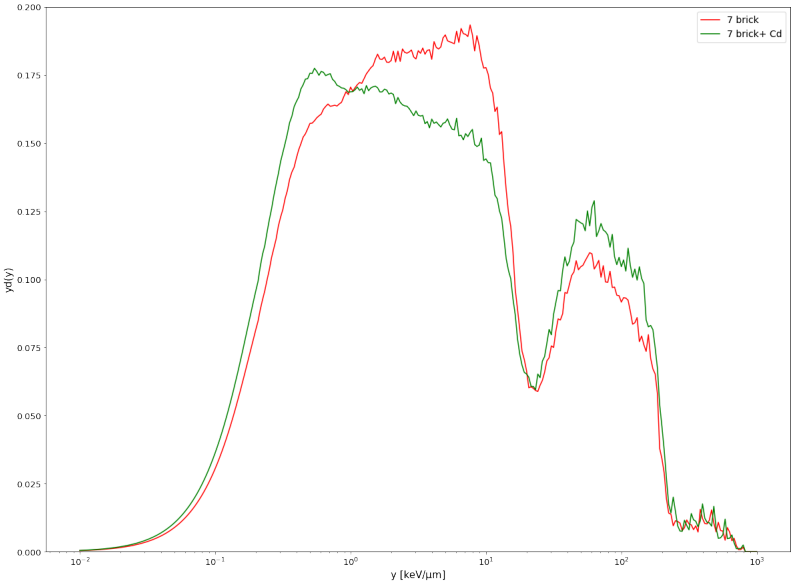

Figure 4.20: Comparison of the microdosimetric spectrum of the two configurations with 7 *Alliflu* bricks: Without (red) and with (green) cadmium cap.

Chapter 5

The next steps

5.1 Microdosimetric simulations

The experiments carried out with the microdosimeter can be simulated by MCNP, although the calculation is not straightforward. In fact, a very detailed transport must be carried out inside the sensitive volume, by simulating each secondary product and following them at very low energies. This is a time-expensive calculation and requires to study features of MCNP physics treatment that usually are not used for macroscopic problems. The preliminary part of this study has been set-up in this thesis work.

First, the geometry of the microdosimeter has been reproduced with MCNP, simulating the same composition and dimensions, as the real one reported in Chapter 4, except from the electronic board housed in the preamplifier box, the helix and the central wire because they are considered not relevant for the tally result, given their small dimensions. Figure 5.1 shows the MCNP geometry of the detector positioned in front of the beam port.

Figure 5.2 shows the detail of the microdosimeter: in pale green the propane gas, in gray the stainless steel walls, in yellow aluminum, in blue the Rexolite and in pink the borated plastic A-150, which is around the cylindrical sensitive volume filled with propane in the upper part of the microdosimeter.

In the microdosimetry simulations the particle transported are neutrons, the secondary particles emitted by neutron interactions, photons and their secondary electrons. The secondaries emitted by neutrons are alpha particles and lithium ions, from interaction with 10-boron in the A-150 and protons from nitrogen capture. Protons are also set in motion by neutron scattering in the gas.

To obtain the microdisimetric spectra it is mandatory to assess the precise dose deposition in the sensitive volume, without any approximation of charged-particle equilibrium. To this end, it is also necessary to lower as much as possible the default minimum energy of the transported particles (electrons, protons, photons, Li ions and α particles).

The last versions of MCNP6 has extended the transport of photons down to 1 eV. In addition, electron transport has been extended down to 10 eV. Moreover, the user can switch off the condensed history calculation for electrons. The new Single Event method,

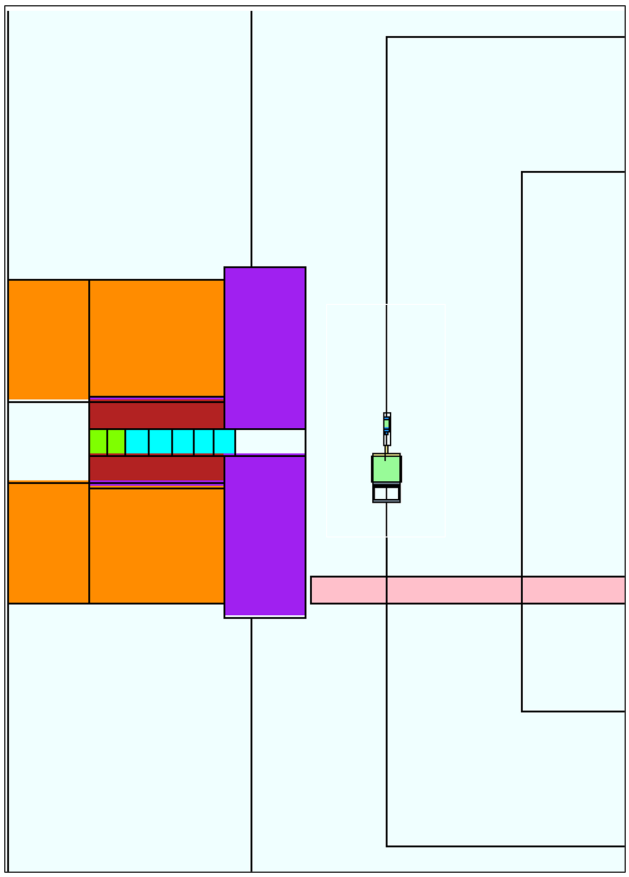

Figure 5.1: Simulation of the microdosimeter in front of the beam-port in the same configuration described in Chapter 4.

coupled with the ENDF/B VI.8 cross sections, transports electrons step by step [34]. The influence in the type of transport of electrons in thin biological samples has been extensively studied by C. Guidi in her MSc thesis [52].

This transport results in a very long calculation time: the transport of electrons is dominated by the long-range Coulomb force, resulting in large numbers of small interactions. For this reason, the described neutron source defined in the target is not efficient. To improve the efficiency, a track-by-track source has been created. This type of source is simulated using the card *SSW* (Surface Source Write) in the input file for MCNP:

```
SSW: surface
```
(5.1)

The surface inserted in the command is at the end of the BSA, at the beam port, as represented in Figure 5.3. In this input file, the importance values related to the geometry component placed beyond the chosen surface, have been set to 0.

The output provides the information (energy, direction of flight and position) related to the particles which cross the surface recorded in a binary file called *rssa*. This is a source that can be used in the following runs, where the user specifies the instruction

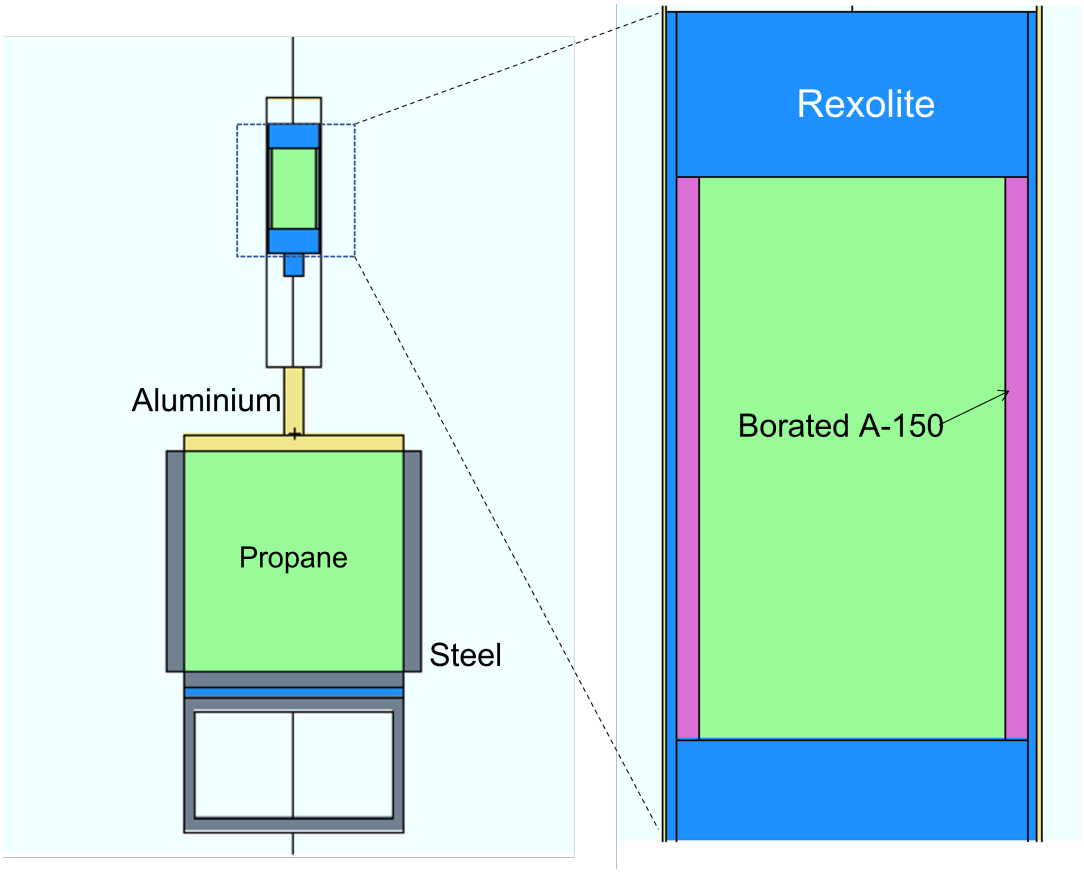

Figure 5.2: Simulation of the microdosimeter: in pale green the propane gas, in gray the stainless steel walls, in yellow aluminum, in blue the rexolite and in pink the borated plastic A-150. This thin layer is visible in the zoom.

SSR (Surface Source Read):

```
SSR: surface
```
(5.2)

This card allows running particles as recorded in the file rssa, avoiding the expensive transport between the target and the tally.

The new source has to be validated, to ensure that there is no bias in replacing the detailed source defined in the target. To accomplish this, we compared the spectrum obtained in the air volume defined at the microdosimeter position (see Figure 5.3) obtained with the detailed source and with the rssa. In Figure 5.4 the comparison of the spectra is shown. The two sources behave in the same way, hence the microdosimetry simulations can be run using the rssa source. To further improve the efficiency of the calculation, the importance of the geometry components irrelevant for the microdosimeter, such as the region beyond the detector towards the wall, can be set to 0.

Although MCNP is not optimized for microdosimetry calculations, some authors have recently investigated its potential in this sense, especially exploiting the new features of

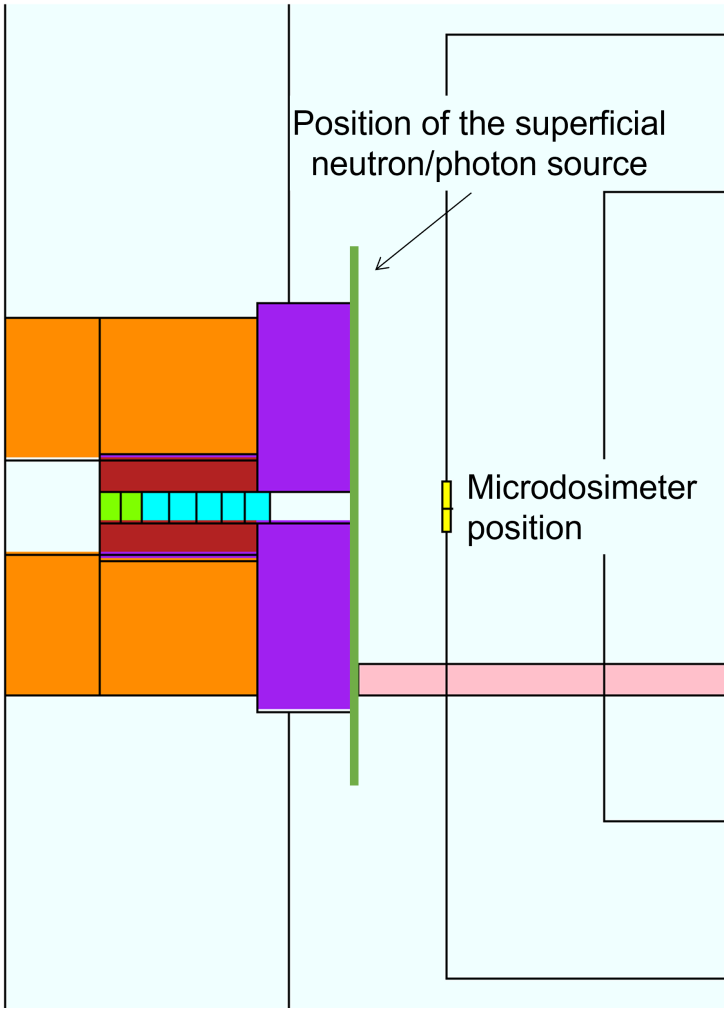

Figure 5.3: Position of the ssw/ssr source calculation and of the volume where the neutron spectrum reaching the microdosimeter is calculated

the last release [53] [54] [55]. These works help in setting the input file for the simulation, for example the physics models to be used and their parameters. This study is presently at the beginning and will be carried out in the following months. It will be interesting to set-up simulations also in PHITS and in GEANT4: the rssa source is easily translated into the syntax of these codes, as well as the geometry in the case of PHITS.

Simulations of the microdosimetry spectra help in understanding the property of the BNCT beam and deepen the insight into the relation between the dose absorbed in the biological tissue and the radiobiological effects observed. Thus, not only they are important for quality assurance, but they also contribute to understand how the dose delivered to patients is related to a clinical outcome.

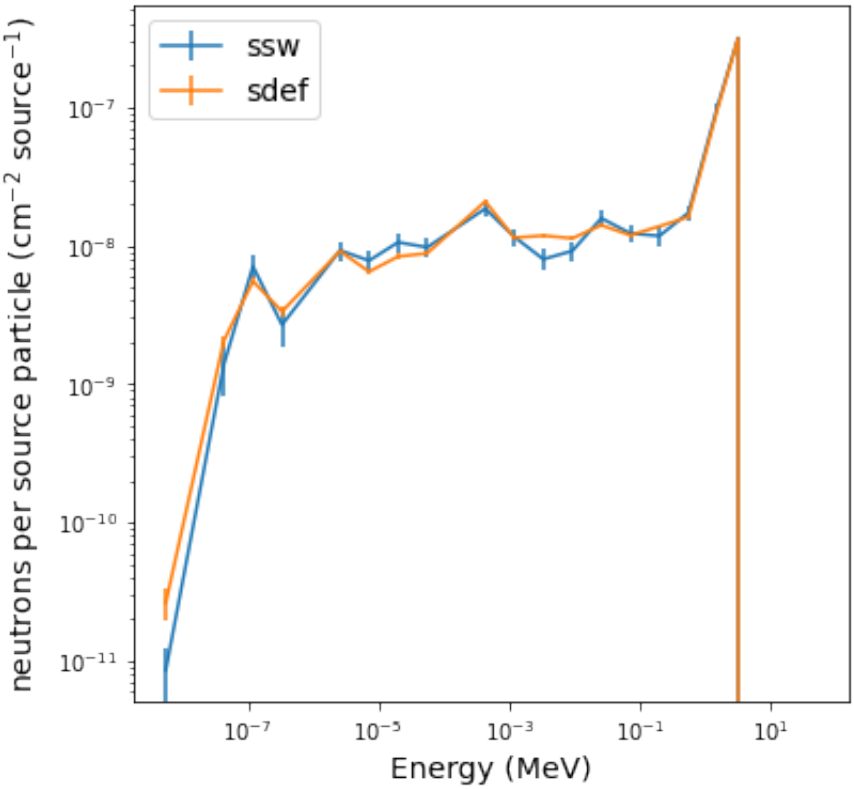

Figure 5.4: Comparison of the spectra obtained with the SSw source (blu) and the original source (orange)

Chapter 6

Conclusion

This thesis has been developed in the field of BNCT, a promising therapy for metastatic or infiltrated tumors or for those that cannot be treated using conventional radiotherapy. BNCT is a binary hadrontherapy which exploits a low energy neutron beam, thermal or epithermal depending on the depth of the tumor, and a borated agent selectively accumulated in the tumor. In particular, this thesis is carried out in the field of the Accelerator-Based Boron Neutron Capture Therapy (AB-BNCT). The production of clinical neutron beams using accelerators has become possible in the last years thanks to the advancements of the technologies needed. Such technologies have been studied, designed, and partially constructed also in Italy.
The work described in this thesis has been developed in the framework of ENTER-BNCT, a project funded by the Commission 5 for Technological and inter-disciplinary research of INFN. ENTER-BNCT is framed in the INFN project for a clinical BNCT facility based on its RFQ accelerator coupled to a beryllium target.

The work of this thesis consists of computational and experimental studies of the spectrum of a neutron beam produced following the interaction of a proton beam, generated in the CN accelerator at the Laboratori Nazionali di Legnaro (LNL) of INFN, and a Beryllium-Vanadium-Copper target. The work described here also includes my experience at LNL, where I spent 10 days to participate in the second measurement campaign, carried out in July 2022, during which I contributed to the target installation, the preparation of measurements and the data acquisition. Measurements were carried out using a prototype of Beam Shaping Assembly (BSA) built at the mechanical workshop of INFN, Unit of Pavia. The BSA is a reduced version of a more complex assembly, designed for the clinical beam [20]. The design of this prototype has been conceived and built to house a new moderator called *Alliflu*, consisting in densified lithiated aluminum fluoride and produced in Pavia through an innovative sintering process [29]. Two versions of the BSA were tested: one consisting of a lead reflector, a borated polyethylene shell and a collimator and another obtained adding a polyethylene extra shell.

The first part of the thesis was dedicated to the study of the macroscopic spectra of the beam leaving the two prototypes of the BSA, both with increasing thickness of *Alliflu*. The simulations have been run using the transport code MCNP6.2.

The simulations of the first prototype of the BSA show that the integral flux decreases as the thickness of the moderator increases, and the fast component decreases without reducing significantly the epithermal flux. The same results have been obtained experimentally, using the spectrometer DIAMON developed at Politecnico di Milano in collaboration with the Italian start-up Raylab. The experimental spectra reported here are obtained with a blind deconvolution which returns non-optimized results. However, the integral flux, which is the quantity for which the detector has been designed, is very well reproduced by the simulations.

Concerning the second prototype of the BSA, which is characterized by an additional part made of polyethylene, the experimental data are still under analysis. For this part the work focused on the simulations. In addition to the spectra calculated in the position of the DIAMON, a tally has been placed in the position of the microdosimeter, the detector used to obtain the microdosimetric spectra described in Chapter 4. The simulated spectra show a further suppression of the fast component. In fact, comparing the spectra of the two prototypes of BSA we deduce that in the second prototype the component related to the fast neutrons, which delivers unwanted dose to the patients, has been further reduced; moreover, increasing its thickness the relative suppression becomes more evident at the expense of a lower epithermal component.

Simulations have been also carried out to evaluate the ambient dose, comparing the two prototypes and what it can be seen is that the additional polyethylene shell reduces the energy deposition so that it is possible to work with a higher proton current. This dose suppression is due to a better shielding of neutrons escaping from the BSA even if the presence of polyethylene produces more 2.2 MeV photons.

The second phase of the work focused on the study of the microdosimetric spectra which have been obtained using a Tissue-Equivalent Proportional Counters (TEPC) developed and built at the Laboratori Nazionali di Legnaro (LNL). It is the first time that a microscopic spectrum is available for a neutron beam produced through a reaction (p,n) on a beryllium target and moderated with aluminum fluoride.

The microdosimetric spectra have been collected increasing the thickness of *Alliflu* in the BSA and with or without a cadmium cap, to absorb the thermal part of the spectrum and allow a rough evaluation of the presence of a significant epithermal component.

Changing the thickness of moderator, the microdosimetric frequency distribution *yf(y)* vs *log(y)*, show that the low-LET events are more frequent than the high LET events. This is mainly due to the presence of a significant gamma background in the experimental room, produced by the neutron beam. However, increasing the thickness, the peak relative to high-LET events decreases while the peak of the low-LET events increases. This is consistent with the expected function of the new moderator. Analyzing the dose distribution *yd(y)* vs *log(y)*, the high-LET events (above 20 keV/μm) contribute more to the total dose than the low-LET events when no bricks are present, but, increasing the number of *Alliflu* bricks, the contribution of the former decreases in favor of the dose delivered by low-LET events. The conclusion is that, without the moderator, the dose is due to protons and ions produced in fast recoils, instead with all the moderator inserted

the dose fraction due to epithermal neutrons and photons becomes predominant. Regarding the measurements with and without cadmium, with with 1 and 7 bricks of *Alliflu*, the cadmium affects more the spectrum with 7 bricks than the one with 1 which means that the cadmium absorbs part of the epithermal neutrons. This is explained by the fact that 7 bricks has higher cross section for capture in cadmium.

Finally this thesis has laid the foundations to carry out a microdosimetric simulation using the transport code MCNP. In order to perform such a simulation, in this thesis a track-by-track source has been produced. This source has been validated comparing the spectrum obtained at the microdosimeter position with the original source defined at the target and the one obtained using the track-by-track source defined at the beam port. Moreover, the simulation of the geometry of the microdosimeter has been reproduced in detail.

For the first time, simulations and experimental measurements for a neutron beam produced through an accelerator and using lithiated alluminum fluoride as the moderator has been obtained. This work produced new knowledge about the modulation of the beam due to a new material, and this will be exploited for the future BNCT clinical beam. Moreover, the work developed in this thesis lays the foundations for a deeper understanding of the relation between the beam characteristics and the observed effects in radiobiological models and in patients. In this respect, the comparison of simulated and experimental microdosimetric spectra, beside providing a further validation of the simulation procedure, can give detailed information on the composition of the radiation field seen by the treated tissue, which could be of great aid to improve Quality Assurance procedures in BNCT.

Bibliography

[1] Jeffrey A Coderre et al. “Boron neutron capture therapy: cellular targeting of high linear energy transfer radiation”. In: *Technology in cancer research & treatment* 2.5 (2003), pp. 355–375.

[2] GL Locher. “Biological Effects and therapeutical possibilities of neutrons”. In: *Am. J. Roentgenol. Radium. Ther.* 36 (1936), pp. 1–13.

[3] Daniel N. Slatkin. “A history of Boron Neutron Capture Ttherapy of brain tumours: postulation of a Brain radiation tolerance limit”. In: *Brain* 114.4 (1991), pp. 1609–1629.

[4] H Hatanaka and KZ Sano. “A revised boron-neutron capture therapy for malignant brain tumours.” In: *Neurol* 204 (1973), pp. 309–332.

[5] Y Mishima et al. “New Thermal Neutron Capture Therapy for Malignant Melanoma: Melanogenesis-Seeking 10B Molecule-Melanoma Cell Interaction From In Vitro to First Clinical Trial”. In: *Pigment Cell Research* 2.4 (1989), pp. 226–234.

[6] Y Mishima et al. “Treatment of Malignant Melanoma by Single Theraml Neutron Capture Therapy with Mealanoma-seeking 10B compound”. In: *The Lancet* 334.8659 (1989), pp. 388–389.

[7] AZ Diaz, DA Chanana, and Coderre JA. “Retrospective review of the clinical BNCT trial at Brookhaven National laboratory”. In: *Proceedings of the Ninth International Simposium on Neutron Capture Therapy for Cancer, Osaka 13-14* (2000).

[8] JA Coderre et al. “Boron neutron capture therapy of glioblastoma multiforme using the p-borophenylalanine-fructose complex and epithermal neutrons: tryal design and early clinical results”. In: *J. Neuro-Oncol.* 33 (1997), pp. 141–151.

[9] “First BNCT treatment of a skin melanoma in Argentina: dosimetric analysis and clinical outcome”. In: *Applied Radiation and Isotopes* 61.5 (2004). Topics in Neutron Capture Therapy: Proceedings of the Eleventh World Congress on Neutron Capture Therapy (ISNCT-11), pp. 1101–1105.

[10] H Madoc-Jones et al. “A phase-I dose escalation trial of boron neutron capture therapy for subjects with subcutaneous melanoma of the extremities”. In: *Y.Mishima ed, Cancer Neutron Capture Therapy* (1996), pp. 707–716.

[11] J Capala et al. “Boron neutron capture therapy for glioblastoma multiforme: clinical studies in Sweden”. In: *J. Neuro-Oncol.* 62(1-2) (2003), pp. 135–144.

[12] M Suzuki et al. "Feasibility of boron neutron capture therapy (BNCT) for malignant pleural mesothelioma from a viewpoint of dose distribution analysis". In: *International Journal of Radiation Oncology, Biology and Physics* 66.5 (2006).

[13] "Extra-corporeal liver BNCT for the treatment of diffuse metastases: What was learned and what is still to be learned". In: *Applied Radiation and Isotopes* 67.7, Supplement (2009), S67–S75.

[14] K Hideghéty et al. "Postoperative treatment of glioblastoma with BNCT at the Petten irradiation facility (EORTC Protocol 11961)". In: *Strahlenther. Onkol.* 175(2) (1999), p. 111.

[15] "Report on the first patient group of the phase I BNCT trial at the LVR-15 reactor". In: *Sauerwein W, Moss R, Wittig A, editors. Research and Development in Neutron Capture Therapy, Bologna, Monduzzi Ed.* (2002), pp. 1107–1112.

[16] Leena Kankaanranta et al. "Boron neutron capture therapy in the treatment of locally recurred head-and-neck cancer: final analysis of a phase I/II trial". In: *International Journal of Radiation Oncology* Biology* Physics* 82.1 (2012), e67–e75.

[17] O Harling and KJ Riley. "Fission reactor neutron sources for neutron capture therapy — a critical review." In: *J Neuro-Oncol* 62 (2003), pp. 7–17.

[18] *Current Status of Neutron Capture Therapy*. TECDOC Series 1223. Vienna: INTERNATIONAL ATOMIC ENERGY AGENCY, 2001. URL: https://www.iaea.org/publications/6168/current-status-of-neutron-capture-therapy.

[19] AA.VV. "Methods and models of dose calculation". In: *IAEA TecDoc on BNCT, under publication* ().

[20] Ian Postuma et al. "A novel approach to design and evaluate BNCT neutron beams combining physical, radiobiological, and dosimetric figures of merit". In: *Biology* 10.3 (2021), p. 174.

[21] H Koivunoro et al. "BNCT dose distribution in liver with epithermal D–D and D–T fusion-based neutron beams". In: *Applied Radiation and Isotopes* 61.5 (2004). Topics in Neutron Capture Therapy: Proceedings of the Eleventh World Congress on Neutron Capture Therapy (ISNCT-11), pp. 853–859.

[22] J. Reijonen. "Compact Neutron Generators for Medical, Home Land Security, and Planetary Exploration". In: *Proceedings of the 2005 Particle Accelerator Conference*. 2005, pp. 49–53. DOI: 10.1109/PAC.2005.1590356.

[23] Jacopo Valsecchi. "Thermal and Epithermal neutron beam tailoring for BNCT research at CN proton accelerator of INFN Legnaro National Laboratories - Msc Thesis - University of Pavia". In: (2014).

[24] Andres Juan Kreiner et al. "Present status of accelerator-based BNCT". In: *Reports of Practical Oncology & Radiotherapy* 21.2 (2016), pp. 95–101.

[25] M. Paul et al. "A high-power liquid-lithium target (LiLiT) for neutron production". In: 305.3 (2015), pp. 783–786.

[26] Andres J Kreiner. "Accelerator-based BNCT". In: *Neutron Capture Therapy* (2012), pp. 41–54.

[27] A Pisent, E Fagotti, and P Colautti. “MUNES a Compact Neutron Source for BNCT and Radioactive Wastes Characterization”. In: *Proceedings of LINAC2014, Geneva, Switzerland* (2014), MOPP088.

[28] J Esposito et al. “Be target development for the accelerator-based SPES-BNCT facility at INFN Legnaro”. In: *Applied Radiation and Isotopes* 67.7-8 (2009), S270–S273.

[29] Chiara Magni. “Experimental and computational studies for an Accelerator-Based Boron Neutron Capture Therapy clinical facility: a multidisciplinary approach - PhD thesis - University of Pavia”. PhD thesis. 2022.

[30] Gabriele Parisi. “AlF3-moderated neutron flux characterization by means of experiments and Monte Carlo simulations for BNCT applications - Msc Thesis - Turin Polytechnic”. In: (2019).

[31] Gabriele Parisi et al. “Development of the ACSpect neutron spectrometer: Technological advance and response against an accelerator-based neutron beam”. In: *Radiation Measurements* 154 (2022), p. 106776.

[32] Andrea Pola et al. “DIAMON: A portable, real-time and direction-aware neutron spectrometer for field characterization and dosimetry”. In: *Nuclear Instruments and Methods in Physics Research Section A: Accelerators, Spectrometers, Detectors and Associated Equipment* 969 (2020), p. 164078.

[33] AA.VV. “Conversion Coefficients for use in Radiological Protection against External Radiation. ICRP Publication 74.” In: *Annals of ICRP* 26.3-4 (1996).

[34] C. J. Werner (editor). “MCNP Users Manual - Code Version 6.2”. In: *Los Alamos National Laboratory, Los Alamos, NM, report LA-UR-17-29981* (2017).

[35] Ian Postuma. “Clinical application of accelerator-based Boron Neutron Capture Therapy: optimisation of procedures, tailoring of a neutron beam and evaluation of its dosimetric performance - PhD thesis - University of Pavia”. PhD thesis. 2015.

[36] Stefano Agosteo et al. “Characterization of the energy distribution of neutrons generated by 5 MeV protons on a thick beryllium target at different emission angles”. In: *Applied Radiation and Isotopes* 69.12 (2011), pp. 1664–1667.

[37] HH Rossi and M Zaider. “Elements of microdosimetry”. In: *Medical Physics* 18(6) (1991), pp. 1085–1092.

[38] Anatoly B. Rosenfeld. “Novel detectors for silicon based microdosimetry, their concepts and applications”. In: *Nuclear Instruments and Methods in Physics Research Section A: Accelerators, Spectrometers, Detectors and Associated Equipment* 809 (2016), pp. 156–170.

[39] Stefano Agosteo and Andrea Pola. “Silicon microdosimetry”. In: *Radiation Protection Dosimetry* 143.2-4 (2010), pp. 409–415.

[40] Consuelo Guardiola et al. “Microdosimetry in low energy proton beam at therapeutic-equivalent fluence rate with silicon 3D-cylindrical microdetectors”. In: *Physics in Medicine & Biology* 66.11 (2021), p. 114001.

[41] Jeremy A Davis et al. “Evolution of diamond based microdosimetry”. In: *Journal of Physics: Conference Series*. Vol. 1154. 1. IOP Publishing. 2019, p. 012007.

[42] C Verona et al. “Microdosimetric measurements of a monoenergetic and modulated Bragg Peaks of 62 MeV therapeutic proton beam with a synthetic single crystal diamond microdosimeter”. In: *Medical Physics* 47.11 (2020), pp. 5791–5801.

[43] Randall S Caswell. “Deposition of energy by neutrons in spherical cavities”. In: *Radiation Research* 27.1 (1966), pp. 92–107.

[44] Sabina Chiriotti Alvarez. “Microdosimetry of hadron therapy beams using mini Tissue-Equivalent Proportional Counters.” PhD thesis. 2015.

[45] AA.VV. “ICRU Report 28: Basic Aspects of High Energy Particle Interactions and Radiation Dosimetry”. In: *Journal of the ICRU* 15.1 (1978).

[46] L Lindborg and A Waker. *Microdosimetry: Eperimental Methods and Applications (1st Ed.)* Physical Sciences. CRC Press, 2017. ISBN: 9781315373737.

[47] S. Chiriotti et al. “Equivalence of pure propane and propane TE gases for microdosimetric measurements”. In: *Radiation Protection Dosimetry* 166.1-4 (2015), pp. 242–246.

[48] Anna Bianchi. “Microdosimetry of therapeutic proton beams.” PhD thesis. 2021.

[49] Elisa Motisi. “Development of microdosimetric techniques applied to hadron therapy.” 2015.

[50] Giulia Giustiniani. “A miniaturized tissue-equivalent proportional counter for characterizing boron capture therapy radiation fields”. In: (2021).

[51] A. Selva et al. “Microdosimetry of an accelerator based thermal neutron field for Boron Neutron Capture Therapy”. In: *Applied Radiation and Isotopes* 182 (2022), p. 110144.

[52] Claretta Guidi. “Irradiation of reconstructed human skin cultivated in-vitro: computational dosimetry and preliminary radiobiological evaluations for BNCT studies - MSc Thesis - University of Pavia”. In: (2020).

[53] Rodolphe Antoni and Laurent Bourgois. “Microdosimetric spectra simulated with MCNP6.1 with INCL4/ABLA model for kerma and mean quality factor assessment, for neutrons between 100keV to 19MeV”. In: *Radiation Measurements* 128 (2019), p. 106189.

[54] Mouhamad Elbast et al. “Microdosimetry of alpha particles for simple and 3D voxelised geometries using MCNPX and Geant4 Monte Carlo codes.” In: *Radiation protection dosimetry* 150 3 (2012), pp. 342–9.

[55] Jan Lillhök, Robert Billnert-Maróti, and Anastasios Anastasiadis. “MCNP 6.2 simulations of energy deposition in low-density volumes corresponding to unit-density volumes on the nanometre level”. In: *Radiation Measurements* 157 (2022), p. 106831.